Mesoscopic simulations of the polymer and microfluidics

by

Lei Jiang

A dissertation submitted in partial fulfillment
of the requirements for the degree of
Doctor of Philosophy
(Physics)
in the University of Michigan
2014

Doctoral Committee:

Professor Ronald G. Larson, Chair
Professor Sharon C. Glotzer
Professor Finn Larsen
Professor Jens-Christian D. Meiners

To my father Yongjun Chen and mother Yuming Jiang

For bringing me to this world,

then everything to me becomes possible.

Acknowledgements

Everything happens for a reason. Such reason is so profound that the objective physical world is already complicated enough for us to fully understand and we still hardly see an end of physics, needless to say involving ourselves in the whole cause. But I believe there is a general causality governing the universe involving each sentient being, and we do not randomly meet people in our lives. Before I can comprehensively understand the whole cause, being grateful is one of the best actions I can take to face the seemingly unpredictable world, keeping me content with my lot and keeping me open to all kinds of possibilities. Gratefulness gives me strength, and motivates me to carry on for pursuing the ultimate truth.

First and foremost, I would like to thank my Ph.D. advisor, Professor Ronald Larson. It has not been smooth for my graduate life. I switched my advisors twice, and by the time I left my second group, I was already on my fifth year. With all the mistakes I had made, I dug myself a deep hole and could hardly find any group to accept me. Thanks to Professor Larson, without his forgiveness to my mistakes and giving me the chance to continue my graduate study in his group, this dissertation could not be possible. This almost three-year period of working with Professor Larson has been the happiest time so far in my life. I want to express my deep and sincere gratitude to Professor Ronald Larson, and it will be a life-long appreciation.

I would like to thank my former advisors, Professor Roberto Merlin, Professor Alfred Hero and my former co-advisor Professor Anthony Grbic. I am feeling sorry for not working out and all the troubles I brought to them. Nevertheless, my deep thankfulness to them for their patient guidance on my research, especially thank Professor Merlin and Professor Hero for keeping

supporting me during my transition, otherwise my graduate life would have been much more difficult.

I would like to thank Professor Cagliyan Kurdak and Professor Finn Larsen for their kind help and valuable suggestions during my switching groups.

I would like to thank my committee members, Professor Sharon Glotzer, Professor Finn Larsen and Professor Jens-Christian Meiners for their patience and support.

I would like to thank Christina Zigulis and Christine Bolang in the student office for all the cordial help I received on numerous occasions, which makes my graduate life much easier.

I would like to thank my former and current group members for giving me a sweet memory of my stay in the groups.

I would like to thank all my friends for their love, support and those happy times we spent together during my graduate life.

Finally, I would like to thank my parents, for everything, everything! Thank you!

And thanks to all who have helped to make this dissertation possible!

Table of Contents

List of Figures

List of Tables

Abstract

This thesis focuses on the dynamics and transport of flowing polymers in microfluidic devices. Using different mesoscopic simulation methods, we explore the dynamics of polymers in dilute and non-dilute, but unentangled, solutions under flow in confined geometries, namely periodic pressure-driven sudden contraction-expansion channel with contraction dimension comparable to R_g, the polymer radius of gyration.

We first choose the method Stochastic Rotation Dynamics (SRD) to study this problem. But before SRD can be confidently used for quantitative calculations,there is a need to benchmark SRD for both fluid dynamics and polymer dynamics. We first examine the accuracy of SRD for contraction flow against results from the finite element method. We show that SRD results are influenced by unphysical compressibility effects due to the ghost-like SRD fluid particles, and we can minimize this effect by lowering the Mach number via adjusting different SRD parameters. We next examine the accuracy of SRD for isolated polymers against standard theoretical and Brownian dynamics (BD) results. We show that the main error is due to an inertial effect that finite bead mass has on polymer hydrodynamics, and we find that this effect is negilible at $L_M / R_g < 0.1$, where L_M is the distance over which polymer bead inertia is lost due to collisions with solvent.

We finally apply SRD to study polymer migration in microfluidic contraction flow. The similarity in results from SRD and BD without hydrodynamic interaction (HI) at low Weissenberg number Wi (<10) indicates that HI has only a weak effect on polymer migration in our geometry. We find that the polymer migration is primarily due to streamline curvature on a length scale comparable to the polymer radius of gyration, which produces a migration velocity

that is proportional to Wi^2. And using the central limit theorem, we show that streamline-curvature-induced (SCI) migration can, in long periodic geometries, lead to clear separation of polymers by molecular length. We find that while there are other mechanisms that can also cause polymer migration, SCI migration is the dominant mechanism for the polymer migration in our contraction flow at $Wi<10$.

Chapter 1

Introduction

Learning to think on an entirely different scale is always a new and exciting challenge to fulfill the curiosity of human beings. We are not satisfied with understanding the small, yet already colorful enough world around us. Owe to the advanced technology, we are either raising the head to the starry sky, the vast universe up to the scale of light-years, where the theory of relative is revealed; or dropping the head to the electron sea, the teeny world down to the scale of nanometers, where quantum mechanism is discovered. While in the field of fluid mechanism, we don't need to go too far, just down to the micrometer scale, there are already exhibiting exciting physics. This is the novel field of microfluidics, emerging in the beginning of 1980s, which attributes to the advances in the microfabrication.

The development in the recent soft lithography enables the microfluidic devices to be fabricated inexpensively and reliably with tailored geometries where the small-scale flows can be precisely controlled. Several schematics of microfluidic devices are shown in Figure 1.1[Mai *et al*. (2012)]. The flows in the micro-geometry are commonly driven by moving boundaries, pressure gradients, or electric field gradients. The microfluidic devices provide a powerful platform to study the dynamics of soft materials. Meanwhile they are also used as powerful tools for a wide variety of applications, especially in the biological systems, such as geonomics[Jing, *et al*.(1998), Zhou, *et al*.(2003)], blood analysis and separations[Faivre *et al*.(2006)]. In this thesis, we are particularly

interested in the device of a pressure-driven planar contraction channel (similar to the schematic (b) in Figure 1.1), since it holds a promising potential application of to the separation of polymers, cells, emulsion droplets and other deformable objects.

The most conventional and widely used polymer separation technique is size-exclusion chromatography (SEC), which was first developed in 1955 by Lathe and Ruthven (1956). A typical SEC method is gel permeation chromatography (GPC), which can be traced back to Moore (1964). The GPC techniques separate based on polymer size or radius of gyration. Due to the size exclusion, the large molecules explore fewer areas than the smaller ones do as they pass the column, and thus go through faster, resulting in the separation. The flow rates in GPC columns are typically too small to deform the polymer molecules; that is the Weissenberg number Wi, which is the characteristic shear rate multiplied by the polymer relaxation time, is usually very small, much less than unity ($< 10^{-2}$) [Moore(1964)].

Meanwhile, techniques for separating biological molecules of different sizes have been developed in parallel with the evolution of molecular biology. Decades ago, Dill and Zimm [Dill(1979), Dill and Zimm(1979)] proposed a rheological separation method for DNA molecules based on the radial migration of the DNA that occurs when DNA solutions are subjected to flow between rotating concentric cylinders or cones. This radial migration is actually caused by streamline curvature. We will discuss this mechanism in detail later in this thesis. However this technique has not been widely used ever since. But DNA separation is an active area, since it is important for numerous applications in biotechnology and medicine, for example, the sequencing of genomes, and genetic arrays to identify diseases. The use of the microfluidic devices for micro-scale DNA separation have been increasingly studied, since those devices provide great advantage in reducing separation time, sample volume and cost per

analysis. DNA molecules are charged polymers, and so far the dominant micro-scale separation strategy is through micro-capillary electrophoresis (μCE). With different separation matrices, μCE can separate DNAs with length ranging from tens of base pair (bp) up to 1000 bp, and the typical separation time is about 63 minutes to 96 minutes with a resolution as high as ~0.35 [Ashton *et al*. (2003)], or even faster at a cost of lowering separation resolution period. For example, Xu *et al*. (2002) reported that using hydroxypropylmethylcellulose (HPMC) with polyhydroxy additives, DNA between 72 bp and 1353 bp could be separated in 170 seconds with a resolution of 10. Meanwhile novel separation strategies using entropic traps, arrays of pillars and Brownian ratchets are also being developed. For more detailed review on development of DNA separation since 2001, please refer to Ashton *et al*. (2003).

Hydrodynamics interaction (HI) was found to play an important role in microfluidic devices. Jendrejack *et al*. (2004) used Brownian Dynamics (BD) to study the polymer migration in a square straight channel and found that the HI between the polymer and wall can significantly thicken the depletion layer beyond that resulting from the size-induced depletion from the wall. The thickness of the depletion layer due to this wall-hydrodynamics-induced migration depends on the Weissenberg number, and thus can also be used for polymer separation.

Most recently, Faivre *et al*. (2006) reported that in a contraction channel, size exclusion of the cells from the wall can be enhanced via the contraction geometry, and proposed an application of such focusing effect for separation of the red blood cells from the suspending plasma. This effect actually results from a depletion-convection coupling. That is the depletion layer whose thickness is the size of the colloids in the narrow region of the contraction channel is convected along the streamline into the wide region. Within a certain distance in the wide region, the

colloids are depleted from a zone near the wall whose size is much larger than the size of the colloids, because the colloids don't have the time to diffuse across the convected depletion layer.

For separating biological cells based on their size or flexibility, the method we demonstrate in this thesis for prediction of polymer separation and then it can be further applied to design microfluidic devices for this purpose.

Among various mesoscopic methods, we first choose Stochastic Rotation Dynamics (SRD) to study the problem of polymer migration in a contraction flow. We choose this problem to illustrate to important two aspects: 1) the geometry and boundary conditions are complex; 2) the fluctuating or time-dependent hydrodynamic interactions (HI) are potentially important. To solve the flow field in a complex geometry, the finite element method (FEM) is excellent, but it is unsuitable for resolving fluctuating hydrodynamic interactions. Brownian dynamics (BD) with full HI is well developed for describing fluctuating hydrodynamic interactions, but becomes very cumbersome when HI is important in complex geometries. And thus in problems that contain a combination of aspects 1) and 2), SRD a promising method. However before SRD can be confidently used for quantitative calcualtions,there is a need to benchmark SRD for both fluid dynamics and polymer dynamics. We first examine the accuracy of SRD for contraction flow against results from FEM in Chapter 2. And then we examine the accuracy of SRD for isolated polymers against standard theoretical and BD results in Chapter 3. With the findings in the first two chapters, we then safely use SRD for studying polymer migration in a periodic pressure-driven contraction flow with contraction dimension comparable to the polymer radius of gyration. To charaterize the influence of the HI, we compare the results from SRD with those from BD simulations without HI. Interestingly, the similarity in results from those two simulations indicates HI has only a weak effect on polymer migration in this geometry at low Weissenberg

number Wi (<10), and inexpensive BD simulations without HI are adequate to predict the single polymer migration accurately in the contraction problem studied here. And using central limit theorem, we demonstrate the potential application of this microfluidic device for polymer separation. Finally in Chapter 5, we further investigate the influence of polymer concentration on the polymer migration and separation. We conclude and discuss the outlook in Chapter 6.

References

Ashton, R., C. Padala and R.S. Kane, "Microfluidic separation of DNA," *Current Opinion in Biotechnology* **14**, 497-504 (2003).

Dill, K.A., "Theory for the separation of very large DNA molecules by radial migration, " *Biophys. Chem.* **10**, 327-334 (1979).

Dill, K.A. and B.H.Zimm, "A rhelogical separator for very large DNA molecules," *Nucleic Acids Res.* **7**, 735 (1979).

Faivre, M, M. Abkarian, K. Bickraj and H.A. Stone, "Geometrical focusing of cells in a microfluidic device: An approach to separate blood plasma," *Biorheology* **43**, 147-159 (2006).

Jendrejack, R. M., D.C. Schwartz, J. J. de Pablo and M. D. Graham, "Shear-induced migration in flowing polymer solution: simulation of long-chain DNA in microchannels", *Journal of Chemical Phycics* **120**, 2513 (2004).

Lathe, G.H and C.R.J. Ruthven, "The Separation of Substance and Estimation of their Relative Molecular Sizes by the use of Columns of Starch in Water," *Biochem J.* **62**, 665–674 (1956).

Mai, D.J., C. Brockman and C.M. Schroeder, "Microfluidic systems for single DNA dynamics," *Soft Matter* **8**, 10506 (2012).

Moore, J.C., "Gel permeation chromatography. I. A new method for molecular weight distribution of high polymers," *J. Polym. Sci.* **2**, 835-843 (1964).

Jing, J, J. Reed, J. Huang, *et al*., "Automated high resolution optical mapping using arrayed, fluid-fixed DNA molecules," *Proc. Natl. Acad. Sci. USA* **95**, 8046-8051 (1998).

Xu, F., M. Jabasini, and Y. Baba, "DNA separation by microchip electrophoresis using low-viscosity hydroxypropylmethylcellulose-50 solutions enhanced by polyhydroxy compounds, " *Electrophoresis* **23**, 3608-3614 (2002).

Zhou S., E. Kvikstad, A. Kile, *et al*., "Whole-genome shotgun optical mapping of rhodobacter sphaeroides strain 2.4.1 and its use for whole-geonome shotgun sequence assembly," *Genome Res.* **13**, 2142-2151 (2003).

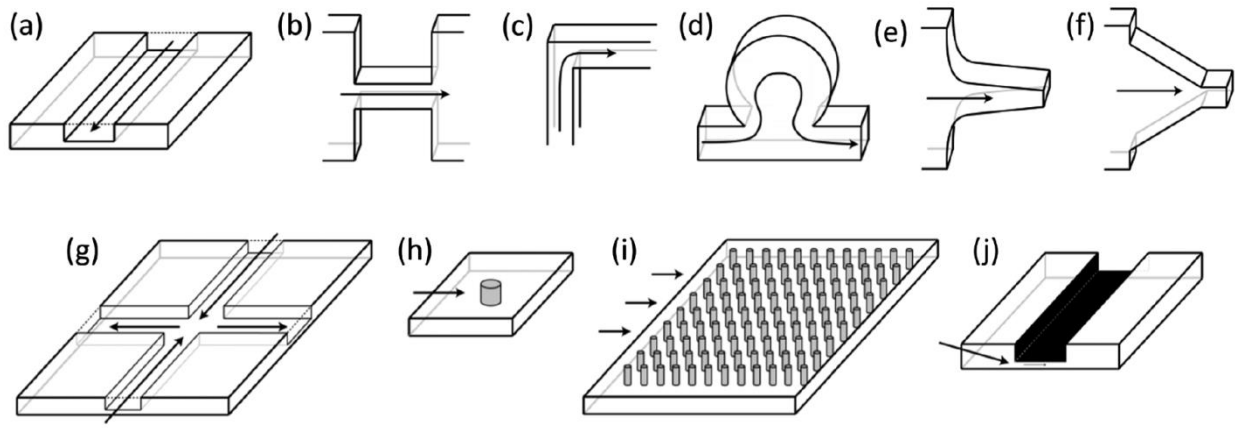

Figure 1.1: Schematics of several microfluidic platforms. For each schematic, the direction of fluid flow is indicated by the arrows.(a) Straight channel; (b) planar micro-contraction; (c) planar 90 bend; (d) channel-based micro-curvilinear flow device; (e) hyperbolic contraction;(f) linear converging channels; (g) cross-slot geometry; (h) single obstacle; (i) ordered array of obstacles; and (j) slit-like confinement. Adapted from Mai *et al*., *Soft Matter* **8**, 10506 (2012).

Chapter 2

Stochastic Rotation Dynamics Simulation of Fluid

In this chapter, the algorithm of Stochastic Rotation Dynamics (SRD) is introduced. And the accuracy of SRD simulations on the fluid dynamics is carefully examined. One main issue with SRD fluid is that, since SRD is uses soft particles to carry momentum, it contains unphysical high compressibility. To assess this effect, compressible SRD fluid is explored in a periodic pressure-driven planar contraction channel. We find that the SRD results are influenced by compressibility effects due to the relatively large value of Ma, the Mach number, in SRD simulations. Ma can be lowered by either increasing the temperature, decreasing the kinematic viscosity or scaling up the system dimension, while keeping fixed Re, the Reynolds number. By varying the SRD parameters, we can reduce density variations to less than 2%, and the error of the flow field, compare with the results from finite element methods, are only around 1%.

2.1. Introduction

The Stochastic Rotation Dynamics (SRD) particle-based simulation method was developed by Malevanets and Kapral [Malevanets and Kapral (1999)] a decade ago, and is now frequently referred to as multi-particle collision (MPC) dynamics. It treats the fluid elements as particles governed by simple interaction rules that preserve linear momentum and energy. (Note that in SRD, angular momentum is not generally conserved. For a detailed discussion of this topic, please refer to Götze *et al*. (2007). The SRD method leads to a significant algorithmic simplification relative to methods that treat the solvent as a continuum (such as the finite element

method (FEM) or Brownian dynamics (BD) simulations), for problems that require tracking the transfer of momentum between fluid, walls or boundaries, and Brownian objects, such as colloids, polymer molecules, bacteria, etc. [Hecht *et al*. (2005); Ali and Yeomans (2005); Lee and Karpral (2005); Earl *et al*. (2007); Yeomans (2006); Watari *et al*. (2007)]. SRD is especially promising for situations where fluctuating or time-dependent hydrodynamic interactions are important (which makes FEM unattractive), but the geometry or boundary conditions are complex (which makes BD cumbersome.). Before the SRD is applied to study such problems, the accuracy of SRD simulations on both the fluid dyanmics and polymer dynamics need to be examined. In this chapter, we benchmark SRD for the Poiseuille and contraction flow against analytical and finite element method (FEM).

2.2. SRD algorithm

In SRD, the fluid is modeled by N particles, each of which is characterized by its position $\mathbf{r}_i$ and velocity $\mathbf{v}_i$, with i=1,2…N. For simplicity, all the fluid particles are assigned the same mass m. The algorithm consists of two steps: a *streaming* step followed by a *collision* step after a discrete time step Δt. We refer to this Δt as the collision time, and note that in SRD the time step Δt is not purely a computational parameter, since its value influences the physical properties of the fluid, such as the fluid viscosity. It does this because sets the mean free path of a fluid "particle" between collisions with other fluid particles, and therefore influences rates of momentum transfer. We will discuss this in greater detail after we summarize how the system evolves in the *streaming* and *collision* steps.

In the *streaming* step, the fluid particles without external force simply follow Newton's law, with the positions updated as:

$$\mathbf{r}_i(t+\Delta t) = \mathbf{r}_i(t) + \mathbf{v}_i(t)\Delta t \tag{2.2.1}$$

In the *collision* step, the particles are sorted into the cells of a *d*-dimensional cubic lattice (where typically $d = 3$) with lattice spacing *a*. The collision is carried out by first taking the difference between each particle's velocity and the center-of-mass velocity of all particles in the cell, and then rotating this velocity difference around a random rotation axis through a rotational angle α. Then the center-of-mass velocity is added back. Thus,

$$\mathbf{v}_i(t^+) = \mathbf{v}_{\mathrm{CoM},i}(t^-) + \mathcal{R}(\alpha)[\mathbf{v}_i(t^-) - \mathbf{v}_{\mathrm{CoM},i}(t^-)] \tag{2.2.2}$$

where $\mathcal{R}(\alpha)$ is a stochastic rotation matrix, $t^{+/-}$ refers to the time after/before the collision and $\mathrm{v}_{\mathrm{CoM},i} = \sum_j^{(i)} (m\mathrm{v}_j) \Big/ \sum_j^{(i)} m$ is the center of mass velocity of all particles in the collision cell where the *i*-th particle is located.

To guarantee Galilean invariance, a random shift of the collision cells before executing the *collision* step has to be performed, and after the *collision* step, the particles are shifted back to their original positions. Details of this process are described in [Ihle and Kroll (2001)].

To avoid development of a spurious temperature profile, after the *collision* step and the random shift of particles is reversed, a thermostat is applied to each collision cell to adjust the local collision cell temperature to the desired system temperature *T* [Watari *et al*. (2007)]. Although in Ref. [Watari *et al*. (2007)], the thermostat is applied after the *streaming* step, we found for polymer dynamics at equilibrium, the point in the computational cycle at which the thermostat is applied makes little difference in the results. (The dynamic quantities for the polymer chains we tested agree within the statistical error.) Detailed discussion of this cell-level thermostat is described in [Huang *et al*. (2010)].

2.2.1. SRD parameters

In the *collision* step, collisions with a large rotational angle dominate the collision contribution to the viscosity. The time the system takes to relax to the equilibrium state, i.e. time required for the particles velocities to relax to their Maxwell-Boltzmann velocity distribution is proportional to α^{-2} [Ihle and Kroll (2001)].

The Schmidt number Sc, which is the ratio of the kinematic viscosity of the solvent to the diffusivity of the fluid particles, can be estimated as [Ripoll *et al*. (2005)]:

$$\mathrm{Sc}=\frac{\nu}{D}\approx\frac{1}{108}\frac{ma^2}{k_\mathrm{B}T}(1-\frac{1}{\rho})^2(\frac{\alpha^2}{\Delta t})^2 \qquad (2.2.1.1)$$

where α is the rotational angle in radians, ν is the kinematic viscosity and D is the self-diffusion coefficient. Liquids typically have high Sc, which therefore requires a small Δt. Note that the mean free path, $\lambda\simeq\Delta t\sqrt{k_\mathrm{B}T/m}$, thus $\mathrm{Sc}\propto\left(a/\lambda\right)^2$. Actually depending on the mean free path λ, two distinct regimes are identified [Ripoll *et al*. (2005)]: 1) In the "particle regime" for which $\lambda\gg a$ (a is the size of the collision cell), i.e. $\mathrm{Sc}\ll 1$, the molecular-chaos assumption holds, and the dynamics is gas-like; 2) In the "collective regime" for which $\lambda\ll a$, i.e. $\mathrm{Sc}\gg 1$, many-body correlations occur, leading to strong hydrodynamic interactions, and the dynamics is fluid-like.

Using kinetic theory, the viscosity η can be calculated theoretically and the validity of this calculation has been checked against SRD simulations [Kikuchi *et al*. (2003); Ihle and Kroll (2003); Ihle *et al*. (2005)]. The momentum transfer in the *streaming* and *collision* steps both contribute to the viscosity. Therefore in 3D, $\eta=\eta_\mathrm{kin}+\eta_\mathrm{col}$:

$$\eta_{\text{kin}} = \frac{\rho k_{\text{B}} T \Delta t}{a^3}\left[\frac{5\rho}{(\rho - 1 + e^{-\rho})(4 - 2\cos\alpha - 2\cos 2\alpha)} - \frac{1}{2}\right] \tag{2.2.1.2}$$

$$\eta_{\text{col}} = \frac{m(1-\cos\alpha)}{18a\Delta t}(\rho - 1 + e^{-\rho}) \tag{2.2.1.3}$$

where $\eta_{\text{kin/col}}$ is the kinetic/collisional contribution to viscosity from the *streaming*/*collision* step and ρ is the average number of fluid particles per collision cell, i.e. their number density.

In the simulations, we choose units such that $a = 1, m = 1, k_{\text{B}}T = 1$ and scale the length and time as $\hat{x} = x/a, \hat{t} = t\sqrt{k_{\text{B}}T/ma^2}$. Thus, the length unit (LU), time unit (TU), and mass unit (MU) in our SRD simulations are $\text{LU} = a, \text{TU} = \sqrt{ma^2/k_{\text{B}}T}$ and $\text{MU} = m$ respectively.

2.2.2. No-slip boundary condition

To apply a no-slip boundary condition in simulating SRD fluid, we assign wall cells (as those cubes on the edges of the geometry shown in Figure. 2.4) along the wall boundaries. To realize the no-slip boundary condition, in the *streaming* step the bounce-back rule is applied. That is, if a particle intersects the boundary at time $t + \Delta t'$ during a collision time step Δt, the particle velocity relative to the wall $\tilde{\mathbf{v}} \equiv \mathbf{v} - \mathbf{v}_{\text{wall}}$ is completely reversed, i.e. $\tilde{\mathbf{v}} \to -\tilde{\mathbf{v}}$, so that the average relative velocity of the fluid near boundary is zero. And in the remainder of the collision time step, the particle is propagated from the point of contact with the boundary using this new velocity [Whitmer and Luijten (2010)]. For simplicity, we replace $\Delta t'$ with its average value $\frac{\Delta t}{2}$ so that at the end of *streaming* step after the bounce-back, the position of the particle is updated as,

$$\mathbf{r}_i(t+\Delta t) = \mathbf{r}_i(t) + \mathbf{v}_{\text{wall}}\frac{\Delta t}{2} \tag{2.2.2.1}$$

$$\mathbf{v}_i(t+\Delta t) = \mathbf{v}_{\text{wall}} - \mathbf{v}_i(t) \tag{2.2.2.2}$$

where $\mathbf{v}_{\text{wall}}$ the velocity of a moving wall. For a stationary boundary, the particle simply restores to its original position at the beginning of the *streaming* step, and its velocity is reversed.

However since a pure bounce-back rule fails to guarantee no-slip boundary conditions, further treatment is needed in the *collision* step. If *n*, the number of fluidic beads shifted into a wall cell after the random shift is less than ρ, the average number of the fluidic beads per cell, then $\rho - n$ "phantom" beads with velocities drawn from a Maxwell-Boltzmann distribution of zero average velocity and temperature *T* are added to that wall cell to participate in the collision for momentum exchange [Lamura *et al*. (2001)]. After this collision, these "phantom" beads are destroyed. New ones created with new random velocities whenever they are needed for collisions in the wall cells.

2.3. Numerical results

2.3.1. Effect of discretization of the geometry

In SRD, the geometry is gridded into cubic collision cells, and the kinetic energy and linear momentum are conserved in each collision cell during the *collision* step. So to accurately simulate the flow field, there needs to be enough collision cells to represent the geometry.

Here, we investigate this issue using Poiseuille flow in a channel with *x* the gap direction, and pressure drop applied along the *y*-direction. The boundaries are represented by two lines of wall cells. No-slip boundary conditions are imposed on the channel walls as described in Section

2.2.2. With this no-slip boundary condition, the flow field doesn't extrapolate to zero at the boundary but rather half way into the wall cells. Therefore the wall cell contributes half of its width to the width of the channel. In Figure 2.1, the solid curve is the theoretical Poiseuille flow calculated using the channel width with the contribution from the wall cell, which matches the SRD predictions, given by circles.

Figure 2.2 shows how the error reduces to zero as the number of the collision cells across the slit in the *x*-direction increases, where the error is calculated as

$$\text{Error} = \frac{|Q - Q_0|}{Q_0} \tag{2.3.1.1}$$

Here Q and Q_0 are the volumetric velocity per unit channel depth, i.e. in the *z*-direction, from the SRD simulation and theory respectively. We can see that with only three collision cells, the error is still only about 10%. The error depends on the number of collision cells across the slit, not on how finely we grid the geometry for calculating the velocity of the fluid at each grid cell (i.e. the grid size for the flow field can be less than a, the size of collision cell). As shown in Figure 2.1), the squares, for which the resolution of the flow field is a, agree with the cross-dashed curve, for which the resolution is $a/4$; both of them is below the solid theoretical curve, since for both there are only three collision cells along *x*-direction to represent the slit channel.

2.3.2. Effect of Schmidt number on the solvent viscosity

As Sc decreases, the SRD fluid becomes more gas-like, with one consequence that the fluid viscosity predicted by Eq. (2.2.1.2-2.2.1.3) becomes less accurate. Figure 2.3 shows that if Sc is reduced from 40 to 10 by either increasing the temperature T, or increasing the collision time Δt, the simulated flow fields deviate slightly away, about 7%, from that predicted using the

analytical viscosity. Hence the viscosity that would be obtained by fitting the flow profile to the analytic one is about 7% higher than the analytical value.

2.3.3. Effect of compressibility of SRD fluid

SRD uses phantom particles to carry momentum and recovers the Navier-Stokes equation with an ideal-gas equation of state according to an *H*-theorem; therefore SRD fluid is highly compressible [Malevanets and Kapral (1999)]. The non-uniformity of the solvent density in a complex geometry resulting from this compressibility was shown by Götze *et al*. (2007). Zhao *et al*. (2013) compared the compressible SRD fluid with the DPD fluid, by studying an electro-osmotic flow along inhomogeneously charged surfaces, where the compressibility is caused by the complex flow in a simple geometry.

Here we investigate the compressibility of the SRD fluid in a complex geometry, a periodic pressure-driven planar contraction channel, shown in Figure 2.4 The simulation box has dimensions $L_1 \times L_2 \times L_3$, where L_3 is the out-of-plane dimension, not shown in Figure 2.4 The lower and upper wide chambers are connected by a narrow channel with width *w* and length *h*. A constant acceleration *g* is applied along the *y* direction to drive the flow. We apply periodic boundary conditions along *y* and *z* directions, and no-slip boundary conditions at the walls (i.e. those cubes on the edges of the geometry).

We set the dimensions of the simulation box to be L_1=21, L_2=18, L_3=20 and the narrow channel is given dimensions of *w*=3, *h*=6. Taking into account the size contribution from the wall cells, the contraction ratio is (21+1)/(3+1) = 5.5. We run the simulation with the parameters ρ = 5 and α = 150°. We first choose T = 1, Δt = 0.05, and impose the acceleration *g*=0.02. The circles in Figure 2.5 show the resulting solvent density *n* along the *y*-direction (and averaged over the other

dimensions of the geometry). We can see, due to the compressibility, in the wide chamber the solvent density is about 10% lower than ρ, the average solvent density, at the slit exit (dash line (2) in Figure 2.4), gradually increases and finally accumulates to about 10% higher than ρ at the slit entrance (dash line (1) in Figure 2.4).

The compressibility is controlled by Ma, the Mach number, which is the ratio of the characteristic flow speed V to the sound speed V_{sound}. The sound speed for the SRD fluid is $V_{\text{sound}} = \sqrt{5k_{\text{B}}T/3m}$ [Tüzel *et al*. (2006)]. We take the characteristic flow speed to be $V = gw^2/8\nu$, the maximum speed of the Poiseuille flow in a slit with the same width as the narrow part of the contraction channel, where ν is the kinematic viscosity. Therefore Ma, as defined here is:

$$\text{Ma} \simeq \frac{gw^2/8\nu}{\sqrt{5k_{\text{B}}T/3m}} \tag{2.3.3.1}$$

Note due to the contraction, the maximum speed of the contraction flow will be larger than $gw^2/8\nu$; thus the actual Ma in the system will be higher than the value from Eq. (2.3.3.1). To lower the compressibility without otherwise changing the flow field, we want to lower Ma but keep Re, the Reynolds number, the same. Using the characteristic speed discussed above to define Re,

$$\text{Re} = \frac{wV}{\nu} = \frac{gw^3}{8\nu^2} \tag{2.3.3.2}$$

which is actually one eighth of the so-called "Galilei number," $\mathrm{Ga} = \frac{gw^3}{\nu^2}$. From Eq. (2.3.3.2), Ma is related to Re as $\mathrm{Ma} = \mathrm{Re}\frac{\nu/w}{\sqrt{5k_\mathrm{B}T/3m}}$. Therefore, keeping the same Re by adjusting acceleration g correspondingly, the Mach number can be lowered either by decreasing the kinematic viscosity ν or increasing the temperature T, or increasing the system size, i.e. w, which will be at the cost of increasing the simulation time. Follow the discussion above, we lower Ma by half via those three methods. As shown in Fig. 2.5, we thereby get a much more uniform solvent density. And at the slit entrance and exit, where the fluid is most compressed, the deviation in solvent density from the average value is reduced from 10% to only about 3%.

In addition, as discussed in Section 2.3.1, the limited number of collision cells across the narrow channel introduces some error. Despite these two sources of error, the SRD flow field at Ma = 0.02 as shown in Figure 2.7 is in good agreement with the nearly exact Stokes flow obtained from a finite element method (FEM) at Re = 0 as shown in Figure 2.8. And the error of the flow field calculated from Eq. (2.3.1.1) is less than 1%.

2.4. Summary

In this chapter, we benchmark SRD for simulating contraction flow against finite element method (FEM). SRD algorithm implies at least three aspects may affect the accuracy of the solved flow field.

1) The discretization of the SRD flow field. Because of the geometry is gridded into collision cells, to accurately simulate the flow field, there expects to need to be enough collision cells to represent the geometry. We find the accuracy of the flow field is weakly affected by this discretization. We test SRD by simulation the Poiseuille flow in a slit channel, and find with

a minimum three collision cells along the slit to present the channel, the error is only within 10%.

2) The Schmidt number Sc. Sc determines the dynamic regime SRD simulates. When $Sc \ll 1$, the dynamics is gas-like, and when $Sc \gg 1$, the dynamics is fluid-like. We find if Sc > 10, the fluid viscosity predicted by the analytic expression from kinetic theory is within 10% away from the viscosity calculated from fitting the parabolic slit Poiseuille flow profile.
3) The compressibility of the SRD fluid. Since SRD uses soft particles to model the fluid, the compressibility is unavoidable in a complex geometry, and will influence the flow field. We quantify this influence in a contraction flow. The compressibility is controlled by Mach number Ma. At Ma = 0.02, the error of the flow field from the accurate flow field from FEM is less than 10%. The maximum deviation of the solvent density from the average solvent density at the entrance and exit of the narrow region of the contraction channel is about 10%. And if we lower Ma to 0.01 while keeping Reynolds number the same via increasing temperature, lowering kinematic viscosity or scaling up the geometry, the compressibility is lowered so that the density deviation is lowered to less than 2%.

References

Ali, I. and J. M. Yeomans, "Polymer translocation: The effect of backflow,"*Journal of Chemical Physics* **123**, 234903(4) (2005) .

Earl, D. J., C. M. Pooley, J. F. Ryder, I. Bredberg and J. M. Yeomans, "Modeling microscopic swimmers at low Reynolds number," *Journal of Chemical Physics* **126**, 064703(12) (2007).

Götze, I. O., H. Noguchi and G. Gompper, "Relevance of angular momentum conservation in mesoscale hydrodynamics simulations," *Physical Review E* **76**, 046705 (9) (2007).

Hecht, M., J. Harting, T. Ihle and H. J. Herrmann, "Simulation of claylike colloids," *Physical Review E* **72**, p. 011408(16) (2005).

Ihle, T. and D. M. Kroll, "Stochastic rotation dynamics: A Galilean-invariant mesoscopic model for fluid flow," *Physical Review E* **63**, 020201(4) (2001).

Ihle, T. and D. M. Kroll, "Stochastic rotation dynamics. II. Transport coefficients, numerics, and long time tails," *Physical Review E* **67**, 066706(17) (2003).

Ihle, T., E. Tüzel and D. M. Kroll, "Equilibrium calculation of transport coefficients for a fluid-particle model," *Physical Review E* **72**, 046707(11) (2005).

Kikuchi, N., C. M. Pooley, J. F. Ryder and J. M. Yeomans, "Transport coefficients of a mesoscopic fluid dynamics model," *Journal of Chemical Physics* **119**, 6388(12) (2003).

Lamura, A., G. Gompper, T. Ihle and D.M. Kroll, "Multi-particle collision dynamics: Flow around a circular and a square cylinder," *Europhysics Letters* **56**(3), 319-325 (2001).

Lee, S. H. and R. Karpral, "Two-particle friction in a mesoscopic solvent," *Journal of Chemical Physics* **122**, 214916 (6) (2005).

Malevanets, A. and R. Kapral, "Mesoscopic model for solvent dynamics," *Journal of Chemical Physics* **110**, 8805-8613 (1999).

Ripoll, M., K. Mussawisade, R. G. Winkler and G. Gompper, "Dynamic regimes of fluids simulated by multiparticle-collision dynamics," *Physical Review E* **72**, 016701(14) (2005).

Tüzel, E., T. Ihle and D.M. Kroll, "Dynamic correlations in stochastic rotation dynamics," *Physical Review E* **74**, 056702 (2006).

Watari, N., M. Makino, N. Kikuchi, R. G. Larson and M. Doi, "Simulation of DNA motion in a microchannel using stochastic rotation dynamics," *Journal of Chemical Physics* **126**, 094902(7) (2007).

Whitmer, J.K. and E. Luijten, "Fluid-solid boundary conditions for multiparticle collision dynamics", *Journal of Physics: Condensed Matter* 22, 104106 (2010).

Yeomans, J. M., "Mesoscale simulations: Lattice Boltzmann and particle algorithms," *Physica A* **369**, 159-184 (2006).

Zhao, T., X. Wang, L. Jiang and R.G. Larson, "Assessment of mesoscopic particle-based methods in microfluidic geometries," *Journal of Chemical Physics* **139**, 084109 (2013)

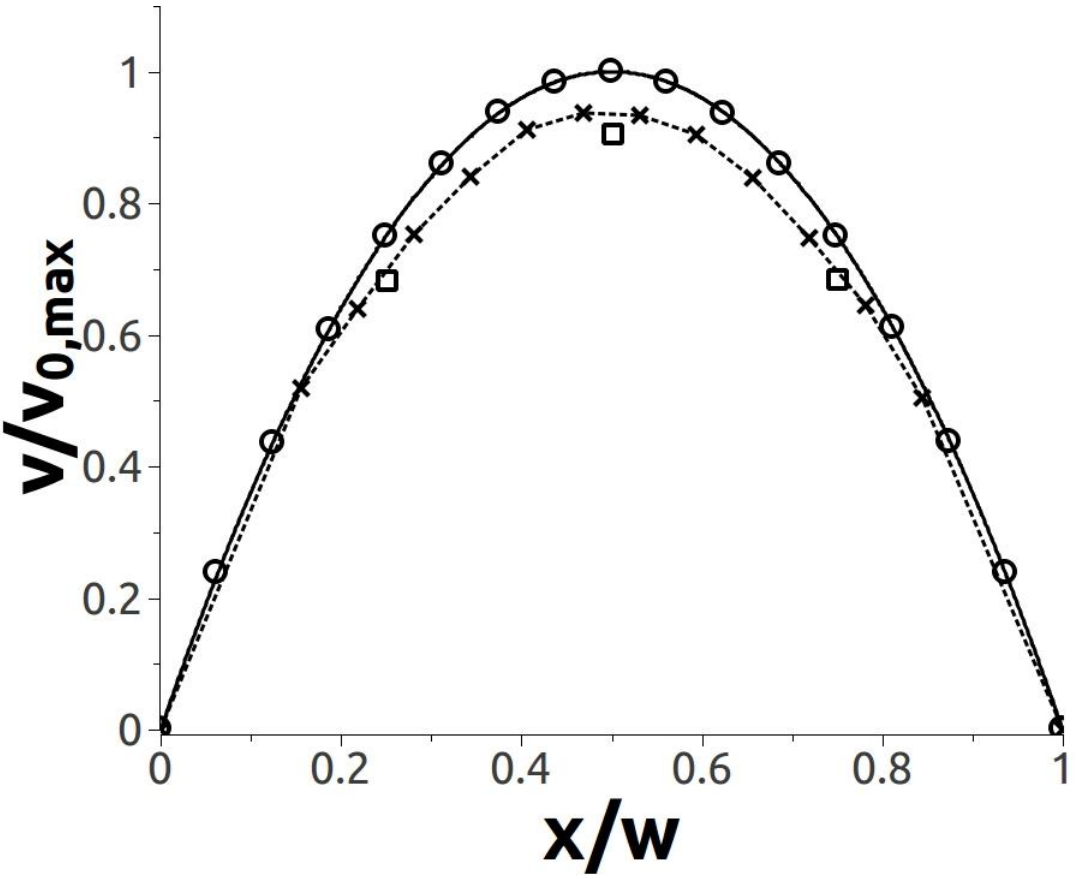

Figure 2.1: Flow profile normalized by $v_{0,max}$, the maximum velocity of Poiseille flow, calculated using the analytical viscosity from Eq. (2.2.1.2-2.2.1.3). Solid curve: theoretical parabolic profile; circles: SRD results with 15 collision cells across the slit; squares: SRD results with 3 collision cells across the slit; crosses and dashed curve: the same as for squares, but the resolution of the flow field is $a/4$, where a is the size of the collision cell.

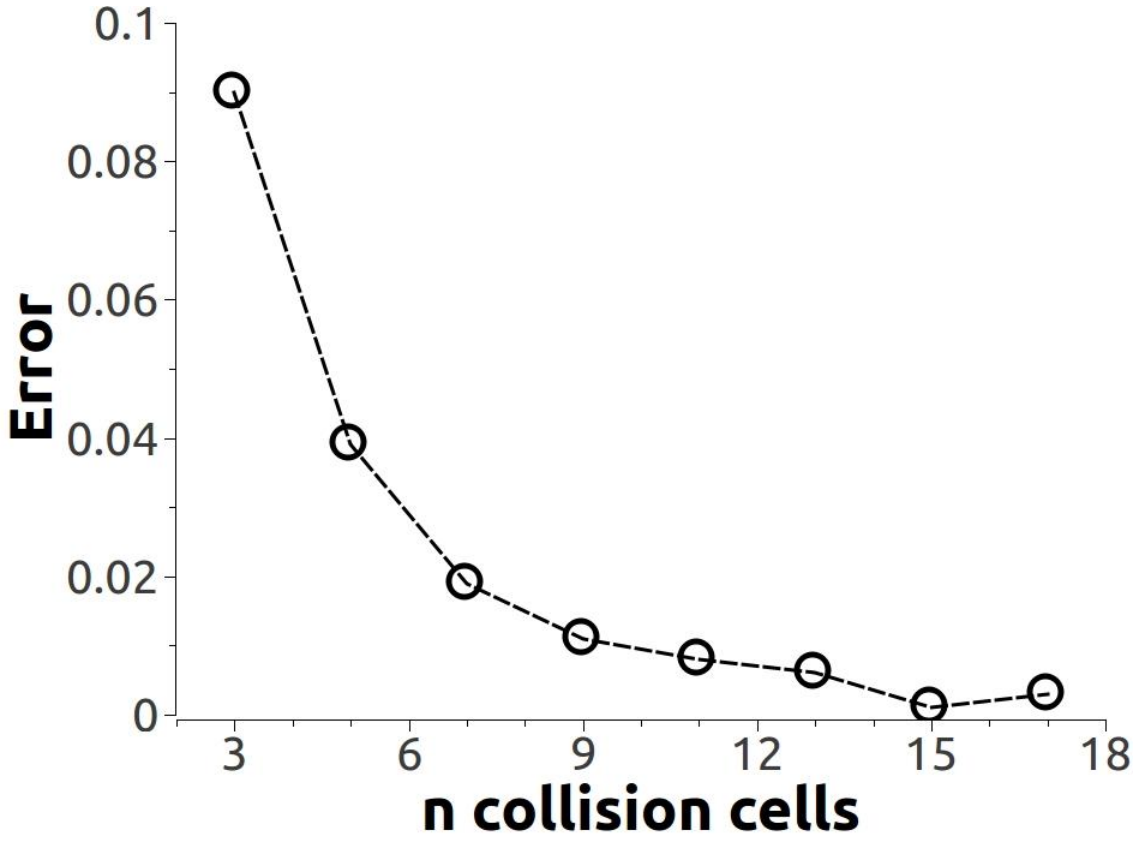

Figure 2.2: Error as calculated by Eq.(2.3.1.1) versus the number n of collision cells across the slit.

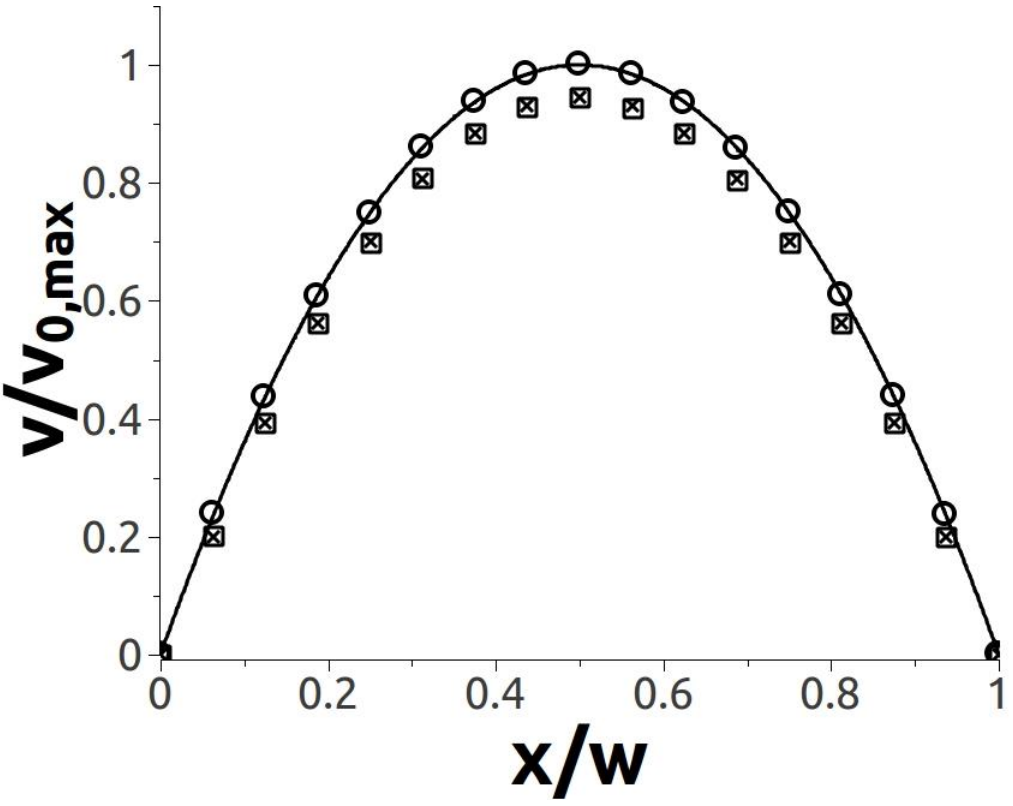

Figure 2.3: Poiseuille flow profiles with 15 collision cells across the slit at different Sc. Solid curve: theoretical parabolic profile; circles: Sc = 40 (T = 1, Δt = 0.05); squares: Sc = 10 (T = 4, Δt = 0.05); crosses: Sc = 10, (T = 1, Δt = 0.1).

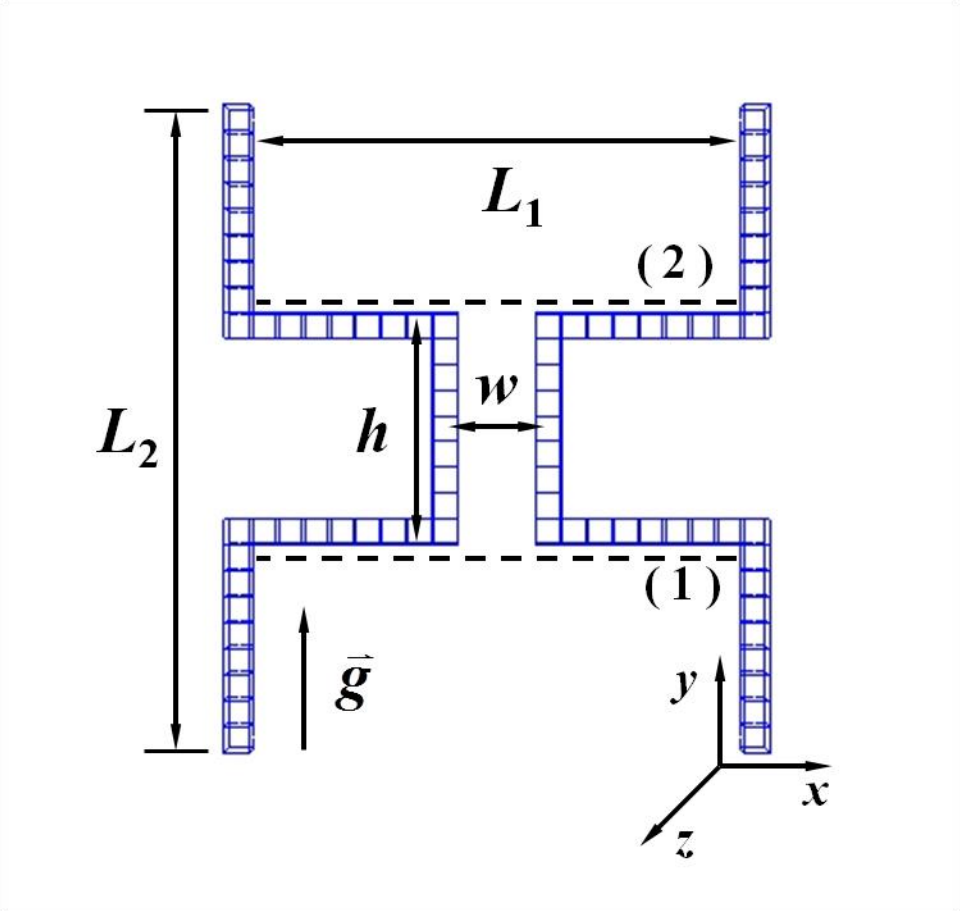

Figure 2.4: Geometry of the planar contraction channel

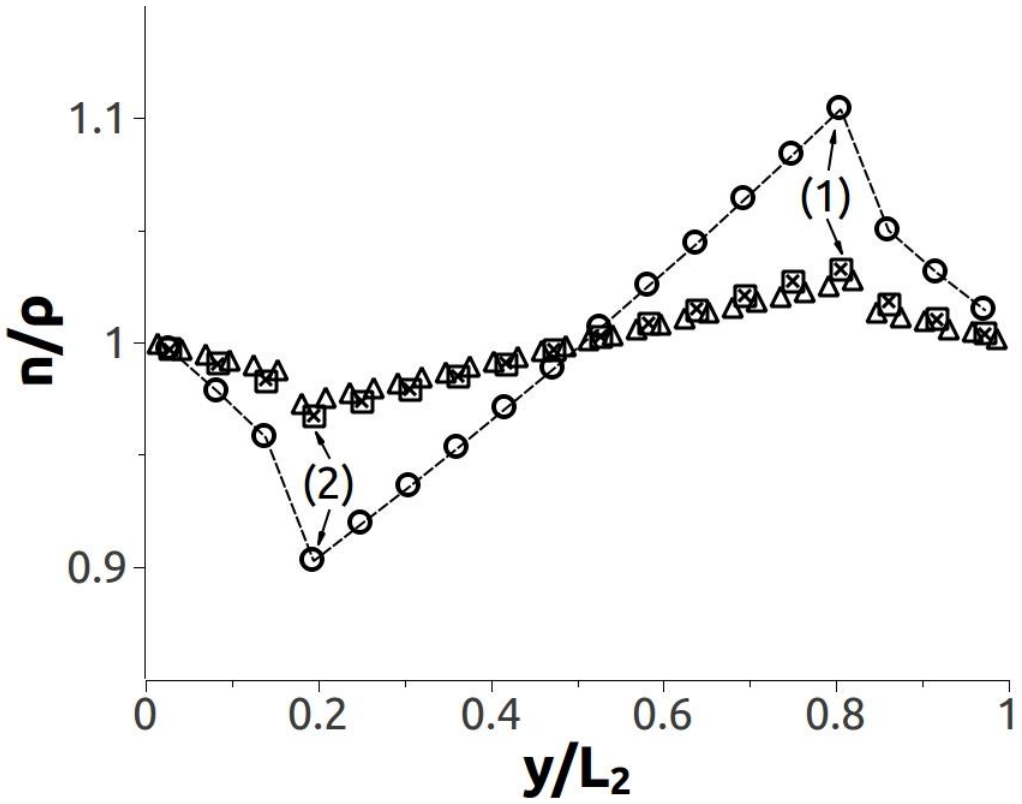

Figure 2.5: Solvent density n normalized by ρ, the average solvent density, along y-direction at Re = 0.06, averaged over the x and z dimensions of the geometry. (1) / (2) corresponds to the slit entrance/exit as shown by the dashed line (1) / (2) in Fig. 3. Circles: Ma = 0.02 (T = 1, Δt = 0.05, w = 4); squares: Ma = 0.01 (T = 4, Δt = 0.05, w = 4); crosses: Ma = 0.01 (T = 1, Δt = 0.1, w = 4); triangles: Ma = 0.01 (T = 1, Δt = 0.05, w = 8); where the value of w takes into account the contribution from the wall cells. Dashed lines are guides for the eyes.

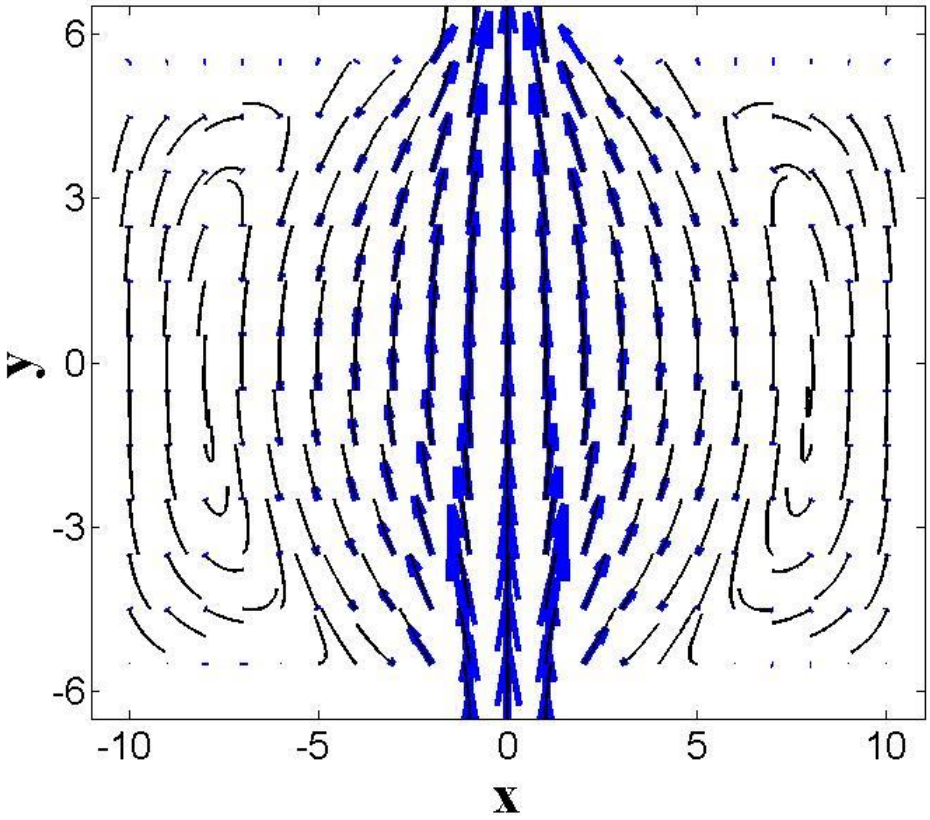

Figure 2.6 Flow field (arrows) and streamlines (black curves) in the wide chamber of the contraction channel at Re = 0.0 from FEM. The length of the arrow is proportional to the magnitude of flow field.

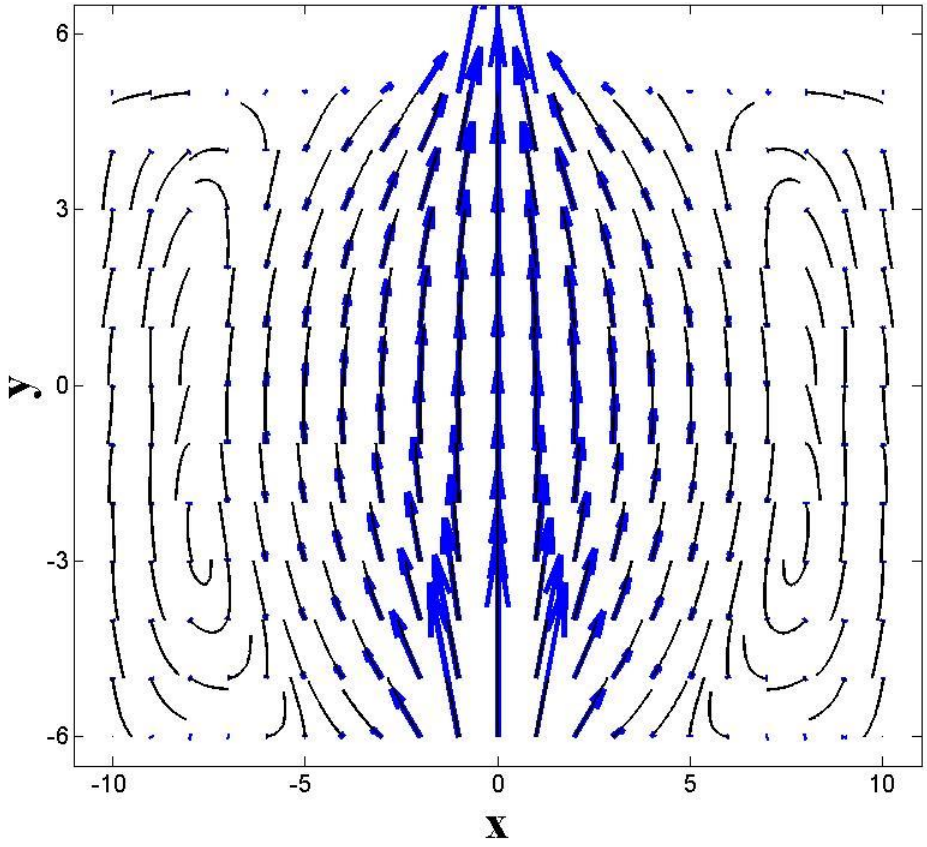

Figure 2.7: The same as Figure 2.6, expect the results are from SRD at Re = 0.06 with Ma = 0.02.

Chapter 3

Mesoscopic Simulations of Single Polymer Chain Dynamics

In this chapter, we examine carefully the accuracy of stochastic rotational dynamics (SRD) simulations for isolated polymer chains in a solvent, where SRD incorporates hydrodynamic interaction through momentum exchange ("*collisions*") between polymer beads and solvent beads, both of which are assigned mass. We show that the main error is due to the inertial effect that finite bead mass has on polymer hydrodynamics. We find that the inertial effect is negligible when R_g, the radius of gyration of the polymer chain is much larger than L_M, the distance over which bead inertia is lost due to collisions with solvent. For moderate hydrodynamic interaction (HI) good agreement is found between the rotational relaxation time simulated by SRD with that from normal mode analysis, and from Brownian dynamics (BD) simulations, even for short 5-bead chains. For dominant HI, for short chains, we can minimize the inertial effect by varying the ratio of polymer to solvent bead mass. For long chains ($R_g \gg L_M$) SRD and BD relaxation times agree, but are larger than those from normal mode analysis due to neglect of fluctuating HI in the latter. We also find that, using the same parameters, the SRD method can reproduce the BD results obtained by Jendrajack et al. for a λ-DNA chain in viscosified water.

3.1 Introduction

As discussed in the last chapter, SRD hold promising potential for solving problem where fluctuating or time-dependent hydrodynamic interactions are important , but the geometry or boundary conditions are complex. Before SRD can be confidently used for quantitative calcualtions of such problems, besides examining the accuracy of SRD simulations on fluid dynamics as we have done in the last chapter, there is also a need to benchmark SRD for isolated polymers against standard theoretical and Brownian dynamics (BD) results for such chains. We will do so in this chapter.

In the last chapter, we have briefly discussed the algorithm we use for SRD simulations of the fluid and how some relevant physical properties associated with the simulation parameters are set in SRD and the consequences of the choices made for these parameters. For more details and a comprehensive review of the SRD method, please refer to Gompper *et al*. (2008). In the following, we describe the simulation methods for polymers in both SRD and BD in Section 3.2, the method of determining the strength of HI in the SRD method in Section 3.3, the results from simulating isolated polymer chains in Section 3.4, and we summarize in Section 3.5.

3.2. Mesoscopic methods to simulate polymer

3.2.1. SRD-MD hybrid method

As usual, the polymer is modeled as a chain of N_b monomer beads connected by $N_s = N_b - 1$ springs. To study polymer dynamics using SRD, we follow previous work and couple a molecular dynamics (MD) simulation of the polymer to an SRD simulation of the fluid by numerically integrating Newton's equation of motion for the polymer chain using the velocity Verlet algorithm between collisions with a smaller time step Δt_{MD}. The polymer beads interact

with the solvent beads in the *collision* step. In this step, the solvent and any polymer beads that are in the same cell exchange momentum through the same collision rule as described above for the solvent beads; thus, the center of mass velocity of the cell $\mathbf{v}_{\mathrm{CoM},i}$ in Eq. (2.2.2) includes the polymer beads[Malevanets and Yeomans (2000)].

In SRD simulation, a polymer chain inevitably has a finite mass. While polymer behavior is usually considered in the Stokes regime where the inertial effect is negligible, in SRD the inertia may affect the polymer dynamics because the method relies on the inertia of relatively few polymer and solvent beads (relative to the number of molecules in a real system) to carry momentum, and so the bead inertia in SRD must be much larger than that of any real molecules. Here we seek to quantify the effect of this inertia and learn how to minimize its influence on polymer dynamics.

3.2.2. Brownian dynamics (BD) method

To compare with our SRD simulations, we also carried out standard Brownian dynamics simulations, with hydrodynamic interactions (HI) described by the Rotne-Prager tensor. The method is described thoroughly in other publications [Larson (2005)] and won't be discussed further here.

3.3. Determination of Hydrodynamic Radius

The coupling between the monomer and the solvent can be characterized by the hydrodynamic radius a_{H} of a polymer bead, which is related to the friction coefficient ζ by $\zeta = 6\pi\eta a_{\mathrm{H}}$. In Kikuchi *et al*. (2003), from the discretized Langevin equation of a monomer, an analytic expression for the friction coefficient was derived:

$$\zeta = \frac{M}{\Delta t}\left[1 - \frac{\langle \mathbf{v}(\Delta t) \bullet \mathbf{v}(0) \rangle}{\langle \mathbf{v}(0) \bullet \mathbf{v}(0) \rangle}\right] \tag{3.3.1}$$

where M and $\mathbf{v}$ are the mass and velocity of the monomer respectively. In this expression, only the velocity correlation between the 1st collision and 0th collision is considered. For the first collision time step, the molecular-chaos assumption holds, but as mentioned in the previous section, hydrodynamic interactions emerge at longer times from the many-body correlation. Therefore to capture the hydrodynamics at long times, we have to go beyond the molecular-chaos assumption. The many-body correlations of the fluid particles and the monomer bead enhances D_0, the self-diffusion coefficient of a single free monomer, and according to the Stokes-Einstein relation, results in a smaller friction coefficient than predicted by Eq. (3.3.1). For simulations of polymer dynamics, it is the long-time bead diffusion coefficient (or equivalently the long-time drag coefficient) that sets the relaxation dynamics of the chain, and hence is of most relevance for our simulations.

Due to inertia, in SRD, several collisions are required to enter the Stokes regime where the friction coefficient reaches its long-time asymptote. The velocity auto-correlation function (VCF), $\langle \mathbf{v}(\Delta t) \bullet \mathbf{v}(0) \rangle$ of a single free monomer bead with mass M is shown in Fig.1 for the simulation with parameters chosen to be $\rho = 10, \Delta t = 0.1, \alpha = 150^\circ$ in SRD units and $M = 10m$.

From Figure 3.1, we can see that the VCF drops to almost zero after about 20 collisions, after which the monomer bead almost enters the Stokes regime. But we can see the self-diffusivity of the monomer still keeps increasing very slowly as it approaches its long-time asymptote value $(2.16 \pm 0.02) \times 10^{-2}$ in SRD units for the inertial effect to vanish. In Fig. 1, the squares are from instantaneous diffusivity defined as

$$D_0(n\Delta t) = \frac{MSD(n\Delta t)}{6n\Delta t} \tag{3.3.2}$$

where n represents the n-th collision, and $MSD(n\Delta t) = \left\langle \int_0^\infty \mathrm{d}t \left[\mathbf{R}(t+n\Delta t) - \mathbf{R}(t)\right]^2 \right\rangle$ is the mean-square distance (MSD) of the monomer bead, where $\mathbf{R}(t)$ is the position of the monomer position at time t. From Eq. (3.3.2), we can derive the following expression for $D_0(n\Delta t)$:

$$D_0(n\Delta t) = \frac{\Delta t}{3} \sum_{i=0}^{n} \frac{n-i}{n} \left\langle \mathbf{v}(\Delta t) \bullet \mathbf{v}(0) \right\rangle - \mathrm{O}(\Delta t) \tag{3.3.3}$$

where $\mathrm{O}(\Delta t) = \frac{\Delta t}{6} \left\langle \mathbf{v}(0) \bullet \mathbf{v}(0) \right\rangle$. After taking the limit $n \to \infty$, Eq. (2.3) reduces to the discrete Green-Kubo relation [Ihle *et al*. (2005)]. The dashed line in Figure 3.1 is calculated from Eq. (3.3.3), and it agrees with the square symbols from the MSD. Note the first square on the left in Figure 3.1 is the diffusivity obtained from the short-time velocity correlation between the 1st collision and the 0th collision; its value is only 22% of that of the long-time diffusivity; and the short-time friction coefficient of Eq. (3.3.1) is 32% larger than the long-time drag coefficient calculated from D_0 via the Stokes-Einstein relation.

From Figure 3.1, we can see it takes the monomer multiple time steps to enter the Stokes regime where its VCF drops to zero. This velocity autocorrelation time scale for a monomer with mass M can be estimated by dimensional analysis to be $\tau_M \approx M/\zeta$. This characteristic time corresponds to a characteristic bead displacement length L_M over which the inertia of the monomer is lost to the solvent. L_M can be estimated as:

$$L_M \approx \tau_M \sqrt{\langle \mathbf{v}(\Delta t) \bullet \mathbf{v}(0) \rangle} = \sqrt{\frac{3M}{k_B T}} D_0 \tag{3.3.4}$$

where $\langle \mathbf{v}(\Delta t) \bullet \mathbf{v}(0) \rangle = {3k_B T}/{M}$ is the monomer's instantaneous velocity squared. The circles in Figure 3.2 show how L_M depends on the monomer mass *M*. The more massive the monomer, the larger the L_M is.

With the long-time self-diffusion coefficient D_0 of a single free monomer bead obtained numerically, the hydrodynamic bead radius a_H can be calculated via the following relation $k_B T / D_0 = \zeta = 6\pi\eta a_H$. If we hold the mass ratio $\gamma = {M}/{\rho m}$ fixed, a_H has a weak dependence on the simulation parameters $\Delta t, \rho, \alpha$. Either decreasing Δt, or increasing ρ or α results in more efficient collisions, and an increase in ζ. However, more efficient collisions result in a larger viscosity η, and this partly cancels out the effect on a_H, which is given by a ratio of ζ to η. Therefore, to control a_H, we adjust $\gamma = {M}/{\rho m}$, the ratio of polymer bead mass to solvent mass. The squares in Figure 3.2 show how a_H depends on γ. The larger the γ is, the larger a_H will be, because the heavier the monomer, the less diffusive it is, while the viscosity is kept the same.

To summarize, the hydrodynamic radius a_H in SRD is obtained by first numerically determining the monomer's diffusivity D_0 and then calculating the hydrodynamic radius via $k_B T / D_0 = \zeta = 6\pi\eta a_H$. Note that a_H is sensitive to the mass ratio $\gamma = {M}/{\rho m}$; the larger the γ is, the larger a_H will be.

3.4. Relaxation Dynamics of Polymer Chains at Equilibrium

To determine whether SRD captures accurately hydrodynamic interaction (HI) in polymer dynamics, we first study Gaussian chains in a theta solvent, i.e. with no excluded volume, at different HI strength. We compute the rotational relaxation time τ_1 and the self-diffusivity D from SRD simulations and directly compare these values with those obtained from a normal mode analysis [Bird *et al*. (1987)] instead of considering only the power-law exponent for the dependence of τ_1 and D on chain length, as in the previous work [Watari *et al*. (2007); Ripoll *et al*. (2004)]. For the short Gaussian chains used here ($N_b < 100$) in a theta solvent, the power-law exponents for the dependences of τ_1 and D on N_s differ somewhat from the values of 1.5 for τ_1, and -0.5 for D, which should be attained in the limit of dominant HI. Instead, these exponents depend on the strength of HI [Thurston (1974)].

We obtain the self-diffusivity D from the simulations by fitting the MSD of the center of mass, with $MSD(t) = 6Dt$. (Note in the expressions above, t is not the instantaneous time, but the time delay, the same as in the following expression of the auto-correlation of the 1st normal mode.) And to fit D, we exclude the early transient period prior to the Stokes regime (as shown in Fig. 1) from the fit region. The rotational relaxation time τ_1 is the decay time of the auto-correlation of the 1st normal mode, $N_1(t) = \langle \chi_1(t) \bullet \chi_1(0) \rangle$, where the 1st normal mode is obtained from the polymer bead coordinates as follows:

$$\chi_1(t) = \sqrt{\frac{2}{N_b}} \sum_{i=1}^{N_b} \mathbf{R}_i(t) \left[\frac{\pi}{N_b} \left(i - \frac{1}{2} \right) \right] \qquad (3.4.1)$$

where N_b is the number of beads, and $\mathbf{R}_i(t)$ is the position of *i*-th bead at time *t*. For a normal mode analysis of a linear stochastic equation (For example, the Rouse limit), the normalized auto-correlation of the 1st normal mode $n_1 = \frac{\langle \chi_1(t) \cdot \chi_1(0) \rangle}{\langle \chi_1(0) \cdot \chi_1(0) \rangle}$ decays as $\exp(-t/\tau_1)$, i.e. a strictly single exponential decay, thus the instantaneous rotational relaxation time defined as $\tau_1(t) = -\frac{t}{\ln[n_1(t)]}$ should be a constant over delay time *t*. Figure 3.3 plots the $\tau_1(t)$ of a 20-spring Gaussian chain from both SRD and BD simulations. We can see that due to inertia, τ_1 starts from a larger initial value because of the smaller instantaneous *D*, and quickly decays, but undershoots its steady-state value, which is attained at long time in the SRD simulation. The initial inertial regime is missing from the BD results, as expected, since the BD simulations contain no inertia, but the rise at later times also occurs in the BD simulations, similar to what is found in the SRD simulations. The rise in τ_1 is presumably due to a non-linear effect induced by HI. Because of HI, the 1st normal mode of the Gaussian chain calculated from Eq. (3.4.1) is no longer a pure eigenmode of the equations, but includes some nonlinear mixing from higher order eigenmodes. Due to mixing with these faster eigenmodes, τ_1 starts from a lower value, and then relaxes to its steady-state value. Therefore, to obtain τ_1, we exclude the early transient period from the fit region, and fit $N_1(t)$ to $A\exp(-t/\tau_1)$.

The angular brackets $\langle\ \rangle$ in the expressions of $MSD(t)$ and $N_1(t)$ refer to an ensemble average. Simulations with different random seeds yield different runs used to build up the ensemble. We run N simulations for each case and for each of these simulations we run for a total time of t_{sim}

with $t_{\text{sim}} > 10\tau_1$. For different polymer chains, we run enough simulations so that we can see a smooth transition of $\tau_1(t)$ to its long-time steady value as shown in Figure 4.3. The initial configuration of a polymer chain is set by fixing the separation of adjacent beads to the value R_s, the root mean square end-to-end length of a spring, and randomizing the orientation of the springs. Further randomization of the chain is achieved before averaging data by discarding the portion of the simulation data from the first period of $10\tau_1$, which is 10 times the polymer rotational relaxation time. As an alternative for Gaussian chains, because we set the initial overall chain configuration to be a random walk, only randomization of the separation of the adjacent beads, and not the whole chain configuration, is required before collecting data. Therefore, to discard less data and save simulation time, especially for long Gaussian chains ($N_s = 40$), we only discard initial data up to the time τ_1. To test this method, for short chains ($N_s = 20$), we used both randomization for a time τ_1 and randomization for $10\tau_1$ and showed that results from these two ways of randomization agree within statistical error. When we simulate DNA chains with excluded volume, however, the use of an initial random walk configuration is no longer appropriate, and so we always discard data for the first $10\tau_1$, instead of only τ_1. Because a single short run gives a response that is too noisy to estimate the relaxation time, we average multiple runs together (which is equivalent to a single long run, but faster using parallel computing) before computing τ_1 and *D*. To estimate the statistical error of our results, we divide the *N* repeat simulations with different random seeds into four groups, and compute τ_1 and *D* for each of the four groups. We then take the mean and standard deviation of the four data points for both τ_1 and *D*, and then calculate the standard error, which for this case is just the

standard deviation divided by square root of 4. Then we randomize the *N* simulations and divide them into another four groups, follow the same steps to compute another standard error, and then use the larger of the two standard errors as the estimation of the true standard error. In principle a better approach would be to use a larger number of groups (>10), so that the standard error for a single grouping would be more accurate. But then each group would be an average over fewer runs, and therefore each average would remains too noisy to extract a reasonable value of τ_1 or *D*. Hence, we obtain the standard error as the larger of the values from two different ways of grouping the runs into a small number of groups (4). In this way, it is much less likely that the standard error is artificially low due to the small number of groups.

We put the polymer chains in a cubic periodic simulation box of length $10R_g$ as in Ripoll *et al.* (2004), where R_g is the radius of gyration of a polymer chain.

3.4.1. Short 10-spring Gaussian chains with different mass ratios $M/\rho m$

In this sub-section, we consider the 10-spring Gaussian chains with different bead masses, and different strengths of HI. The strength of HI is characterized by the hydrodynamic coefficient h^*. For a Gaussian chain with the equilibrium spring root-mean-square length R_s, h^* is defined as $h^* = \sqrt{\frac{3}{\pi}}\frac{a_H}{R_s}$. Therefore, with a_H obtained numerically as discussed in Section II, we can vary h^* by varying R_s. We choose to study two values of h^*: 0.24, representing dominant HI; and 0.16, for moderate HI.

The SRD simulation parameters are chosen to be $\rho = 10, \Delta t = 0.1, \alpha = 150^\circ$ and we study the dynamics of Gaussian chains of monomer mass $\gamma = M/\rho m = 0.1, 0.2, 0.5, 1.0, 2.0, 5.0$. The MD time step Δt_{MD} is chosen to be 10^{-4} ($10^{-3}\Delta t$) and all the values above are in SRD units. Due to the heavier mass assigned to the polymer bead, one might expect that one could take Δt_{MD} to be at least as large as Δt. We checked in several cases that the results do in fact converge when we take $\Delta t_{\mathrm{MD}} = \Delta t$. (Here "convergence" means that the results agree within statistical error with results obtained for smaller Δt_{MD}.) Although convergence is achieved even for larger MD time steps, for extra assurance, we chose to use a very small value of $\Delta t_{\mathrm{MD}} = 10^{-4}$, since the MD integration is fast, and by far the slowest step of the simulation is the collision step, which occurs with time step Δt.

Figure 3.4 shows that diffusivities from SRD are in good agreement with those from the normal mode analysis at both $h^* = 0.24$ & $h^* = 0.16$. Bead inertia evidently has a very weak effect on the diffusivity.

To compare rotational relaxation times, we scale them with the Rouse values. The quantities $\tau_1, \eta, a_{\mathrm{H}}, k_{\mathrm{B}}T$ form a dimensionless group $\Pi = \tau_1/t_0$, with $t_0 = \eta a_{\mathrm{H}}^3/k_{\mathrm{B}}T$. The Rouse rotational relaxation time in these units is given by $\tau_{\mathrm{R}} = Ct_0$, where $C = \frac{3}{2}\left(h^* \sin\frac{\pi}{2N_{\mathrm{b}}}\right)^{-2}$.

Figure 3.5 plots τ_1 versus mass ratio γ. This shows:

1) at $h^* = 0.24$ (left figure), τ_1 from BD simulations deviates from analytical normal-mode (or Zimm) values in the direction of the Rouse values. This disagreement between BD and normal-mode results is likely explained by fluctuations in HI, which are neglected by the normal mode analysis, since the normal-mode analysis pre-averages the HI tensor over the polymer's conformations. It was shown in previous work that inclusion of HI fluctuations lowers τ_1 below the Zimm value for a dumbbell [Zylka and Öttinger (1989)].

2) τ_1 from SRD simulations at $h^* = 0.24$ also deviates from analytical Zimm values from the normal-mode analysis in the direction of the Rouse values, but reaches a minimum at $\gamma = 0.5$, where it agrees with that from BD simulations within statistical error. This trend can be understood by consideration of the inertial effect. In Section 3.3, we estimated L_M , the characteristic length of inertia for a polymer bead with a mass *M*; negligible inertia requires that $L_M / R_g \ll 1$. Since for fixed h^*, $R_g \propto a_H$, and as seen in Figure 3.2, both L_M and a_H increase with γ, we expect an optimum γ at which the inertial effect is minimized. As shown by circles in Figure 3.6, at around $\gamma = 0.5$, the ratio L_M / R_g reaches a minimum below 0.1, which is evidently small enough that inertia is negligible.

3) At $h^* = 0.16$, the squares in Figure 3.6 show that L_M / R_g is below that for $h^* = 0.24$. Under these conditions, as shown in Figure 3.5 (right), τ_1 from SRD and BD simulations agree well. Meanwhile HI fluctuations have less effect, so that τ_1 from BD simulations agree well with the analytical Zimm value. Nevertheless, τ_1 from SRD tends to be somewhat smaller than from BD.

It is difficult to trace the source of this small difference. It might result because the hydrodynamic near-field is not well resolved in either BD or SRD. In BD, the HI is described by a far-field Rotne-Prager tensor, and the expression in the Rotne-Prager tensor for small bead separation is not accurate. In SRD, during the collision step, two polymer beads have a probability to be sorted into the same cell and collide, and this distorts the hydrodynamic couplings between bead movements, limiting the accuracy of hydrodynamic near-field. Possibly some other inaccuracy in the SRD method might be responsible, however, and we did not pursue the source of this small discrepancy any further here.

The key finding of this sub-section is that for short Gaussian chains (10-spring), at moderate HI, since $L_M / R_g < 0.1$, the inertial effect is negligible; hence SRD results are in good agreement with those of BD. And at dominant HI, one can minimize the inertial effect by adjusting the mass ratio $\gamma = M / \rho m$ to minimize the ratio L_M / R_g.

3.4.2. Gaussian chains of different lengths at fixed mass ratio $M / \rho m = 1.0$

In this sub-section, we fix mass ratio $\gamma = M / \rho m$ at 1.0, and vary N_s, the number of springs, to determine the polymer dynamics at $h^* = 0.24$ & $h^* = 0.16$.

For the diffusivity *D*, we can see from Figure 3.7 that the results from SRD are in good agreement with those from the normal mode analysis at both $h^* = 0.24$ and $h^* = 0.16$.

For the rotational relaxation time τ_1: 1) At $h^* = 0.16$, the condition $L_M / R_g \ll 1$ holds, and hence, as shown in Figure 3.8 (right) good agreement is obtained between the results from SRD and the

corresponding results from an analytical normal mode analysis, and with those from BD simulations. 2) At $h^* = 0.24$, by increasing N_s, $L_M / R_g \ll 1$ can also be reached. We can see in Figure 3.8(left), for short chains ($N_s = 5$), that τ_1 from SRD deviates by 24% from the Zimm value and 19% from the BD value. As N_s increases, the SRD results converge to the BD results and finally agree within the statistical error. The simulation results from both BD and SRD deviate from the analytical Zimm values in the direction of Rouse due to the HI fluctuation.

From Figure 3.8 (right), we can also see that for all chain lengths ($N_b < 100$), with $h^* = 0.16$, τ_1 does not follow the expected power law with respect to N_s as shown by the disagreement between the solid line and the points. As h^* increases to approach the dominant HI limit, the analytical Zimm values get closer to the solid line as shown in Figure 3.8 (left). (For long Gaussian chains, $N_s \gg 1$, without HI, $\tau_R \propto N_s^{2.0}$, while in a theta solvent in the limit of dominant HI, $\tau_Z \propto N_s^{1.5}$. Therefore $\tau_Z / \tau_R \propto N_s^{-0.5}$ as given by the solid line shown in Figure 3.7.)

We now take a closer look at the results of τ_1 by scaling the simulation results with the analytical Zimm values as shown in Figure 3.9. We can see that as the coil size gets bigger, the BD results deviate more from the Zimm values, possibly because the HI fluctuations have more influence on the relaxation. On the other hand, for SRD simulations, as the coil size gets bigger, the inertial effect has less influence on the relaxation. As the inertial effect becomes negligible in SRD, there may be a crossover between the BD and SRD, though it is within the standard error. Note that due to the many-body correlation and inertia, the thermal fluctuations in SRD are actually "colored" noise, in contrast to the white-noise fluctuations in BD. When the HI

fluctuations have increased influence on the polymer dynamics, this crossover may indicate that different types of fluctuation in SRD and BD may result in somewhat different polymer dynamics.

Last but not the least, we vary the SRD simulation parameters $\Delta t, \rho, \alpha$, and check the resulting polymer dynamics for several cases. The results agree within the statistical error when the mass ratio γ is fixed, presumably suggesting that the inertial effect is controlled by the mass ratio rather than the polymer mass itself. This is reasonable because the efficiency of the momentum transfer from polymer to solvent ought to be determined by the mass ratio, not the mass alone. But to confirm this conclusion, more detailed study may be required, which is beyond the scope of this chapter.

The key finding of this sub-section is that at dominant HI, the inertial effect is negligible for chains with enough beads that the condition $L_M / R_g < 0.1$ is reached, and then SRD and BD simulations agree.

To summarize findings up to this section as a recap of parameters and results for SRD simulations of polymer chains. We choose a set of general SRD parameters $\rho = 10, \Delta t = 0.1, \alpha = 150^\circ$ for simulating the relaxation of polymer chains in the absence of flow. And we studied systematically the mass ratios $\gamma = M / \rho m = 0.1, 0.2, 0.5, 1.0, 2.0, 5.0$. For dominant HI represented by $h^* = 0.24$, and short chains (10-spring) SRD gave the best agreement with BD at $\gamma = 0.5$; when chains are with 20 or more springs, good agreement was obtained at any mass ratio. For moderate HI, represented by $h^* = 0.16$ in this paper, SRD agrees with BD at all mass ratios. We expect these parameters to be generally applicable not only for Gaussian chains, but

also when chains are finitely extensible and/or excluded volume interactions are present between beads.

3.4.3. Finitely extensible chains with excluded volume (EV)

Finally, we include finite extensibility by replacing the Hookean spring with a wormlike spring, which is frequently chosen to model DNA chains [Marko and Siggia (1995)]:

$$\mathbf{f}_{ij} = \frac{k_{\mathrm{B}}T}{2b_{\mathrm{K}}}\left[\left(1-\frac{R_{ij}}{L_{\mathrm{s}}}\right)^{-2} - \frac{1}{4} + \frac{R_{ij}}{L_{\mathrm{s}}}\right]\frac{\mathbf{R}_{ij}}{R_{ij}}\delta_{i,j\pm1} \tag{3.4.3.1}$$

where $\mathbf{f}_{ij}$ refers to the spring force on the *i*-th bead resulting from the *j*-th bead; $\mathbf{R}_{ij} = \mathbf{R}_j - \mathbf{R}_i$, $\mathbf{R}_i$ is the coordinate of the *i*-th bead; L_{s} is the maximum spring length, $L_{\mathrm{s}} = L_{\mathrm{DNA}}/N_{\mathrm{s}} = N_{\mathrm{K,s}}b_{\mathrm{K}}$, L_{DNA} is the contour length of the DNA chain, b_{K} the Kuhn length, and $N_{\mathrm{K,s}}$ the number of Kuhn segments per spring.

To model solvent quality, we include the following EV repulsive potential between pairs of polymer beads [Jendrejack *et al*. (2002)]:

$$U_{ij} = \frac{1}{2}vk_{\mathrm{B}}TN_{\mathrm{N,s}}^2\left(\frac{9}{2\pi R_{\mathrm{s}}^2}\right)^{2/3}\exp\left(-\frac{9R_{ij}^2}{2R_{\mathrm{s}}^2}\right) \tag{3.4.3.2}$$

where $R_{\mathrm{s}}^2 = N_{\mathrm{N,s}}b_{\mathrm{K}}^2$ is the mean-square end-to-end length of a spring, and *v* is the excluded volume parameter.

We wish to see whether our SRD simulations of a DNA chain can reproduce the experimental results as reviewed by Jendrejack *et al.* (2002). In Jendrejack *et al*. (2002), to model a YOYO-1 stained 21 μm λ-phage DNA in a 43.4 cP solvent (water viscosified with sucrose) at room

temperature 23C and reproduce the experimental results, the BD parameters: $\{L_{\mathrm{DNA}}, N_{\mathrm{s}}, b_{\mathrm{K}}, a_{\mathrm{H}}, v\}$ were set to the following values: {21 μm, 10, 0.106 μm, 0.077 μm, 0.0012 $\mu\mathrm{m}^3$}. To check whether these results can be reproduced using SRD simulations, we map these parameter values into SRD units, i.e. $\{\beta L_{\mathrm{DNA}}^{(\mathrm{BD})}, N_{\mathrm{s}}, \beta b_{\mathrm{K}}^{(\mathrm{BD})}, \beta a_{\mathrm{H}}^{(\mathrm{BD})}, \beta^3 v^{(\mathrm{BD})}\}$, where $\beta = a_{\mathrm{H}}^{(\mathrm{SRD})} / a_{\mathrm{H}}^{(\mathrm{BD})}$, and SRD (BD) stands for SRD (BD) simulations, respectively. The corresponding SRD values turn out to be {67.0, 10, 0.338, 0.246, 0.0390} in SRD units with $\rho = 10, \Delta t = 0.1, \alpha = 150^{\circ}, \gamma = 1$.

We first simulate a single DNA chain at equilibrium. The diffusivity from SRD simulations is $(1.16 \pm 0.02) \times 10^{-2}\ \mu\mathrm{m}^2/\mathrm{s}$, reproducing the experimental value $1.15 \times 10^{-2}\ \mu\mathrm{m}^2/\mathrm{s}$ [Jendrejack *et al*. (2002)]. Note EV is another non-linear effect that can mix higher order eigenmodes into the 1st normal mode, and here it dominates the HI. The values of τ_1/τ_{R} are 1.52 ± 0.03 from BD simulations and 1.49 ± 0.07 from SRD simulations; they agree within statistical error.

Next we compare the experimental longest relaxation time, τ, with that from the simulations. In the simulations, we have three ways to determine the longest relaxation time. The first method is to calculate it from the rotational relaxation time τ_1 via the relation $\tau = \tau_1/2$ [Doi and Edwards (1986)]. The second method is as described in Jendrejack *et al*. (2002), in which a stretched DNA chain is allowed to relax to equilibrium and τ is determined from a fit over the final 10% decay in the average chain stretch length squared $\langle X^2 \rangle$ to $\langle X^2 \rangle = A\exp(-t/\tau) + B$. Here *X*, the stretch of the DNA molecule, is defined as the distance between the upstream-most portion of the DNA and the downstream-most portion, i.e. $X = \max(\mathbf{R}_{i,x}) - \min(\mathbf{R}_{i,x})$, where $\mathbf{R}_i$ is the position of *i*-th bead, and the *x*-direction is the stretching direction. The third method is the same as the second, except that only the last 1% of the chain stretch squared is used. Since we focus here on

the dynamics near equilibrium, it does not matter much what the initial stretch of the DNA is or how we stretch the DNA. In our simulations, we stretch the DNA chain to 75% of its contour length, with beads separated evenly along a line. Because the trajectories are very noisy, we compute $\langle X^2 \rangle$ from an average over an ensemble of 1000 runs, where the standard error is estimated as described at the beginning of this Section.

To compare with the experimental data, we convert the results from the simulation into values in SI units. The comparison is given in Table 3.1.

From Table 3.1, we can see: 1) $\tau^{(1,3)}$ values from SRD simulations agree with those from BD simulations within statistical error. 2) For the BD and SRD simulations, $\tau^{(1)}$ is closer to $\tau^{(3)}$, but is significantly larger than $\tau^{(2)}$. This difference arises because even if the fitting to the relaxation of chain stretch only includes stretch that is 10% or less that of the contour length, there still is a significant contribution from the faster modes to the rate of relaxation. Also note, for the stretched DNA, the polymer beads are well separated, so that EV has less effect on the polymer dynamics for the stretched DNA than for the DNA chains at equilibrium, which also leads to faster relaxation. 3) The results from simulations show reasonable agreement with the experimental data. The inertia in SRD presumably slows the decay of the faster modes, resulting in relatively more contribution from faster modes left in the final 10% decay; therefore $\tau^{(2)}$ from SRD is smaller than that from BD. The experimental value is in between the SRD and BD values.

For completeness, we also compare the BD and SRD simulations with different γ at dominant HI ($h^* = 0.24$) for polymer chains with finite extensible spring and EV. To set $h^* = 0.24$, we hold the Kuhn length the same and reduce the number of Kuhn segments per spring. This corresponds to a DNA chain with a shorter contour length, but with more beads and hence more drag per unit

length. We keep the excluded volume parameter per bead the same. The results are shown in Figure 3.10. We can see the best agreement between BD and SRD tends to shift to $\gamma = 1.0$. Nevertheless, it is not significant, since the difference is almost within the statistical error. This is presumably due to the EV, because bead radius from EV is about 2-3 times of L_M , so that EV keeps the polymer beads separated by a distance greater than the distance L_M required for the inertia effect to die out. Therefore with EV, inertia has less effect on the polymer dynamics at $h^* = 0.24$ than that without EV.

The key finding of this sub-section is that SRD simulates DNA chains well. When computed from the relaxation of stretched DNA chains as experiments do, SRD gives a relaxation time in reasonable agreement with experiment. The discrepancy is presumably due to the effect of inertia and EV.

3.5. Conclusions and Perspective

We carefully explored the ability of stochastic rotational dynamics (SRD) to simulate accurately the self-diffusivity and the rotational relaxation time of polymer chains with Hookean and non-Hookean springs, by comparing SRD results to those from Brownian dynamics simulations and (for Hookean springs) to those from normal mode analyses. We obtained the longest relaxation time from the SRD and Brownian dynamics simulations using the auto-correlation function of the slowest normal mode.

In SRD, the polymer chains have finite mass. Hence, the diffusivity reaches its long-time steady value only after the inertial effect dies out. The slowest normal mode, beyond this transient period due to inertia, still does not decay by a single exponential due to the non-linear mode coupling induced by HI and additional excluded volume effects for DNA chains), and the

rotational relaxation time reaches its long-time steady value after the coupled faster modes die out.

The simulation results show that the inertia has a very weak effect on the diffusivity; therefore the diffusivity from SRD agrees with the analytical Zimm value from normal mode analysis very well. For the rotational relaxation time, the inertial effect is negligible when $L_M / R_g < 0.1$ (where L_M is the characteristic displacement distance over which inertia dies out for a polymer bead with a given mass *M*). This condition usually holds for moderate HI, represented by $h^* = 0.16$ in this paper, even for chains with only 10 springs, and hence the SRD results for the relaxation time agree well with results from a normal mode analysis, and from Brownian dynamics simulations. For dominant HI, represented by $h^* = 0.24$, for short chains ($N_s = 10$), the inertial effect can be minimized by adjusting the mass ratio $\gamma = M / \rho m$. When the mass ratio is fixed at a relative large value ($\gamma = 1$), $L_M / R_g < 0.1$ can be reached for long chains ($N_s \geq 20$), and then relaxation times from SRD and BD simulations agree, but are greater than those from a normal mode analysis. This deviation can be attributed to fluctuating hydrodynamic interactions, which is not included in the pre-averaged normal mode analysis.

Finally we applied the SRD method to simulate DNA using a wormlike-chain spring law and excluded volume. The SRD reproduces the experimental diffusivity, the relaxation time from the BD simulations ($h^* = 0.16$), and is in reasonable agreement with the experimental relaxation time.

In general, we find that the SRD model adequately captures hydrodynamic interactions and excluded volume interactions, and is therefore suitable for simulating polymer chains in confined, complex, geometries.

References

Bird, B. R., C. F. Curtiss, R. C. Armstrong and O. Hassager, *Dynamics of Polymeric Liquids.* 2nd Ed. (Wiley, New York, 1987), Vol. 2.

Doi, M. and S. F. Edwards. *The Theory of Polymer Dynamics* (Clarendon Press, Oxford . 1986).

Gompper, G., T. Ihle, D. M. Kroll and R. G. Winkler, "Multi-Particle Collision Dynamics: A Particle-Based Mesoscale Simulation Approach to the Hydrodynamics of Complex Fluids," *Advances in Polymer Science* **221**, 1-87 (2008).

Huang, C. C., A. Chatterji, G. Sutmann, G. Gompper and R. G. Winkle, "Cell-level canonical sampling by velocity scaling for multiparticle collision dynamics simulations," *Journal of Computational Physics* **229**, 168-177 (2010).

Ihle, T., E. Tüzel and D. M. Kroll, "Equilibrium calculation of transport coefficients for a fluid-particle model," *Physical Review E* **72**, 046707(11) (2005).

Jendrejack, R. M., J. J. de Pablo and M. D. Graham, "Stochastic simulations of DNA in flow: Dynamics and the effects of hydrodynamic interactions," *Journal of Chemical Phycics* **116**, 7752(8) (2002).

Kikuchi, N., C. M. Pooley, J. F. Ryder and J. M. Yeomans, "Transport coefficients of a mesoscopic fluid dynamics model," *Journal of Chemical Physics* **119**, 6388(12) (2003).

Larson, R. G., "The rheology of dilute solutions of flexible polymers: Progress and problems," *Journal of Rheology* **49**, 1-70 (2005).

Malevanets, A. and J.M. Yeomans, "Dynamics of short polymer chains in solution," *Europhysics Letters* **52**(2), 231-237 (2000).

Marko, J. F. and E. D. Siggia, "Stretching DNA," *Macromolecules* **28**, 8759-8770 (1995).

Ripoll, M., K. Mussawisade, R. G. Winkler and G. Gompper, "Low-Reynolds-number hydrodynamics of complex fluids by multi-particle-collision dynamics," *Europhysics Letters* **68**(1), 106-112 (2004).

Thurston, G. B., “Exact and approximate eigenvalues and intrinsic functions for Gaussian chain theory,” *Polymer* **15**, 569-572 (1974).

Watari, N., M. Makino, N. Kikuchi, R. G. Larson and M. Doi, “Simulation of DNA motion in a microchannel using stochastic rotation dynamics,” *Journal of Chemical Physics* **126**, 094902(7) (2007).

Zylka, W. and H. C. Öttinger, 'A comparison between simulations and various approximations for Hookean dumbbells with hydrodynamic interaction,' *Journal of Chemical Physics* **90**, 474-480 (1989).

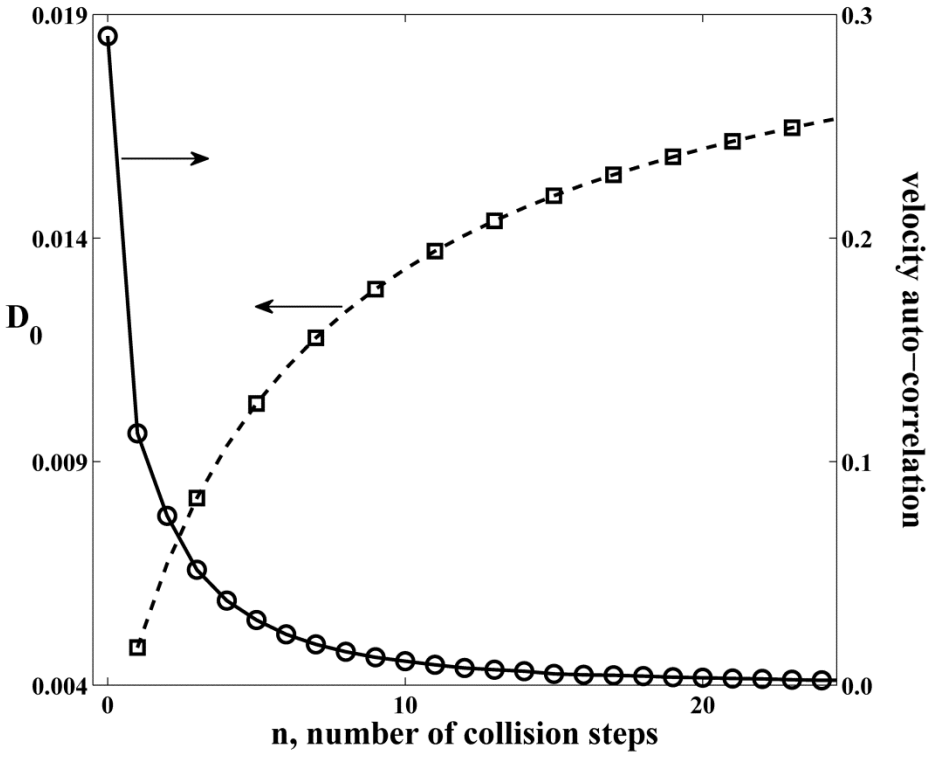

Figure 3.1: Velocity auto-correlation (circles and solid curve) and self-diffusivity D_0 (squares and dashed curve) of a single free monomer versus number of collisions. Squares: D_0 calculated from Eq. (3.3.2). Dashed curve: D_0 calculated from Eq. (3.3.3). Simulation parameters: $\rho = 10, \Delta t = 0.1, \alpha = 150^\circ, \gamma = M/\rho m = 1.$

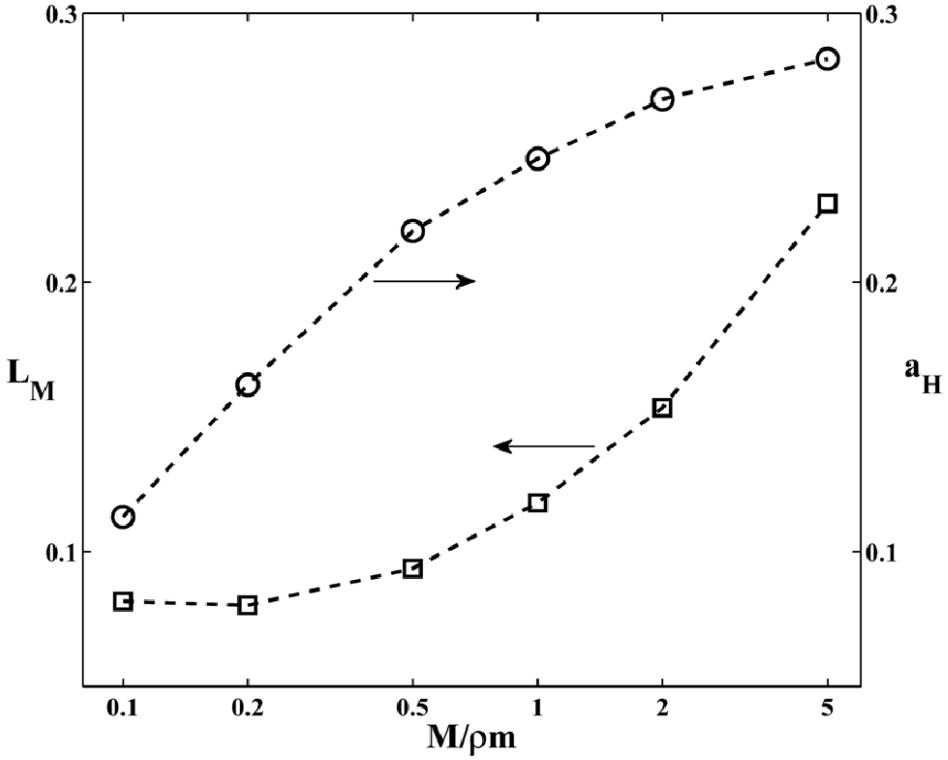

Figure 3.2: L_M (circles) and a_{H} (squares) versus mass ratio $\gamma = M/\rho m$ with simulation parameters $\rho = 10, \Delta t = 0.1, \alpha = 150^{\circ}$.

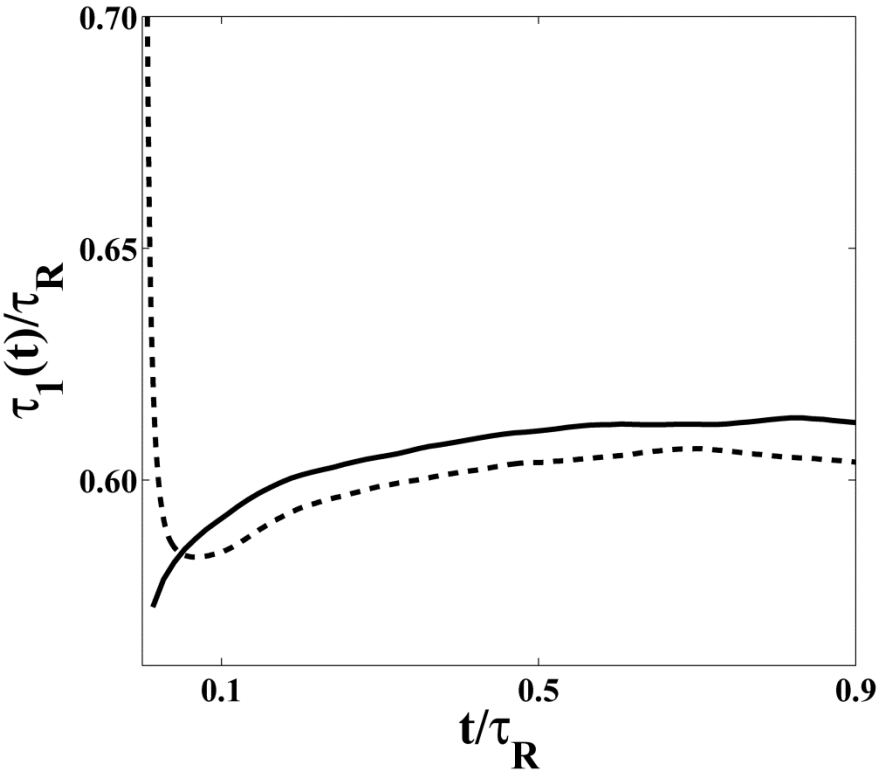

Figure 3.3: Instantaneous rotational relaxation time $\tau_1(t) = -t/\ln\left[n_1(t)\right]$ versus delay time *t* of a 20-spring Gaussian chain at $h^* = 0.24$. Solid curve is from BD simulations, dashed curve is from SRD simulations with simulation parameters $\rho = 10, \Delta t = 0.1, \alpha = 150^\circ, M = 10m$.

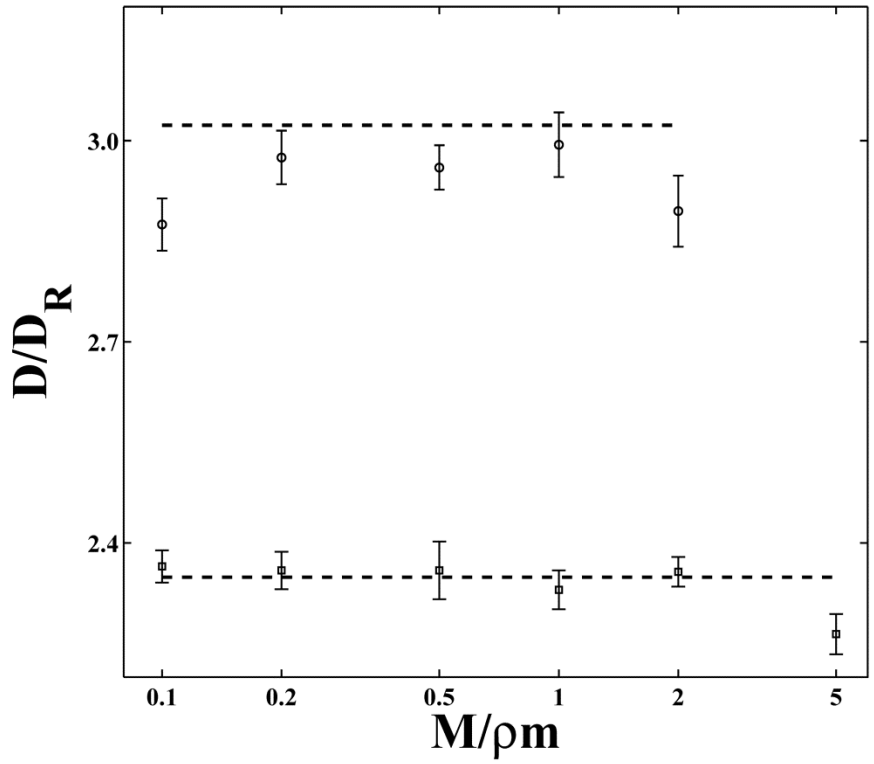

Figure 3.4: Diffusivity D versus mass ratio $\gamma = M/\rho m$ of a 10-spring Gaussian chain with simulation parameters $\rho = 10, \Delta t = 0.1, \alpha = 150^{\circ}$; upper (lower) dashed line is the Zimm normal mode value at h^* = 0.24(0.16), circles (squares) with error bars are the values from SRD simulations at h^* = 0.24(0.16).

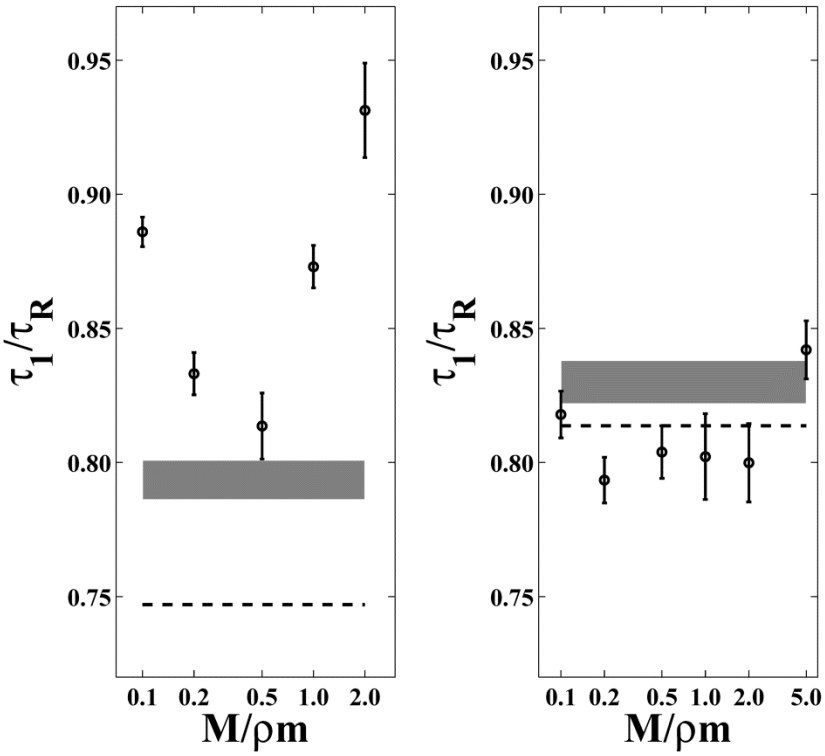

Figure 3.5: Rotational relaxation time τ_1 versus mass ratio $\gamma = M/\rho m$ of a 10-spring Gaussian chain with simulation parameters $\rho = 10, \Delta t = 0.1, \alpha = 150^{\circ}$; left (right) figure contains the results at h^* = 0.24(0.16); dashed lines are the Zimm values, the gray areas are the values from BD simulations bounded with its standard error; circles with error bars are the values from SRD simulations.

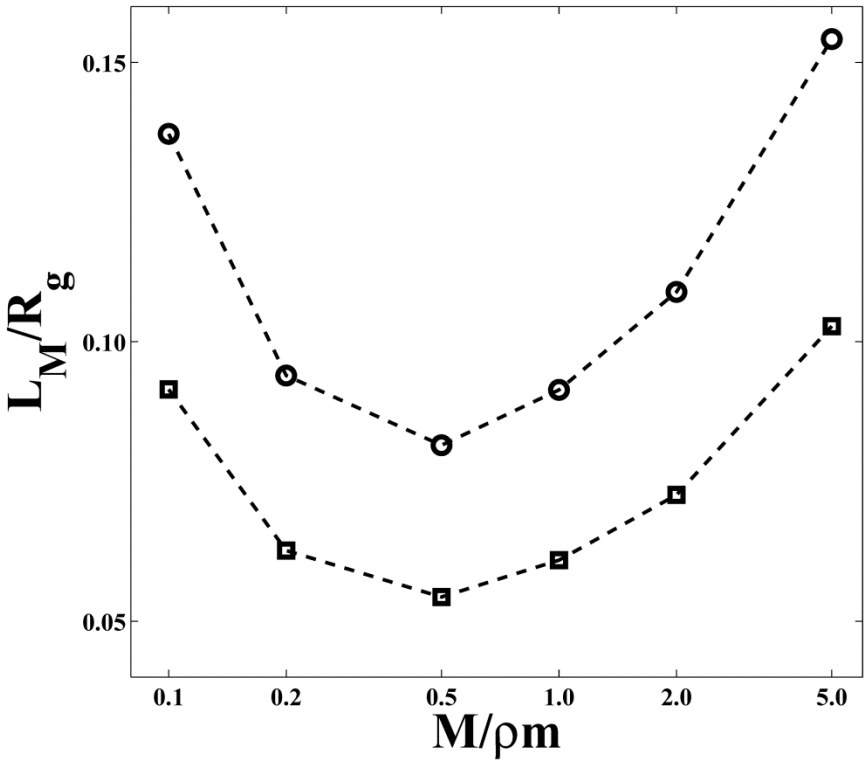

Figure 3.6: Ratio L_M/R_g versus mass ratio $\gamma = M/\rho m$ of a 10-spring Gaussian chain at h^* = 0.24 (circles) and h^* = 0.16 (squares) with simulation parameters $\rho = 10, \Delta t = 0.1, \alpha = 150^\circ$.

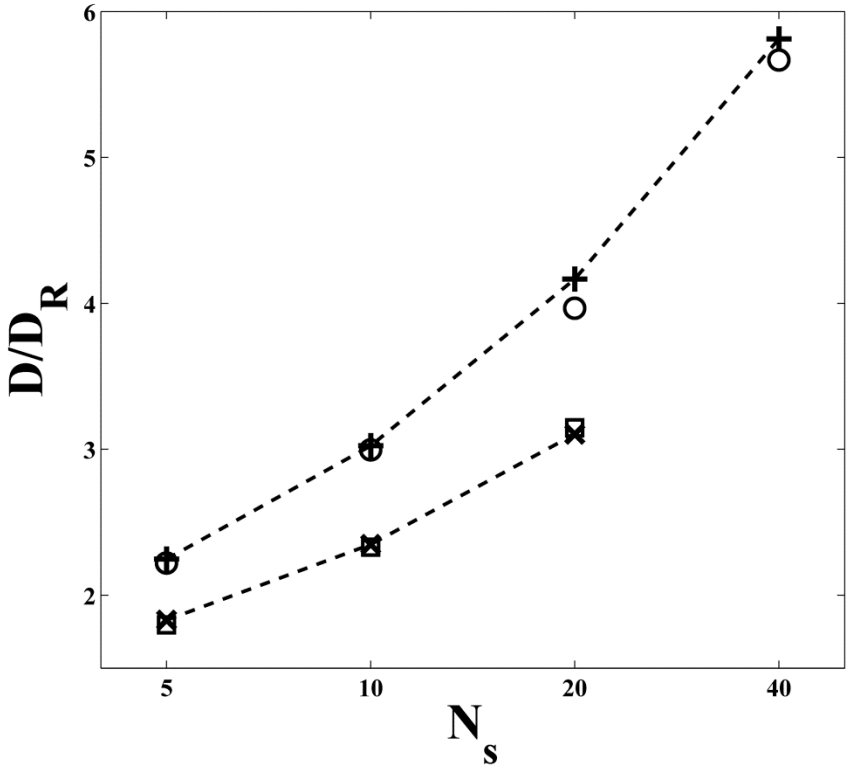

Figure 3.7: Diffusivity D of Gaussian chains versus number N_s of Hookean springs with simulation parameters $\rho = 10, \Delta t = 0.1, \alpha = 150^\circ$. Pluses (crosses) guided by the dashed curves are values from normal mode analysis at h^* = 0.24(0.16), circles (squares) are the values from SRD simulations at h^* = 0.24(0.16). The estimated statistical errors in the SRD and BD results are less than the size of the symbols.

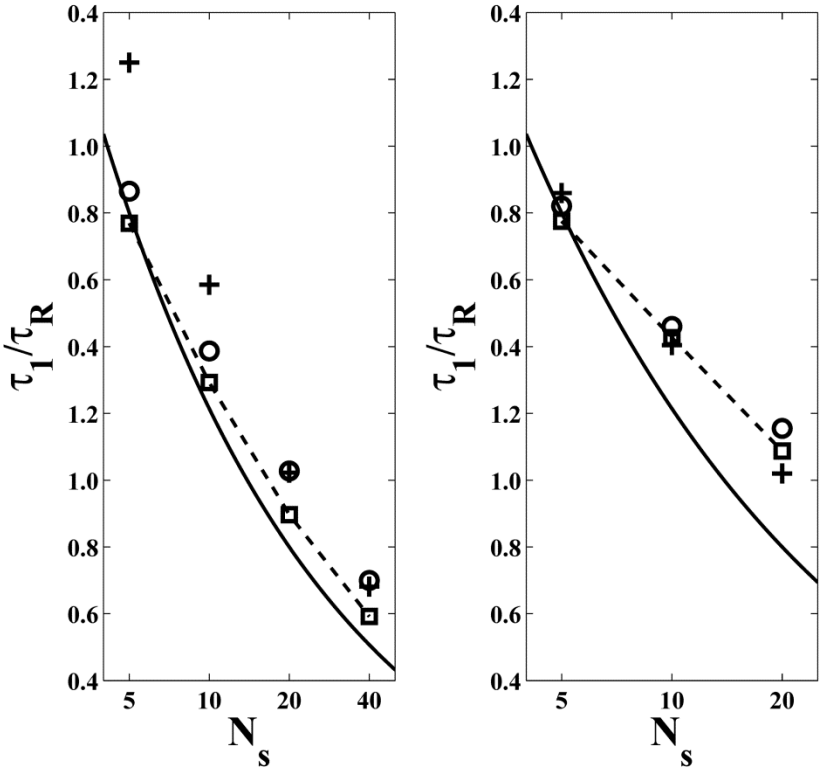

Figure 3.8: Rotational relaxation time of Gaussian chains at $h^* = 0.24$ (left) and $h^* = 0.16$ (right) as a function of the number N_s of Hookean springs. Squares & dashed line: analytical Zimm values normalized by analytical Rouse values, both of which are from normal mode analysis; solid line: $f(N_s) \propto N_s^{-0.5}$ which is the power law of τ_Z/τ_R for the dominant HI limit. Circles: values from BD simulations; pluses: values from SRD simulations. The estimated statistical errors in the SRD and BD results are less than the size of the symbols.

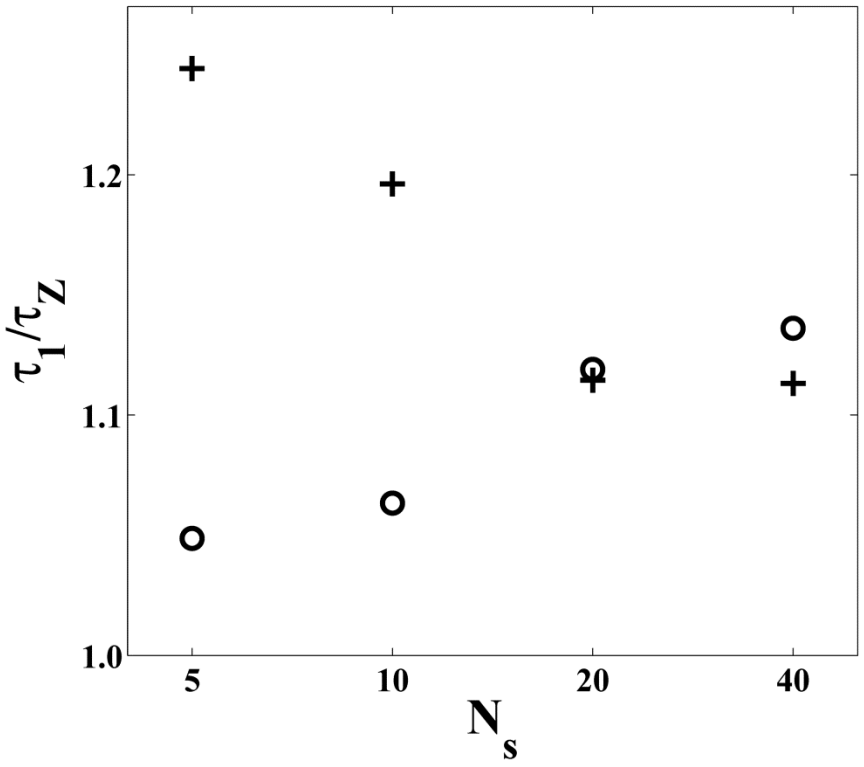

Figure 3.9: Rotational relaxation time of Gaussian chains at $h^* = 0.24$ as a function of the number N_s of Hookean springs. Circles: values from BD simulations; pluses: values from SRD simulations. The values are normalized by analytical Zimm values from normal mode analysis.

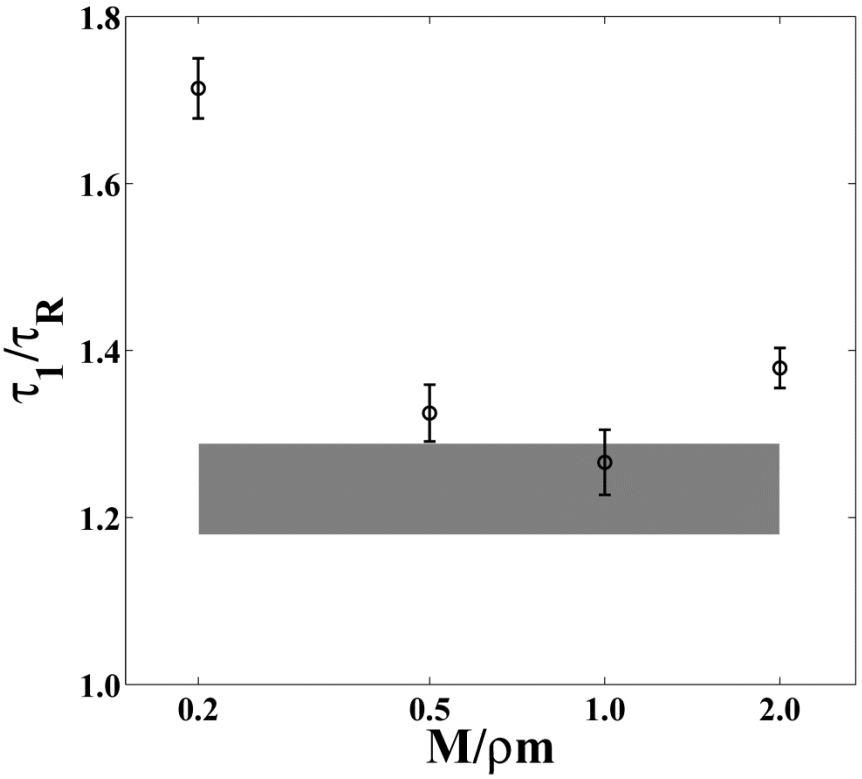

Figure 3.10: Rotational relaxation time τ_1 versus mass ratio $\gamma = M/\rho m$ of a "modified" DNA chain with h^* = 0.24 and simulation parametersc; the gray areas are the values from BD simulations bounded with its standard error; circles with error bars are the values from SRD simulations

Table 3.1: Comparison of estimates of longest relaxation time, τ (in sec)

	Experiment	BD	SRD
$\tau^{(1)}$		10.7 ± 0.2	10.5 ± 0.9
$\tau^{(2)}$	4.1	4.5 ± 0.0	3.5 ± 0.0
$\tau^{(3)}$		7.7 ± 0.3	7.7 ± 0.5

1. $\tau^{(1)}$ from half the rotational relaxation time.
2. $\tau^{(2)}$ from a fit to the last 10% decay of $\left\langle X^2 \right\rangle / L_{\mathbf{DNA}}^2$.
3. $\tau^{(3)}$ from a fit to the last 1% decay of $\left\langle X^2 \right\rangle / L_{\mathbf{DNA}}^2$.

Chapter 4

Single Polymer Chain Dynamics in a Microfluidic Contraction Flow

In this chapter, we study polymer migration in a periodic pressure-driven sudden contraction-expansion flow with contraction dimension comparable to the polymer radius of gyration. We use both Stochastic Rotation Dynamics (SRD), which includes hydrodynamic interaction (HI), and simple Brownian dynamics (BD), with HI omitted and flow field given by finite element analysis. The similarity in results from SRD and BD at low Weissenberg number Wi (<10, where Wi is based on the shear rate in the narrow region of the contraction channel) shows that HI has only a weak effect on polymer migration, and inexpensive BD simulations without HI are adequate to predict the migration accurately at low Wi (<10). After it is deformed during its passage through the narrow region, the polymer migrates towards the center streamline in the wide region. This migration is induced by polymer stretching along curved streamlines, with migration velocity proportional to the square of the Weissenberg number Wi^2. This migration affects the residence time distribution for a polymer to pass through the contraction channel periodically, and using the central limit theorem, we can accurately predict the position and width of a band of polymer passing through *N* periodic contractions. We thereby demonstrate the potential for polymer length-dependent migration as a mechanism of size separation in a multi-step planar contraction channel. We find that the best separation is achieved at Wi around 2, where the streamline-curvature-induced migration has the greatest resolving power between polymers of different size. We find a separate mechanism at low Wi less than unity, where the

chains with large radius of gyration are delayed in their entry to the thin channel, relative to shorter polymers. This "blockage" separation mechanism differs from that of size-exclusion chromatography, and yields faster migration by the shorter chains. Our strategy of combining simulation methods with the central limit theorem could also be used to predict separation efficiencies of a wide variety of polymers and colloids in microfluidic geometries.

4.1. Introduction

Owing to recent advances in micro-fabrication technology, microfluidic devices can be fabricated inexpensively and reliably with tailored complex geometries. These devices commonly rely on pressure-driven or electrokinetically-driven flows to stretch polymer chains far from equilibrium. Such geometries provide a powerful platform to study non-equilibrium polymer dynamics, polymer-solvent interactions, and macromolecular transport phenomena. A comprehensive understanding of polymer dynamics in micro-fluidic devices is important for many potential applications, including polymer or DNA separation.

The most conventional and widely used polymer separation technique is size-exclusion chromatography (SEC), which was first developed in 1955 by Lathe and Ruthven (1956) . A typical SEC method is gel permeation chromatography (GPC), which can be traced back to Moore (1964). GPC techniques separate based on polymer size or radius of gyration. The flow rates in GPC columns are typically too small to deform the polymer molecules; that is the Weissenberg number Wi, which is the characteristic shear rate multiplied by the polymer relaxation time, is usually very small, much less than unity ($< 10^{-2}$) [Moore(1964)].

Meanwhile, techniques for separating biological molecules of different sizes have been developed in parallel with the evolution of molecular biology. Decades ago, Dill and Zimm

[Dill(1979), Dill and Zimm(1979)] proposed a rheological separation method for DNA molecules based on the radial migration of the DNA that occurs when DNA solutions are subjected to flow between rotating concentric cylinders or cones.

In this paper, we study polymer migration and separation in a multi-step planar contraction channel using two mesoscopic simulation methods. The first method is Stochastic Rotation Dynamics (SRD), which is a particle-based method of solving for polymer and fluid dynamics simultaneously, including the effects of hydrodynamic interaction (HI) within individual chains, between different chains, and between chains and the walls of the geometry. The SRD method is briefly described below in Section 4.2. The second method is Brownian dynamics (BD), in which we use the flow field in the absence of polymer, drawn either from a finite element solution or from SRD, as the convection term in a Langevin differential equation that, as used here, neglects all hydrodynamic interactions and also neglects the modification in the flow field produced indirectly by the polymer molecules through the momentum balance equation. In Section 4.3, by comparing results from SRD with those from Brownian dynamics (BD) for a single polymer chain without HI, we show that HI has only a weak effect on the polymer dynamics, and that BD simulations without HI predict the polymer migration accurately. We investigate in Section 4.4 the migration mechanism, which determines the spatial distribution and residence time distribution of the polymer, and show that the polymer migration toward the center of the channel observed in both SRD and BD simulations is due to the curvature of the contraction flow streamlines. Finally, in Section 4.5, using the central limit theorem, we demonstrate the potential of such flows for producing polymer separation using curvature-induced migration, which is a different mechanism for separation than the common size-

exclusion mechanism typical in flowing polymer solutions through columns with complex geometries. We summarize our results in Section 4.6.

4.2.Migration of a single polymer chain with HI, simulated using SRD

In this section, we investigate migration of single polymer chains with HI using Stochastic Rotation Dynamics (SRD). SRD is an especially promising method for situations in which fluctuating or time-dependent HI is potentially important, but the geometry is so complex that Brownian dynamics with full HI is difficult to implement. Earlier studies [Ripoll *et al*. (2004), Jiang *et al*. (2013)] have shown that SRD can accurately capture HI in the relaxation dynamics of an isolated chain in the absence of flow. Studies[Watari *et al*. (2007), Cannavacciuolo *et al*. (2008)] have also shown that SRD captures the HI between the solid boundaries and the polymer in shearing flows. In principle it should also capture the influence of polymeric stresses on the flow field.

4.2.1. Algorithm, geometry and boundary condition

In SRD simulations, the fluid is modeled by N solvent beads. The polymer is, as usual, modeled as a chain of N_b polymer beads connected by $N_\mathrm{s} = N_\mathrm{b} - 1$ springs. The algorithm consists of two steps: a *streaming* step followed by a *collision* step after a discrete time step Δt, which is referred as the collision time. In the *streaming* step, the solvent/polymer beads simply follow Newton's law, with the positions $\mathbf{r}_i$ and velocities $\mathbf{v}_i$ determined by integration using the velocity Verlet algorithm:

$$\mathbf{r}_i(t+\Delta t) = \mathbf{r}_i(t) + \mathbf{v}_i(t)\Delta t + \frac{1}{2}\frac{\mathbf{f}_i(t)}{m}\Delta t^2 \qquad (4.2.1.1)$$

$$\mathbf{v}_i(t+\Delta t) = \mathbf{v}_i(t) + \frac{1}{2}\frac{\mathbf{f}_i(t)+\mathbf{f}_i(t+\Delta t)}{m}\Delta t \qquad (4.2.1.2)$$

where $\mathbf{f}_i$ is the force exerted on the *i*-th bead and *m* is the bead mass. The masses of the solvent and polymer beads are not the same, and the mass ratio is chosen to optimize transport of momentum from the polymer to the solvent so that hydrodynamic interactions are most accurately captured [Jiang *et al*. (2013)]. Usually the polymer beads are more massive than the solvent beads, so that the integration time step for the polymer beads can be the same as Δt without losing accuracy at the relatively low shear rate applied in SRD simulations in this paper. In the *collision* step, the solvent/polymer beads are sorted into the cells of a *d*-dimensional cubic lattice (where typically $d = 3$) with lattice spacing *a*. The beads exchange momentum following a "collision" rule in which their velocities are updated after the collision as follows:

$$\mathbf{v}_i\left(t^+\right) = \mathbf{v}_{\mathrm{CoM},i}\left(t^-\right) + \mathcal{R}(\alpha)\left[\mathbf{v}_i\left(t^-\right) - \mathbf{v}_{\mathrm{CoM},i}\left(t^-\right)\right] \tag{4.2.1.3}$$

where $\mathcal{R}(\alpha)$ is a stochastic rotation matrix which rotates the velocity vector in a random direction through an angle α, $t^{+/-}$ refers to the time after/before the collision and $\mathbf{v}_{\mathrm{CoM},i}$ is the center of mass velocity of all beads in the collision cell where the *i*-th bead is located. This collision rule ensures that the kinetic energy and linear momentum in the cell are conserved during the collision. Therefore in SRD the flow field is discretized with a resolution determined by the cell size *a*. After each *collision* step, a thermostat is applied to adjust the local temperature of each collision cell to the imposed temperature [Watari *et al*. (2007), Huang *et al*. (2010)]. To guarantee Galilean invariance over long runs, a random shift of particles before executing the *collision* step has to be performed, and after the *collision* step, the particles are shifted back to their original positions [Ihle and Kroll (2001)].

The geometry of a planar contraction channel in our simulation is shown in Figure 4.1. The simulation box has dimensions $L_1 \times L_2 \times L_3$, where L_3 is the out-of-plane dimension, not shown in Figure 4.1 The lower and upper wide chambers are connected by a narrow channel with width *w* and length *h*. A constant acceleration ***g*** is applied along the *y* direction to drive the flow.

Along the *y* and *z* directions, we apply periodic boundary conditions; thus the geometry between the dashed lines shown in Figure 4.1 is extended infinitely along those directions. Therefore we are actually simulating a multi-step contraction channel. The flow field is invariant along the *z*-direction and thus 2-dimensional, although in SRD we solve the problem in three dimensions to allow isotropic random velocity fluctuations from Brownian motion. Along the walls, we apply a no-slip boundary condition. To realize the no-slip boundary condition, in the *streaming* step the bounce-back rule is applied. That is, if a bead intersects the boundary at time $t + \Delta t'$ during a Verlet time step Δt, the bead velocity at $t + \Delta t'$ is completely reversed, i.e. $\mathbf{v}(t + \Delta t') \to -\mathbf{v}(t + \Delta t')$, and in the remainder of the Verlet time step, the bead is propagated from the point of contact with the boundary using this new velocity [Whitmer and Luijten (2010)]. For simplicity, we replace $\Delta t'$ with its average value $\frac{\Delta t}{2}$, so that at the end of *streaming* step after the bounce-back, the bead is restored to its original position at the beginning of the *streaming* step, and the velocity is updated as:

$$\mathbf{v}_i(t + \Delta t) = -\mathbf{v}_i(t) + \frac{1}{4}\frac{\mathbf{f}_i(t) - \mathbf{f}_i(t + \Delta t)}{m}\Delta t \qquad (4.2.1.4)$$

However since a pure bounce-back rule fails to guarantee no-slip boundary conditions, further treatment is needed in the *collision* step. If *n*, the number of solvent beads shifted into a wall cell (which are the cubes on the edges of the geometry shown in Figure 4.1) after the random shift is

less than ρ, the average number of the solvent beads per cell, then $\rho - n$ "phantom" beads with velocities drawn from a Maxwell-Boltzmann distribution of zero average velocity and temperature T are added to that wall cell to participate in the collision for momentum exchange [Lamura *et al*. (2001)]. After this collision, these "phantom" beads are destroyed. New ones created with new random velocities whenever they are needed for collisions in the wall cells.

4.2.2. Simulation parameters and results

We set the dimensions of the simulation box to be L_1=21, L_2=18, L_3=20 and the narrow part of the channel is given dimensions of w=3, h=6. Taking into account the contribution from the wall cells, the contraction ratio is (21+1)/(3+1) = 5.5. For the SRD simulation, the parameters are chosen as following: the average number of solvent beads per cell is ρ = 5, the collision time is Δt = 0.05 and the rotation angle is $\alpha = 150°$. The mass of the polymer bead is set to be M = 2.5 to minimize the inertial effect on hydrodynamic interaction [Jiang *et al*. (2013)]. All these values are typical ones for SRD, chosen to optimize accuracy and computational speed [Gompper *et al*. (2008)]. The above values are in SRD units chosen so that the cell size is a = 1, the mass of the solvent bead is m = 1 and $k_B T$ = 1. In these units, the imposed acceleration is g = 0.02, chosen so that the polymers are well stretched under the flow, while the SRD fluid is not badly compressed (at most around 10%).

To model DNA polymer chains, we use the wormlike spring law [Marko and Siggia (1995)]:

$$\mathbf{f}_{ij} = \frac{k_{\mathbf{B}}T}{2b_{\mathbf{K}}}\left[\left(1-\frac{R_{ij}}{L_{\mathbf{s}}}\right)^{-2} - \frac{1}{4} + \frac{R_{ij}}{L_{\mathbf{s}}}\right]\frac{\mathbf{R}_{ij}}{R_{ij}}\delta_{i,j\pm1} \qquad (4.2.2.1)$$

where $\mathbf{f}_{ij}$ refers to the spring force on the *i*-th bead resulting from the *j*-th bead; $\mathbf{R}_{ij} = \mathbf{R}_j - \mathbf{R}_i$, $\mathbf{R}_i$ is the coordinate of the *i*-th bead; L_s is the maximum spring length, $L_s = L_{DNA}/N_s = N_{K,s} b_K$, L_{DNA} is the contour length of the DNA chain, b_K the Kuhn length, and $N_{K,s}$ the number of Kuhn segments per spring. We obtain specific values for these parameters by mapping the values from the BD bead-spring model of Jendrejack *et al.* (2002) into SRD units, as discussed in Jiang *et al.* (2013), yielding $\{b_K, L_s\}$ to be {0.380, 7.534} in SRD units, corresponding to {0.106μm, 2.1μm} in Jendrejack et al. The length of the chain is chosen such that its radius of gyration is comparable to *w*, the width of the narrow channel.

To characterize the migration of a single polymer chain in the contraction channel, we compute its residence time distribution (RTD), i.e. the distribution of time a polymer chain takes to pass through one periodic image of the geometry defined as the region between the dashed lines shown in Figure 4.1. While a single chain can pass multiple times through the channel because of the periodic boundary condition, it would nevertheless require a long computational time to collect statistics on the RTD for a single chain. For SRD, a single-chain calculation is computationally very inefficient, since most of the simulation time is spent on simulating the fluid beads. Thus, we simulate multiple chains distributed throughout the fluid, but keep the number of chains low enough that their influence on each other is negligible and the RTD becomes insensitive to chain concentration, which then corresponds to the dilute limit. Of course, this is the procedure followed in most experiments; i.e., a dilute solution rather than an isolated chain is used to obtain good chain statistics.

We are also interested in the spatial distribution of the polymer's center-of-mass. To calculate this, since the planar contraction flow is symmetric along the *z*-direction, we grid the contraction

channel in the *x*-*y* plane into cells of size *b*. (For simplicity, *b* is set to 1, the same as *a*, the size of the cubic collision cell by default.) The cells are indexed as (l_1,l_2), which are integers given by $(l_1,l_2) = (x,y)/b$, and (x,y) is position of the lower left corner of the cell. From the simulation, we can calculate $\mathrm{P}(l_1,l_2)$, the probability that the polymer's center-of-mass is located in cell (l_1,l_2). So the spatial probability density (or concentration) at coordinate $(l_1+0.5, l_2+0.5)\times b$ is given by $\mathrm{P}(l_1,l_2)/b^2$. In this paper, we typically consider distribution functions averaged over the wide region, or "chamber" of the contraction channel. The one-dimensional spatial distribution along *x* and averaged over y in the wide chamber is then defined by $f_X(x)|_{\text{chamber}} = \sum_{l_2 \in \text{chamber}} \mathrm{P}(l_1,l_2)/b^2,\ x=(l_1+0.5)b$, while the spatial distribution along *y* (averaged over x) in the chamber is $f_Y(y)|_{\text{chamber}} = \sum_{l_1} \mathrm{P}(l_1,l_2)/b^2,\ y=(l_2+0.5)b\,|_{l_2 \in \text{chamber}}$.

We normalize the residence time of an individual polymer molecule with μ_{f}, the mean residence time of a fluid element, that is with $\mu_{\mathrm{f}} = A/Q$, where *A* is the channel area (including wide and narrow regions) in the *x*-*y* plane, and *Q* is the volumetric flow rate per unit depth of the channel. We denote this normalized polymer residence time as τ. Figure 4.2 shows the RTD of this normalized time for a 10-spring chain with radius of gyration $R_{\mathrm{g}} = 2.1$. Note that the distribution obtained by simulating 75 chains simultaneously agrees with the cruder distribution obtained from simulating 5 chains simultaneously. Their mean and standard deviations agree to within the statistical error. The spatial distributions of polymer in these two simulations also superimpose to within error. The only difference is that with more chains, the viscosity of the solvent is increased, which results in slower polymer migration, but that is canceled out by the larger μ_{f}, which normalizes the values of τ.

4.3.Migration of single chain without HI, simulated by BD

To investigate the effect of hydrodynamic interaction (HI), we compare results from SRD to those from Brownian dynamics (BD) simulations that neglect HI. The discretized Langevin equation for the BD chain simulation is as following,

$$\mathbf{r}_i(t+\Delta t) = \mathbf{r}_i(t) + \mathbf{v}_i(t)\Delta t + \frac{\Delta t}{\zeta}(\mathbf{F}^{\mathrm{sp}} + \mathbf{F}^{\mathrm{B}}) \tag{4.3.1}$$

where $\mathbf{r}_i$ is the position of the i-th polymer bead, and $\mathbf{F}^{\mathrm{sp}}$ is the spring force. $\mathbf{F}^{\mathrm{B}} = \left(\frac{6k_{\mathrm{B}}T\zeta}{\Delta t}\right)^{1/2}$ sis the Brownian force, where $\mathbf{n}$ is a random three-dimensional vector each component of which has a magnitude uniformly distributed in the interval $[-1,1]$. The thermal energy $k_{\mathrm{B}}T$, and polymer bead friction coefficient ζ are set to be the same as in SRD. We grid the contraction channel in the x-y plane in the way described in Section 4.2.2, with cell size a. $\mathbf{v}_i(t)$ is the velocity of the i-th polymer bead at time t. If the bead is located in the cell with index (l_1,l_2) in the x-y plane at time t, then $\mathbf{v}_i(t) = \mathbf{v}(l_1,l_2)$, where $\mathbf{v}(l_1,l_2)$ is the solvent velocity at cell (l_1,l_2). For the boundary condition, we apply the bounce-back rule as described in Section 4.2.2.

4.3.1. Effect of hydrodynamic interaction

To determine the effect of HI on the dynamics, we set a=1 and use in BD simulations the solvent velocity obtained from the SRD simulation of pure solvent. Note that the parameters used in Jendrejack *et al.* (2002) correspond to a chain with moderate HI, $h^* = 0.16$. Here we also consider a chain with dominant HI, achieved by using shorter springs, but with the same R_{g}, obtained by increasing the number of beads per chain. Thus, to model dominant HI, we set $h^* = 0.27$ by holding the Kuhn length fixed and reducing the number of Kuhn segments per spring, i.e., by

decreasing L_s, the fully extended spring length. With the shorter spring, the number of beads is set to 29 so that R_g is kept the same.

Figure 4.3 (left) shows that for h^* =0.16, the RTDs from the SRD and BD simulations almost superimpose and so do the spatial distributions of the polymer's center of mass along x in the wide chamber in Figure 4.4 (left). This indicates that HI has negligible effect on the polymer dynamics at moderate HI. For dominant HI, the chain slightly concentrates more around the centerline than the chain without HI as shown in Figure 4.4 (right). This might be due to HI-induced migration [Jendrejack *et al*. (2004)], but, if so, the effect is weak. Meanwhile the RTD has a thinner tail with HI than without it as shown in Figure 4.3 (right). The main difference is that there is a somewhat larger accumulation of polymer near the entrance to the narrow channel (corresponding to y=12) in the BD simulations than that in the SRD simulations as shown in Figure 4.5. We will discuss this difference in Section 4.3.2. Table 4.1 shows that the mean and standard deviations of the RTD's from SRD and BD simulations agree well for moderate HI with h^* =0.16, and show a slight difference for dominant HI with h^* =0.27. Overall, HI has only a weak effect on the RTD even for strong HI, and for moderate HI, the SRD simulation is reproduced almost perfectly by the BD simulation with no HI.

4.3.2. Errors caused by the inaccuracy of the SRD flow field

The flow field from SRD is not as accurate as that from the finite element method (FEM), because an SRD fluid is somewhat compressible [Malevanets and Kapral (1999)], causing the solvent density in the contraction channel to be somewhat non-uniform (by about 10% at the entrance of the narrow channel where the SRD fluid is most compressed) and thus modestly distorting the flow field. Due to this compressibility, the solvent density in SRD rises above the average density at the upstream side of the narrow channel. Thus the SRD fluid gradually slows

down on average as it moves towards the entrance of the narrow channel because of the mass balance.

In addition, the resolution of the flow field in SRD is determined by the collision cell size a. With a=1 in SRD, at each value of y there are only 3 positions across the narrow channel at which the flow field can be evaluated, and this crude discretization in SRD will also cause inaccuracy in the flow field.

To determine how such errors from the inaccuracy of the flow field in SRD affect the polymer migration, we obtain the solvent velocity from finite element simulations and use these, rather than the SRD velocities, in the BD simulations and then compare the results with those obtained by using the SRD flow field in the BD simulations. In addition, using the flow field from FEM, we can grid the channel more finely by using a value of a less than 1 to see how the discretization of the flow field affects the results.

Another issue with SRD simulations is that the flow field does not extrapolate to zero at the boundary but rather half way into the wall cells, into which the polymer can not penetrate. Thus the boundaries for polymer beads and for the fluid do not precisely match, and the polymers see a slightly narrower contraction channel than the fluid does. To determine the error arising from this, in our BD simulations we modify the boundary for the polymer beads and let them bounce back at the boundary where the flow field drops to zero and compare the results to those from the previous simulations.

Overall, the results show that there are only slight discrepancies among all the discussed simulations above. Table 4.2 shows that the mean and standard deviation of the RTD's from SRD at moderate HI (h^*=0.16) and from BD simulations with different approximations to the

flow field for 10-spring chains agree well. The standard deviation in the last row in Table 4.2 deviates most from that in SRD, implying the main error is from the mismatch of the boundaries for the polymer beads and for the flow field. Nevertheless, as shown in Figure 4.6 and 4.7, the RTD and spatial distribution from the BD simulations with the modified boundary almost overlap with those from SRD simulations. And we can see in Figure 4.7 (bottom) that with the most accurate flow field from FEM, the discrepancy shown in Figure 4.5 in spatial distributions along y near the entrance (y = 12) to the narrow channel is almost eliminated. BD simulations with the flow field taken from FEM simulations with a resolution of a=0.2 reproduce both the RTD and the spatial distribution obtained using a lower FEM resolution, a=1. This implies that three points adequately sample the flow profile across the narrow channel, at least for the purpose of determining the RTD and the spatial distribution of polymer in the chamber.

In summary, HI has only a weak effect on the RTD and the spatial distribution. BD simulations without HI with an accurate flow field from FEM are adequate to predict polymer migration. The main error comes from the boundary for the polymer beads in SRD not matching that for the flow field, whereas in the BD simulations we can modify the boundary for the polymer beads to correct this error. In the rest of this paper, we will derive all results from BD simulations without HI and with the accurate flow field with resolution a=0.2 from FEM simulations, using the modified boundary for the polymer beads.

4.4.The mean μ and standard deviation σ of the residence time

We are particularly interested in the mean μ and standard deviation σ of the residence time distribution, since these quantities control the separation efficiency of polymer chains of different length, as we will see.

4.4.1. Polymer migration due to curvature of the streamlines

In a straight micro-channel, extensive studies [Watari *et al*.(2007), Cannavacciuolo *et al*.(2008), Jendrejack *et al*.(2004), Usta *et al*.(2005), Hernández-Ortiz *et al*.(2007), Hernández-Ortiz *et al*.(2008)], using different mesoscopic simulations, including SRD, show that HI between polymer and the wall causes the chains to migrate slowly towards the channel centerline. Ma and Graham (2005) developed a continuum theory for bead-spring dumbbell models in dilute polymer solutions near solid surfaces, giving the flux **j** of polymer chains as,

$$\mathbf{j} = c\mathbf{v}_\infty + \frac{c}{8}\langle \mathbf{qq} \rangle : \nabla\nabla \mathbf{v}_\infty + \boldsymbol{\mathcal{M}} : \boldsymbol{\tau}^{\mathrm{p}} - \nabla \bullet \left(c\mathbf{D}_{K,\mathrm{bulk}} \right) \tag{4.4.1.1}$$

where c is the polymer number density, $\mathbf{v}_\infty$ is the bulk fluid velocity field, **q** is the dumbbell end-to-end vector, $\boldsymbol{\mathcal{M}}$ is a third order tensor [Ma and Graham (2005)], $\boldsymbol{\tau}^{\mathrm{p}}$ is the polymer stress tensor and $\mathbf{D}_{K,\mathrm{bulk}}$ is the Kirkwood diffusivity tensor evaluated in an unbounded domain. Biased migration towards the centerline of a straight channel due to the HI between the polymer and wall arises from the third term in Eq. (4.4.1.1). This migration becomes significant at a Weissenberg number (Wi) of the order of 10 [Cannavacciuolo *et al*.(2008), Jendrejack *et al*.(2004), Usta *et al*.(2005)]. However in our contraction geometry, apparently HI is not the dominant mechanism for migration since the chain without HI also migrates towards the center as shown in Figure 4.4 (left). Moreover this migration, in either BD or SRD simulations occurs even though Wi is only 2.5 in the narrow channel and an order of magnitude smaller than this in the wide chamber. In this chapter, Wi is always based on the shear rate in the narrow channel, unless otherwise specified.

The last term in Eq. (4.4.1.1) is simply diffusive transport, which carries mass down a concentration gradient and cannot produce a spatial inhomogeneity in polymer concentration and the first term on the right side is convection, which also is unable to produce concentration inhomogeneities. Thus, the spatial inhomogeneities we observe are predominantly due to the second-order gradient term, which is the second term on the right side of Eq. (4.4.1.1). This term describes the migration that occurs in dilute solutions owing to polymer deformation coupling to streamline curvature. Dill and Zimm (1979) reported that DNA migration can arise from such a term in a curvilinear shearing flow, produced for example by torsional shearing between a cone and plate, which has also been experimentally confirmed for polystyrene solutions by MacDonald and Muller (1996). Watari *et al*. (2008) reported that in a Taylor vortex flow or an electro-osmotic flow, such migration can even lead to a fluidic trapping of deformable polymers. A second order velocity gradient term also is present in flow through a channel with a groove along the side, and, indeed, polymer migration also occurs in simulations in this geometry, even in the absence of hydrodynamic interactions [Hernández-Ortiz *et al*.(2008)]. In strictly rectilinear flows, for example Poiseuille flows in a slit or square straight channel, no streamline curvature exists to produce cross-streamline migration. However, as shown in Figure 4.8, in our contraction flow, one component of the curvature points toward the centerline, which could drive polymer migration in that direction. Dill (1979) estimated the migration rate v_r in the torsional shearing flow to be,

$$v_r \sim \frac{\eta_s \dot{\gamma}^2}{r k_B T} R_0^5 \qquad (4.4.1.2)$$

where r is the radial position, R_0 is the root-mean-square end-to-end vector of the polymer coil at equilibrium, η_s is the solvent viscosity and $\dot{\gamma}$ is the shear rate. In our contraction flow, there are

curved streamlines as shown in Figure 4.8, and the observed polymer migration towards the channel centerline is presumably due to the curvature of the streamlines. From Eq. (4.4.1.2), we can work out a dimensionless group $\Pi = \frac{v_r r}{D} \sim \frac{\eta_s R_g^5}{k_B T D} \dot{\gamma}^2$, where $R_g = \frac{R_0}{\sqrt{6}}$ and D are the radius of gyration and the center-of-mass diffusivity of the polymer chain, respectively. Note in Zimm theory, the relaxation time of the polymer is approximately $\tau \sim \frac{\eta_s R_g^3}{k_B T}$, so that $\tau \sim \frac{R_g^2}{D}$, and therefore $\Pi \sim \mathrm{Wi}^2$. If we change N_s, the length of the polymer chain, we can hold $\Pi \sim \mathrm{Wi}^2$ fixed by adjusting the acceleration g, thus adjusting the shear rate $\dot{\gamma}$ to offset the change in relaxation time produced by the change in N_s. Note that in the BD simulation without HI, the chains are Rouse chains for which D is inversely proportional to the product of the chain length N_s and the bead drag coefficient, rather than scaling as $D \sim \frac{k_B T}{\eta_s R_g}$, as in Zimm theory with dominant HI. So to hold Π fixed, in addition to adjusting g, we also adjust D through adjustments of the bead drag coefficient, so that D scales with N_s as in the Zimm theory. One can see in Figure 4.9 that, at the same Wi (i.e., the same Π), the spatial distributions of chains of different lengths almost overlap. The small discrepancies between them at the right and left edges are because of the difference in the sizes of the wall depletion zones for these chains of different lengths. We expect the polymer chain with the largest Wi to migrate the most towards the centerline of the channel as is indeed shown in Figure 4.10. At low Wi (Wi=0.25), the polymer distribution is almost flat, while at large Wi (Wi=7.5), the migration becomes so strong that most of the polymer resides near the centerline in a zone of width comparable to that of the narrow channel.

The mean residence time μ is determined by the spatial distribution, i.e. how the polymer samples the flow field. From Figure 4.11, one can see that when the streamline-curvature-induced migration becomes important (Wi > 1), values of μ normalized with μ_f (the mean residence time of a fluid element) for different chain lengths converge to almost the same value due to the similarity of their spatial distributions. As Wi increases, the polymer distribution becomes more and more confined to a zone of width similar to that of the narrow channel, and then becomes insensitive to further increases in Wi; thus μ also ceases to decrease with increasing Wi, as shown in Figure 4.11 However, we note that for short chains (N_s=5), as Wi is driven even higher, μ starts to rise. This results from the widening of the spatial distribution and the dip that appears at the center of the channel as shown in Figure 4.12 The longer the chain, the larger the Wi at which such dip occurs. For N_s=15, the dip appears at $\mathrm{Wi} \approx 75$. Such a dip was also observed in other studies for which HI was present [Cannavacciuolo *et al*.(2008), Jendrejack *et al*.(2004), Usta *et al*.(2005), Hernández-Ortiz *et al*.(2007), Hernández-Ortiz *et al*.(2008)]. In these previous works, the dip occurred because the less stretched polymer at the center had a higher diffusivity (due to internal HI within the chain) than the more stretched polymer located slightly off the center [Butler *et al*.(2007)]. In our BD simulations, however, there is no HI, and the polymer conformation will not affect its diffusivity. We confirm this by carrying out BD simulations in a uniformly straight channel, for which we find that, outside of the polymer depletion zones near the wall, the polymer distributes uniformly across the channel. This dip in our contraction flow is thus presumably due to spatial variation in the rate of the streamline-induced-migration. Near the centerline, the streamline curvature is reduced and so is the migration rate. At this point, however, we cannot give a detailed explanation for the dip beyond attributing it to the entry effect combined with streamline curvature.

When Wi exceeds 10, migration induced by wall HI starts to take effect [Jendrejack *et al*.(2004)]. However such migration takes time to build up, and the time scale required for it to lead to a significant concentration difference, as estimated from Jendrejack *et al*.(2004), is much larger than the residence time of the polymer chain in either the narrow channel or the wide chamber, and so the effect of migration due to HI should be small. Moreover, in the wide chamber, Wi is one order of magnitude smaller than in the narrow channel, so the migration due to HI is still small even when Wi ~ 30 in the narrow channel. Thus, streamline-curvature induced migration dominates in our simulations. Therefore, we expect that predictions from BD simulations would not change much if full HI were taken into account at moderate Wi (10 ~ 30).

4.4.2. Taylor Dispersion

The effective longitudinal diffusivity of a Brownian object along a channel can be much larger than its center-of-mass diffusivity *D*, because of the variation of velocity with distance from the center of the channel. Molecules on different streamlines are convected at different rates, which increases their longitudinal spreading, while cross-stream diffusion mixes molecules between streamlines, thus reducing their longitudinal spreading. Hence, an increased molecular diffusivity actually leads to a smaller longitudinal spreading. The longitudinal spreading becomes Gaussian in a long enough tube or channel and is referred as Taylor dispersion [Taylor (1953)].

At steady state, the longitudinal effective diffusivity D_{eff} (or dispersivity) is related to the standard deviation of the residence time σ as $D_{\text{eff}} = \frac{1}{2}\frac{(\bar{v}_{\text{L}}\sigma)^2}{\mu}$, where $\bar{v}_{\text{L}}$ is the average velocity of the polymer along the longitudinal direction and μ is the mean residence time. Taylor dispersion is controlled by the Peclet number Pe which for a channel flow is given by $\text{Pe} = \frac{Q}{D}$, where *Q* is the volumetric flow rate per unit depth of the channel, and *D* is the center-of-mass

diffusivity. We followed Taylor (1953), and derived the effective diffusivity D_{eff} for a slit channel, depending on Pe as:

$$\frac{D_{\text{eff}}}{D} = 1 + \frac{\text{Pe}^2}{\xi} \tag{4.4.2.1}$$

with

$$\xi^{-1} = \int_{\varepsilon}^{1-\varepsilon} \mathrm{d}x \left(-6x^2 + 6x - 1\right)\left(-\frac{1}{2}x^4 + x^3 - \frac{1}{2}x^2 - \alpha x - \beta - \gamma\right) \tag{4.4.2.2}$$

where

$$\alpha = -2\varepsilon^3 + 3\varepsilon^2 - \varepsilon \ , \ \beta = \frac{3}{2}\varepsilon^4 - 2\varepsilon^3 + \frac{1}{2}\varepsilon^2 \ , \ \gamma = \int_{\varepsilon}^{1-\varepsilon} \mathrm{d}x \left(-\frac{1}{2}x^4 + x^3 - \frac{1}{2}x^2 - \alpha x - \beta\right) \ , \ \varepsilon = R_{\text{g}} \big/ w \ ,$$

w is the width of the narrow channel, and R_{g} is the radius of gyration of the polymer.

As a reference, we first consider Taylor dispersion in a straight planar channel, for which the value $\xi = 210$ is obtained from analytical theory. As expected, D_{eff}/D for a monomer as a function of Pe obtained from the BD simulations exactly follows the theoretical curve, as shown in Figure 4.13. Due to size-induced depletion from the wall, polymers cannot fully sample the flow field near the wall; therefore the Taylor dispersion of polymers is smaller than that of the monomers, i.e. their dispersion is characterized by a larger ξ than for monomers. We can estimate the value of ξ for polymers in a slit channel of width w by assuming that the polymer center of mass is uniform across the channel except for a wall zone of width equal to the polymer radius of gyration R_{g} from which the polymers are completely excluded. With this assumption, the expression for ξ as a function of $\varepsilon = R_{\text{g}}/w$ is given in Eq. (4.4.2.2), from which we calculated the values appearing in the last column of Table 3. The other values of ξ in Table 4.3 are from fits of the data in Figure 4.13 to Eq. (4.4.2.1). The fitted ξ is smaller than the analytical

value, presumably because the polymer is not completely excluded from the depletion zone. We note that as the chain gets longer, the fitted value approaches more closely the analytical one. This might be expected, since chains with more beads will be more completely excluded from the wall region.

In a straight channel, the longitudinal Taylor dispersivity D_{eff} reduces to the molecular diffusivity D as Pe becomes small. In the contraction channel however, as the velocity approaches zero, the dispersivity actually drops below D, as in Figure 4.14. This may occur because in the contraction geometry, the average path length for diffusion is longer than the longitudinal distance down the channel, and this effect evidently is greater than any additional spreading that results from the higher variability in particle path lengths due to the contraction, at least for the particular aspect ratio considered.

For chains at low Pe, where Wi is also low since $\text{Wi} \sim \left(\frac{R_g}{w} \right)^2 \text{Pe}$, the chains are undeformed and their dispersion curves follow that of the monomer as shown in Figure 4.14. As Pe increases, so that Wi exceeds 2 (at points indicated by the arrows in Figure 4.14). the chains are able to deform significantly in the flow, and we can see their dispersion curves start to "roll off" from that of the monomer. Note that it is at $\text{Wi} \approx 2$ that streamline-curvature-induced migration starts to become important. Therefore as Wi increases above this value, the polymers become increasingly confined near the centerline and thus the dispersion is reduced. However a larger Wi also means that Pe increases, which tends to increase the dispersion. The balance between these two mechanisms may account for the saturation of the dispersivity for long chains (N_s = 15). However for the short chains (N_s = 5), before reaching the balance mentioned above, their spatial distribution starts to widen as shown in Figure 4.12; therefore their dispersion keeps increasing even at high Pe. For longer chains (N_s = 10 or 15), after the dispersivity begins to saturate at high

Pe, at still higher Pe it begins to increase again. This occurs at the point that the polymer chains have become largely concentrated in a zone at the center of the chamber, hardly wider than the thin channel. This appears to be the condition for saturation of the effect of migration induced by streamline curvature; further increases in Pe are not able to increase the confinement of the chain. Thus, from this point, upon further increase of Pe, the dispersion behaves similarly to that in the straight channel and starts to rise again. Moreover, since for Taylor dispersion $D_{\text{eff}}/D \sim \text{Pe}^2$ at high Pe and $\text{Wi} \sim \left(\frac{R_g}{w}\right)^2 \text{Pe} \sim N_s \text{Pe}$, we expect that the quantity $N_s^2 D_{\text{eff}}/D$ for chains of different length should collapse if plotted against Wi, which is the case as shown in Figure 4.15.

4.5.Polymer separation

In this section, we show the potential for polymer separation in a multi-step contraction channel using the principle of the central limit theorem (CLT).

For the same pressure drop, and thus the same shear rate, a longer chain has a larger Wi and migrates more towards the centerline of the channel as shown in Figure 4.17, and therefore has a shorter mean residence time. So to separate two polymers of different length, one needs the standard deviations of the residence time to be smaller than the difference of their means. If this is not the case in a one-pass contraction geometry as shown in Figure 4.16, then, based on central limit theorem, it can be realized in a multi-step contraction channel.

Let $\tau^{(n)}$ denote the *n*-pass residence time, that is the time a polymer takes to pass *n* sequential contractions, which is equivalent to passing the one-step contraction channel periodically *n* times. To predict the RTD in a multi-step channel using the CLT, first we need to know the value of *n* at which sequential $\tau^{(n)}$ values become de-correlated, namely at which their auto-correlation

becomes almost zero. This auto-correlation can be written as $\left\langle \left[\tau(j) - \tau(j-n) - \bar{\tau}^{(n)} \right] \left[\tau(j+n) - \tau(j) - \bar{\tau}^{(n)} \right] \right\rangle \Big/ \left(\bar{\tau}^{(n)} \right)^2$, where $\tau(j)$ is the time at which the polymer passes the *j*-th contraction and $\bar{\tau}^{(n)}$ is the average *n*-pass residence time. This auto-correlation function will become almost zero when *n* is large enough, and the larger Wi is, the larger this *n* will be. As shown in Figure 4.18, at Wi = 2.5 (obtained for a 10-spring chain at g = 0.02), the auto-correlation between sequential 1-pass residence time is less than 10%, and the 2-pass residence time shows an even smaller correlation, about 2%. This indicates the residence time of every 2 sequential passages is almost completely un-correlated. However, at Wi = 12.5, 7 passages are required for the correlation to drop below 2%. To calculate D_{eff}, defined in the previous section, one has to use the standard deviation of an uncorrelated *n*-pass residence time.

In addition, since the residence time has a long tail at long times as shown in Figure 4.16, to get an accurate standard deviation, one has to run the simulation long enough to sample fairly the tail of the distribution. For this purpose the BD simulation method is more attractive than SRD, due to the high computational efficiency of BD simulation, which is about 15 times faster than SRD.

The histogram in Figure 4.19 shows the RTD of a 100-step contraction channel for a 10-spring chain at Wi = 2.5. The solid line is the Gaussian distribution expected for the 100-pass RTD, namely $\mathcal{N}(\mu^{(2)}, \frac{\sigma^{(2)}}{\sqrt{N/2}})$, where $\mu^{(2)}, \sigma^{(2)}$ are the mean and standard deviation of the 2-pass residence time distribution normalized by the mean residence time of a fluid element. Here $N/2 = 50$ is the number of independent sequential double-passes in the run of 100 passes, leading to a standard deviation of $\frac{\sigma^{(2)}}{\sqrt{N/2}}$ for the 100-pass distribution, according to the central

limit theorem. Also plotted in Figure 4.19 is the actual RTD obtained by simulating directly an entire 100-pass run, giving the RTD of a long channel with 100- contraction steps. Figure 4.19 shows that this RTD histogram is almost Gaussian-like, although still a little skewed, with skewness of 0.6, reduced greatly from the skewness of 6.4 of the highly skewed 1-pass RTD shown as the dashed curve in Figure 4.19 (Skewness is the sample third central moment normalized by the cube of the standard deviation.) Figure 4.19 indicates that at Wi = 2.5, the assumption of statistical independence of the residence time after two passes through the geometry is a good approximation, and that 50 repeats of the two passes is enough to sample the distribution of residence times well enough for the initially skewed distribution to revert nearly to a Gaussian, as expected from the central limit theorem.

This convergence to the Gaussian predicted by the central limit theorem allows us to predict the RTD's for a polymer passing through an *N*-step contraction channels, using the RTD for a much shorter *n*-step contraction, by simply using $\mathcal{N}(\mu^{(n)}, \frac{\sigma^{(n)}}{\sqrt{N/n}})$.

Figure 4.20 shows the residence time distribution of 600-step contraction channel predicted by central limit theorem for polymer chains of 5,10, and 15 springs at the same shear rate (same value of *g*). We can see that we can expect 5-spring and 10-spring chains to be very well separated after 600 contraction steps. The 10-spring and 15-spring chains are also reasonably well separated.

We now define $\lambda_{ij}(N)$, the efficiency of separation of *i*-spring chains from *j*-spring chains in an *N*-step contraction channel, as,

$$\lambda_{ij}(N) = \sqrt{\frac{N}{n}} \frac{|\mu_i^{(n)} - \mu_j^{(n)}|}{|\sigma_i^{(n)} + \sigma_j^{(n)}|} \tag{4.5.1}$$

where $\mu_i^{(n)}, \sigma_i^{(n)}$ are the mean and standard deviation respectively of the uncorrelated *n*-pass RTD of an *i*-spring chain. By adjusting the flow rate, it is interesting to see in Figure 4.21 that the best separation is achieved at Wi around 2, which is the value of Wi at which the chains transition from un-stretched to stretched as discuss in the previous Section 4.4.2.

If we decrease the shear rate so that Wi drops below unity, the chains are no longer stretched. Since their radii of gyration are comparable to the width of the narrow channel, the longer chain (N_s=15, $w/R_g = 1.6$) will find it more difficult to enter the narrow channel than the shorter chains (N_s=10, $w/R_g = 1.9$). So at low Wi, this blockage effect can also separate the polymers as shown in Figure 4.22(bottom). However the longer 15-spring chains migrate slower than the 10-spring chains do, rather than migrating faster than the shorter chains as is the case at high Wi, shown in Figure 4.22(top). From the figure, we can also see that the blockage effect gives a better separation between 10-spring and 15-spring chains than does the curvature-induced migration, and that the separation will be even better if we further shrink the width of the narrow channel. But it takes a 100-fold longer time to achieve this better separation because of the reduced flow rate, since the acceleration *g* is reduced from 2×10^{-2} to 2×10^{-4}.

In traditional size-exclusion chromatography (SEC), the long chains experience not temporary *blockage* from small pores through which they must eventually pass, but *exclusion* from side regions, thereby speeding their motion through the remaining available pore space. Therefore, in SEC, the large polymers move faster than the small ones, as is the case in our simulations at high Wi. However, in our simulations the high-Wi exclusion of large chains from the side regions is

not due to polymer size, but to a curvature-induced migration that is sensitive to chain deformation and therefore to Weissenberg number. Hence, there are at least three mechanisms of separation: size exclusion, blockage, and curvature-induced migration, and in our simulations the latter two are dominant. When the blockage effect is dominant, the ratio μ/μ_f is larger than unity, where μ and μ_f are the mean residence time of the polymers and fluid respectively. When curvature-induced migration is dominant, μ/μ_f is less than unity.

4.6.Conclusions and final remarks

We have simulated the migration of a single polymer chain through a period pressure-driven planar contraction channel from low (~ 0.03) to moderate (~ 30) Weissenberg numbers (Wi), where Wi is defined based on the shear rate in the narrow channel of a contraction channel (contraction ratio 5.5). (In the wide chamber of the geometry, the effective Weissenberg number is an order of magnitude smaller.) The width of the narrow region of the contraction channel is chosen to be comparable to the radius of gyration of the chains studied. When Wi < 1, and chains are un-deformed, we find that the mean residence time of the polymer is smaller than that of the fluid and size-dependent blockage of the chain from the thin channel dominates the residence time distribution of the polymer, so that long chains migrate slower than short chains. For 1 < Wi < 2, the long polymers are modestly stretched, and migrate faster than short chains. In this range of Wi, the Taylor dispersion coefficient normalized by the polymer diffusion coefficient is higher by an order of magnitude than for undeformable monomers due to curvature-induced migration, but depends on Peclet number in a similar way. The curvature-induced migration is similar to that reported by Dill and Zimm (1979) and confirmed by MacDonald and Muller (1996) in torsional shearing flow. The rate of migration produced by this

mechanism is proportional to Wi^2. For Wi > 2, polymers are highly stretched as they pass into the narrow channel and the migration reaches a saturation condition, so that the dispersivity no longer increases as rapidly with increasing Wi. By comparing the spatial distributions and the residence time distributions of the polymer chains from SRD simulations, which include hydrodynamic interaction (HI), with those from BD simulations without HI, we find that HI has only a weak effect on polymer migration. Although Jendrejack *et al*. (2004) and Kekre *et al*. (2010) have reported that for long straight micro-channels, migration induced by HI between the wall and the polymer can produce large concentration gradients across the channel, this effect is weak for Wi < 10, and is slow even for much higher Wi. Since the thin channels considered here are broken up by intervening large chambers, the influence of wall HI appears to be minimal. Thus, for the periodic contraction geometry considered here, fast BD simulations are adequate for studying polymer migration in the contraction channel for Wi up to at least around 30.

Using the central limit theorem, we have demonstrated the potential for polymer separation using a multi-step pressure-driven planar contraction channel with a few hundred steps. At low Wi where $\mu / \mu_f > 1$, the longer chains have a larger mean residence time than the shorter chains do, and the polymers separate due to the blockage effect at the entrance to the narrow channel. However such separation is very slow because of the slow flow rate needed to avoid chain stretch. When Wi is above unity, the polymers are stretched, and in this case the longer chains migrate to the center of the wide region of the channel due to streamline-curvature-induced migration and therefore have a shorter mean residence time than the longer chains do. For this separation mechanism, one can achieve the best separation by adjusting the shear rate to the region where Wi is around 2.

References

Butler, J.E., O.B. Usta, R. Kekre and A.J.C. Ladd, "Kinetic theory of a confined polymer driven by an external force and pressure-driven flow," *Physics of Fluids* **19**, 113101 (2007).

Cannavacciuolo, L., R.G. Winkler and G. Gompper, "Mesoscale simulations of polymer dynamics in microchannel flows," *Europhysics Letters* **83**, 34007 (2008).

Dill, K.A., "Theory for the separation of very large DNA molecules by radial migration, " *Biophys. Chem.* **10**, 327-334 (1979).

Dill, K.A. and B.H.Zimm, "A rhelogical separator for very large DNA molecules," *Nucleic Acids Res.* **7**, 735 (1979).

Gompper, G., T. Ihle, D. M. Kroll, R. G. Winkler, "Multi-Particle Collision Dynamics: A Particle-Based Mesoscale Simulation Approach to the Hydrodynamics of Complex Fluids," *Advances in Polymer Science* **221**, 1-87 (2008).

Hernández-Ortiz, J.P., J.J. de Pablo and M.D. Graham, "Fast computation of many-particle hydrodynamic and electrostatic interactions in a confined geometry," *Physics Review Letters* **98**, 140602 (2007).

Hernández-Ortiz, J.P., H.B. Ma, J.J. de Pablo and M.D. Graham, "Concentration distributions during flow of confined flowing polymer solutions at finite concentration: slit and grooved channel," *Korea-Australia Rheology Journal* **20**, 143-152 (2008).

Huang, C.C., A. Chatterji, G. Sutmann, G. Gompper and R. G. Winkle, "Cell-level canonical sampling by velocity scaling for multiparticle collision dynamics simulations," *Journal of Computational Physics* **229**, 168-177 (2010).

Ihle, T. and D. M. Kroll, "Stochastic rotation dynamics: A Galilean-invariant mesoscopic model for fluid flow," *Physical Review E* **63**, 020201(4) (2001).

Jendrejack, R. M., J. J. de Pablo and M. D. Graham, "Stochastic simulations of DNA in flow: Dynamics and the effects of hydrodynamic interactions," *Journal of Chemical Phycics* **116**, 7752(8) (2002).

Jendrejack, R. M., D.C. Schwartz, J. J. de Pablo and M. D. Graham, "Shear-induced migration in flowing polymer solution: simulation of long-chain DNA in microchannels", *Journal of Chemical Phycics* **120**, 2513 (2004).

Jiang, L., N. Watari, R.G. Larson, "How accurate are stochastic rotation dynamics simulations of polymer dynamics?" *J. Rheo.* **54**,1177-1194 (2013).

Kekre, R., J.E. Butler, A.J.C. Ladd, "Comparison of lattice-Boltzmann and Brownian-dynamics simulations of polymer migration in confined flows," *Phys. Rev. E* **82**, 011802 (2010).

Lamura, A., G. Gompper, T. Ihle and D.M. Kroll, "Multi-particle collision dynamics: Flow around a circular and a square cylinder," *Europhysics Letters* **56**(3), 319-325 (2001).

Lathe, G.H and C.R.J. Ruthven, "The Separation of Substance and Estimation of their Relative Molecular Sizes by the use of Columns of Starch in Water," *Biochem J.* **62**, 665–674 (1956).

Ma, H.B. and M.D. Graham, "Theory of shear-induced migration in dilute polymer solutions near solid boundaries," *Physics of Fluids* **17**, 083103 (2005).

Macdonald, M.J. and S.J. Muller, "Experimental study of shear-induced migration of polymers in dilute solutions," *J. Rheo.* **40**, 259-283 (1996).

Malevanets, A. and R. Kapral, "Mesoscopic model for solvent dynamics," *Journal of Chemical Physics* **110**, 8805-8613 (1999).

Marko, J. F. and E. D. Siggia, "Stretching DNA," *Macromolecules* **28**, 8759-8770 (1995).

Moore, J.C., "Gel permeation chromatography. I. A new method for molecular weight distribution of high polymers," *J. Polym. Sci.* **2**, 835-843 (1964).

Ripoll, M., K. Mussawisade, R. G. Winkler and G. Gompper, "Low-Reynolds-number hydrodynamics of complex fluids by multi-particle-collision dynamics," *Europhysics Letters* **68**(1), 106-112 (2004).

Taylor, G.I., "Dispersion of soluble matter in solvent flowing slowly through a tube, " *Proc. Roy. Soc. A.* **219**, 186–203 (1953).

Usta, O.B., A.J.C. Ladd, and J.E. Butler, "Lattice-Boltzmann simulations of the dynamics of polymer solutions in periodic and confined geometries", *Journal of Chemical Physics,* **122**, 094902 (2005).

Watari, N., M. Makino, N. Kikuchi, R. G. Larson, M. Doi, "Simulation of DNA motion in a microchannel using stochastic rotation dynamics," *Journal of Chemical Physics* **126**, 094902(7) (2007).

Watari, N., M. Doi and R.G. Larson, "Fluidic trapping of deformable polymers in microflows," *Physical Review E* **78**, 011801 (2008).

Whitmer, J.K., E. Luijten, "Fluid-solid boundary conditions for multiparticle collision dynamics," *Journal of Physics: Condensed Matter* **22**,104106 (2010).

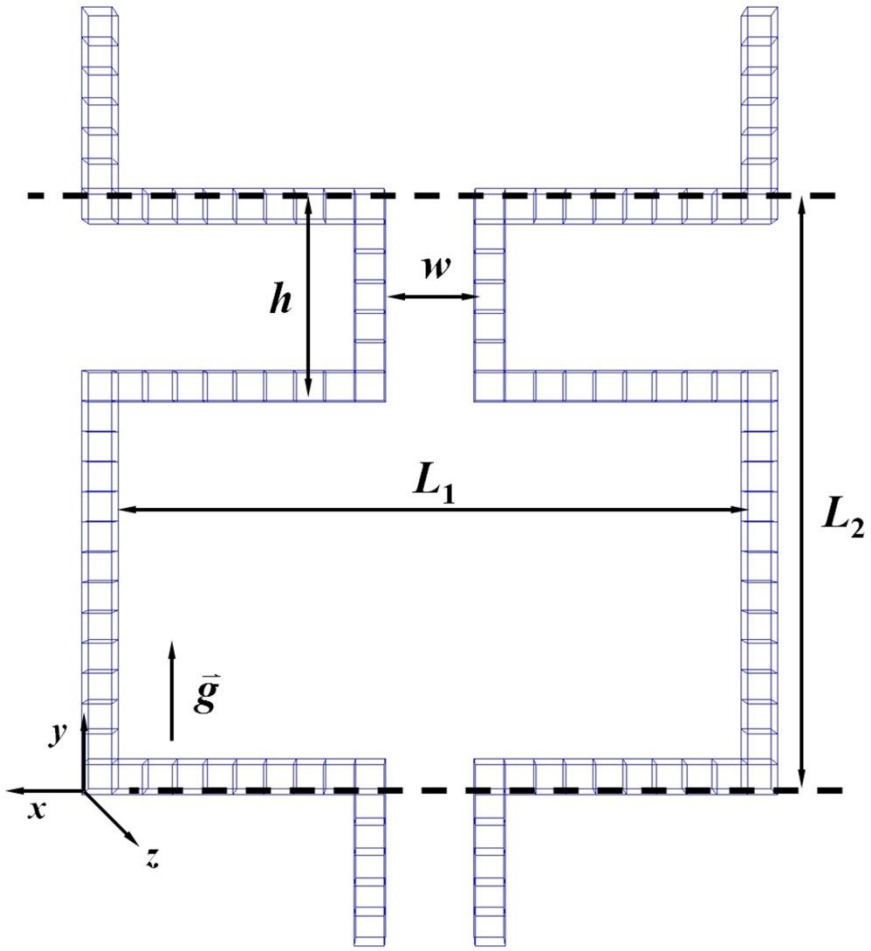

Figure 4.1: Geometry of the planar contraction channel. The parts above and below the dashed lines are periodic images.

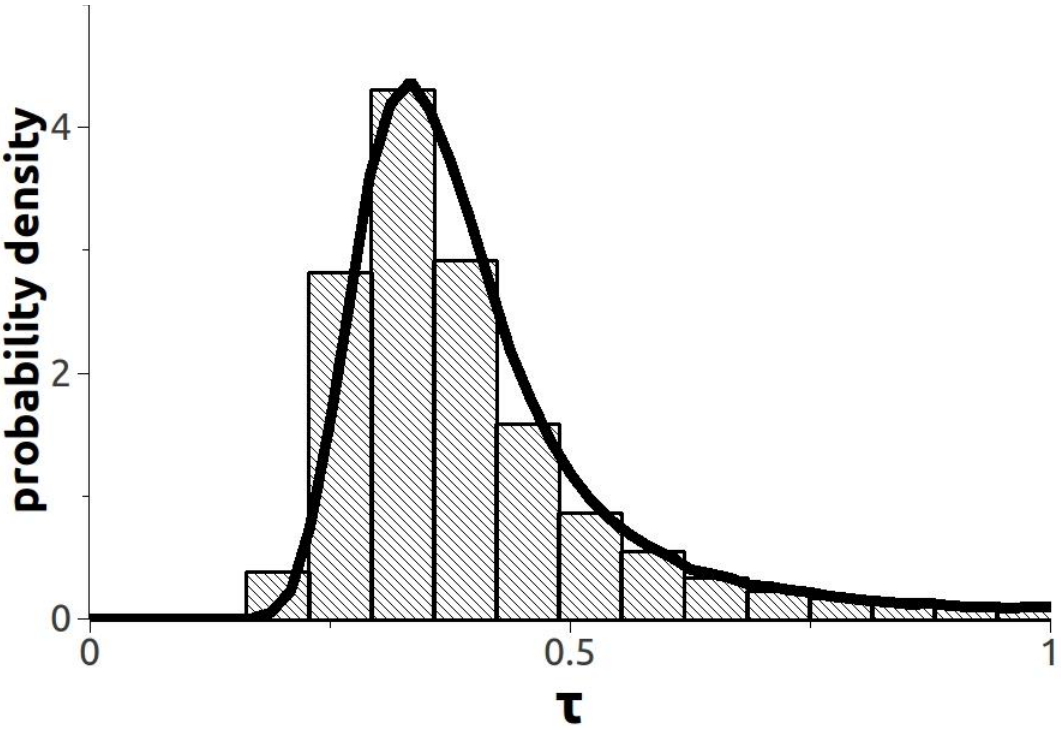

Figure 4.2: Normalized residence time distribution of 10-spring chain simulated by SRD. Solid line is from simulating 75 chains; histogram is from simulating 5 chains.

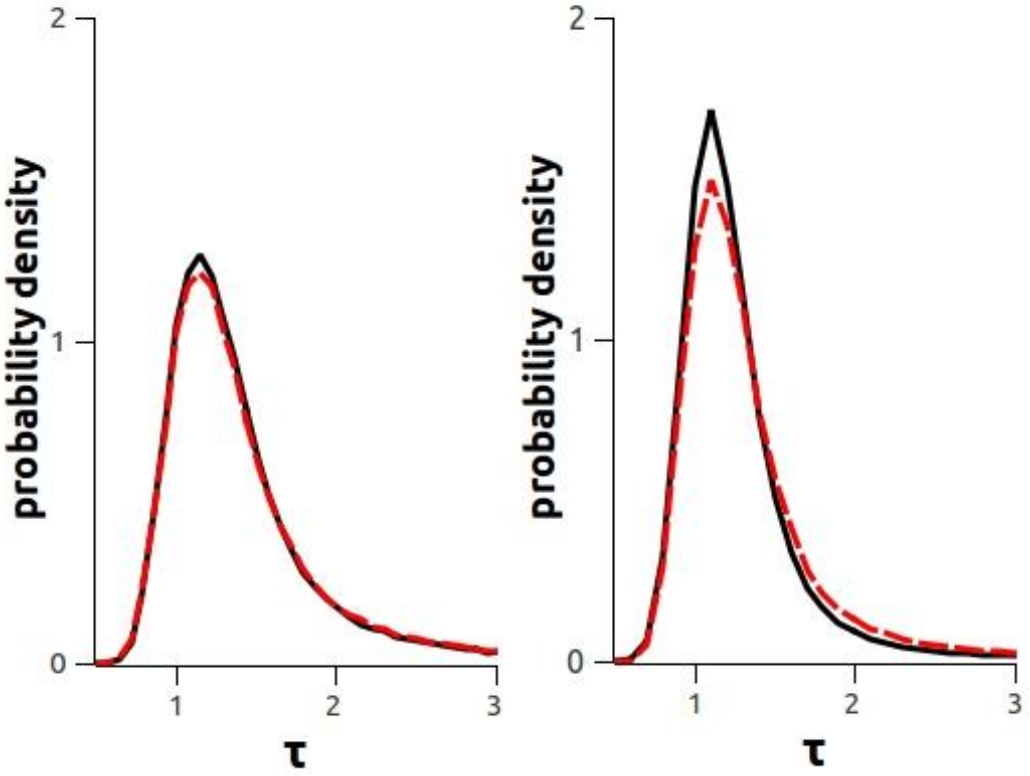

Figure 4.3: Residence time distribution for a 10-spring chain with h^* =0.16 (left) or a 28-spring chain with h^* =0.27 (right). Black solid curves: SRD simulation; red dashed curves: BD simulation without HI with flow field from SRD.

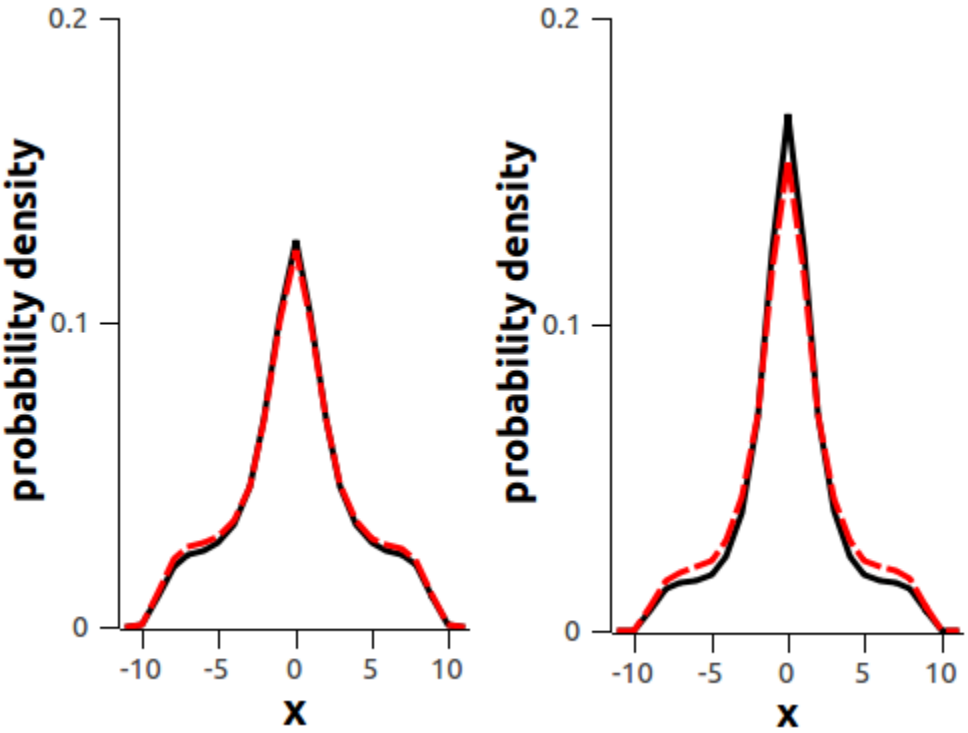

Figure 4.4: Spatial distribution along x direction in the wide chamber for a 10-spring chain with h^* =0.16 (left) or a 28-spring chain with h^* =0.27 (right). Black solid curves: SRD simulation; red dashed curves: BD simulation without HI with flow field from SRD.

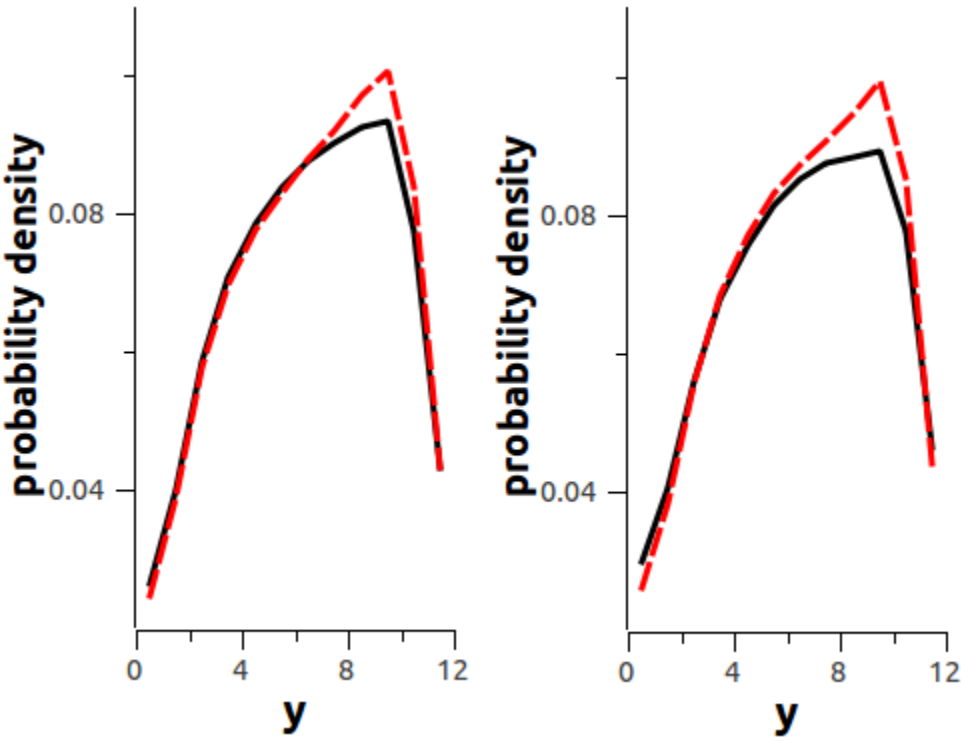

Figure 4.5: Spatial distribution along *y* direction in the wide chamber for a 10-spring chain with h^* =0.16 (left) or a 28-spring chain with h^* =0.27 (right). Black solid curves: SRD simulation; red dashed curves: BD simulation without HI with flow field from SRD.

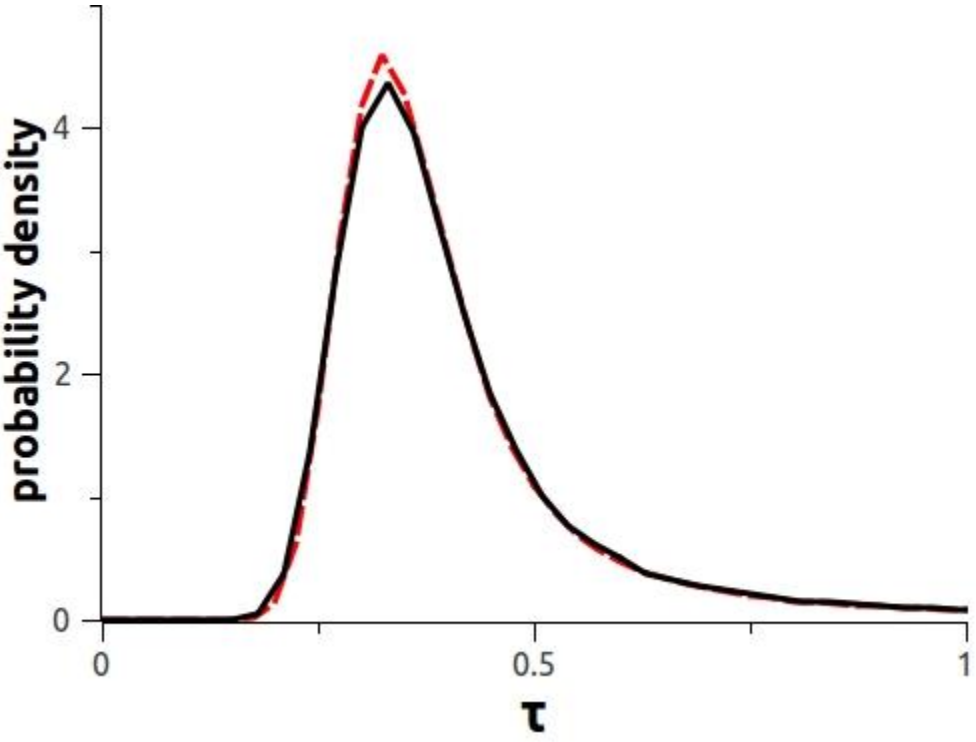

Figure 4.6: Residence time distribution for 10-spring chains. Black solid curve: SRD simulation with h^* =0.16; red dashed curve: BD simulation without HI with flow field resolution a=0.2 from FEM, using the modified boundary for polymers.

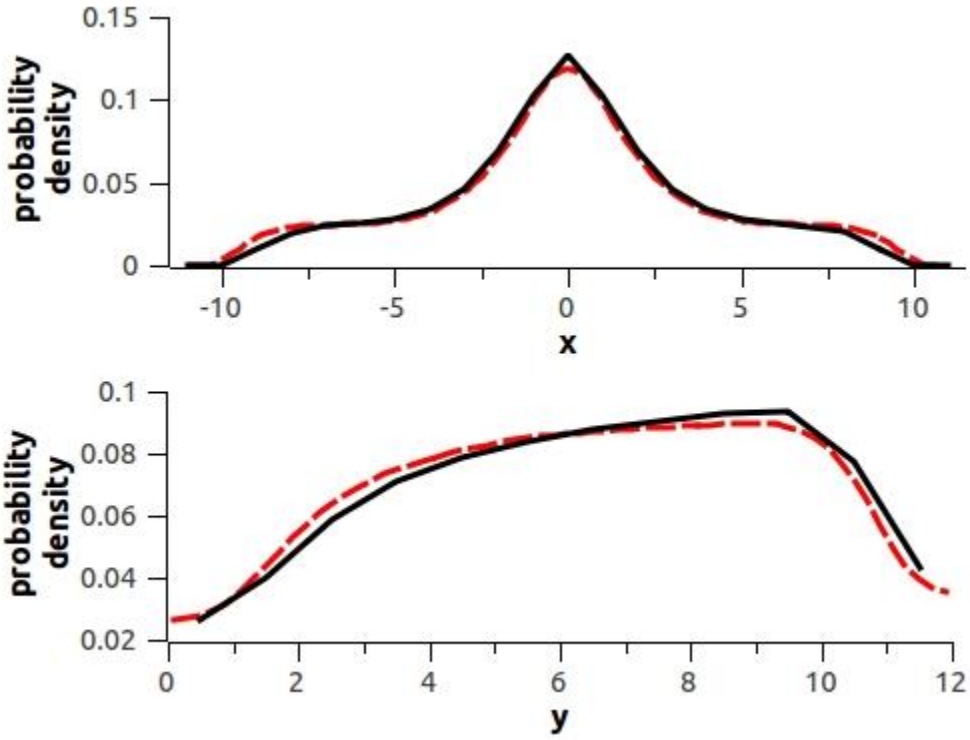

Figure 4.7: Spatial distribution along x (top) and y (bottom) in the wide chamber for 10-spring chains. Black solid curve: SRD simulation with h^* =0.16; red dashed curve: BD simulation without HI with flow field resolution a=0.2 from FEM, using the modified boundary for polymers.

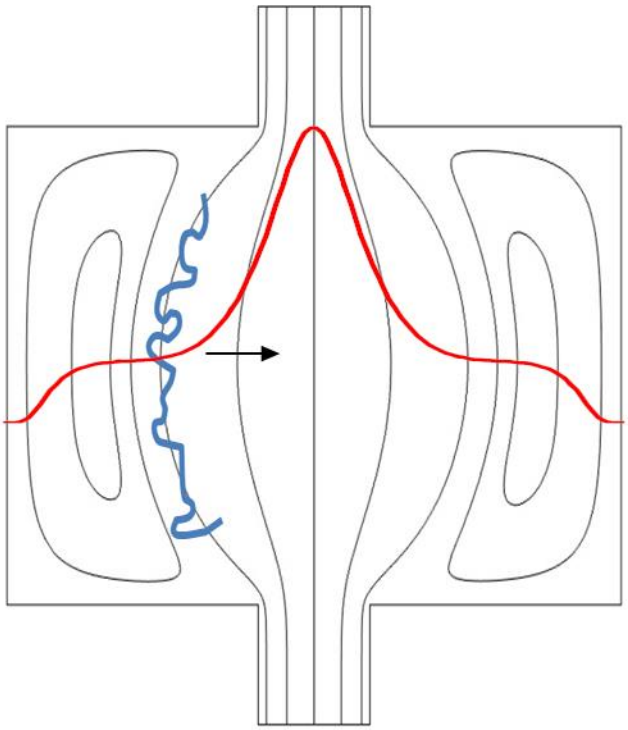

Figure 4.8: Schematic of streamline-curvature-induced migration in the contraction flow. The black lines are the streamlines from the FEM simulation; the red is the spatial distribution of a 10-spring polymer at Wi=2.5, and the blue is a schematic polymer chain; the arrow indicates the direction of the migration.

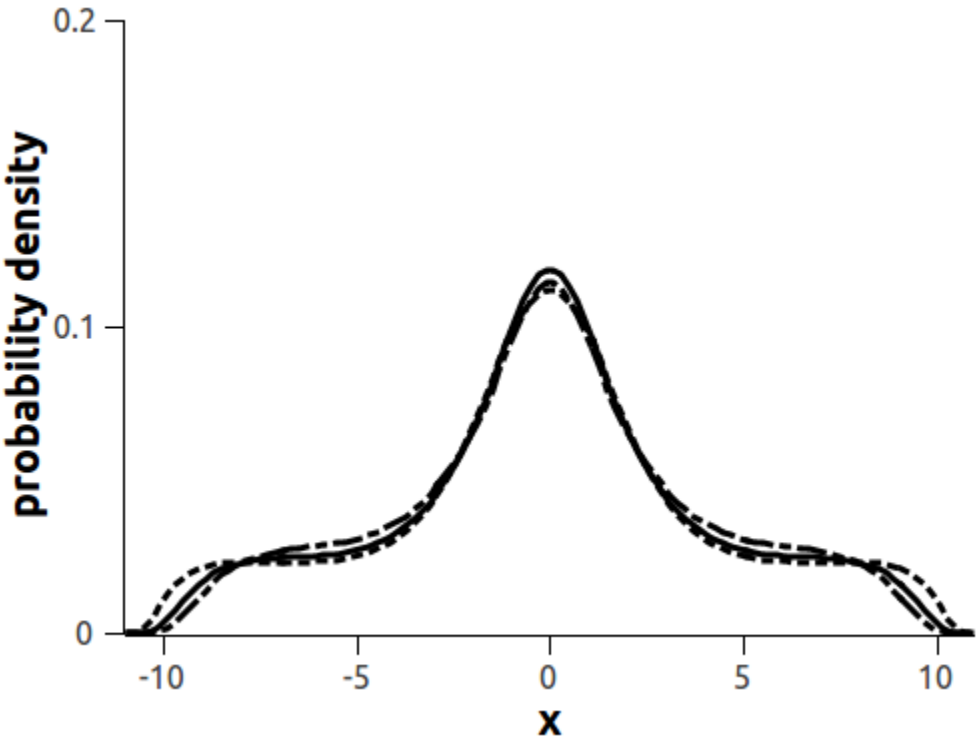

Figure 4.9 Spatial distribution along x in the wide chamber for chains of different lengths at Wi=2.5; dashed curve: N_s=5, solid curve: N_s=10, dot-dashed curve: N_s=15.

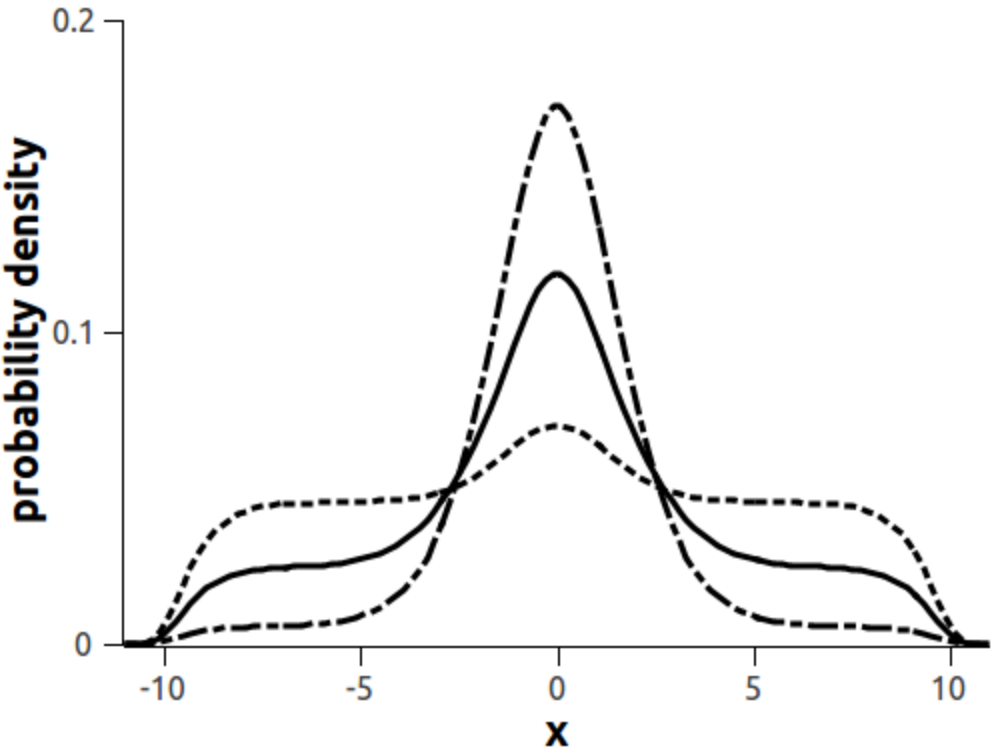

Figure 4.10: The same as Figure 4.9 except for 10-spring chains at different Wi; dashed curve: Wi=0.25, solid curve: Wi=2.5, dot-dashed curve: Wi=7.5.

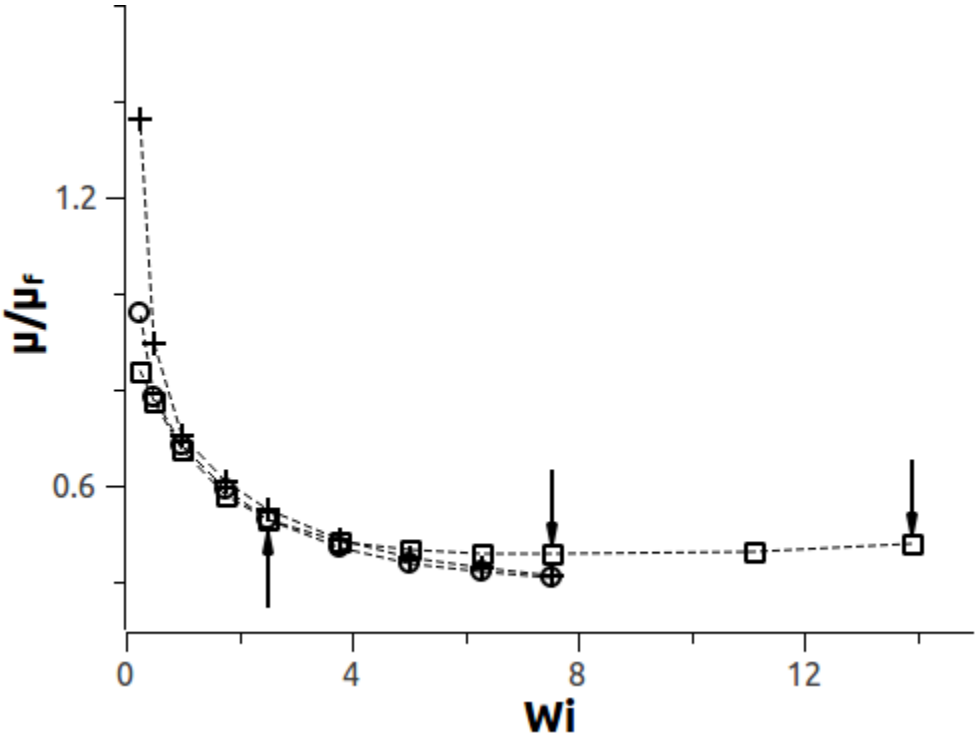

Figure 4.11: The mean residence time μ normalized by μ_f, the mean residence time of a fluid element, against Wi for chains of different length; squares: 5-spring chain, circles: 10-spring chain, pluses: 15-spring chain, where the dashed lines are all guides to the eye.

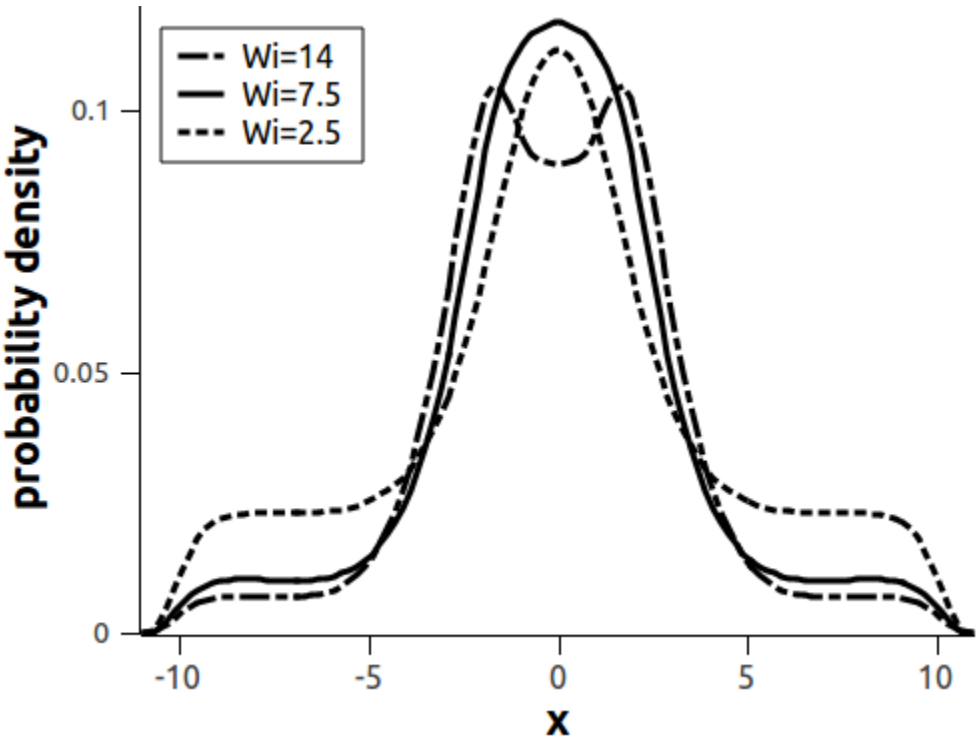

Figure 4.12: The spatial distribution of a 5-spring chain at different Wi corresponding to the arrows in Figure 4.11.

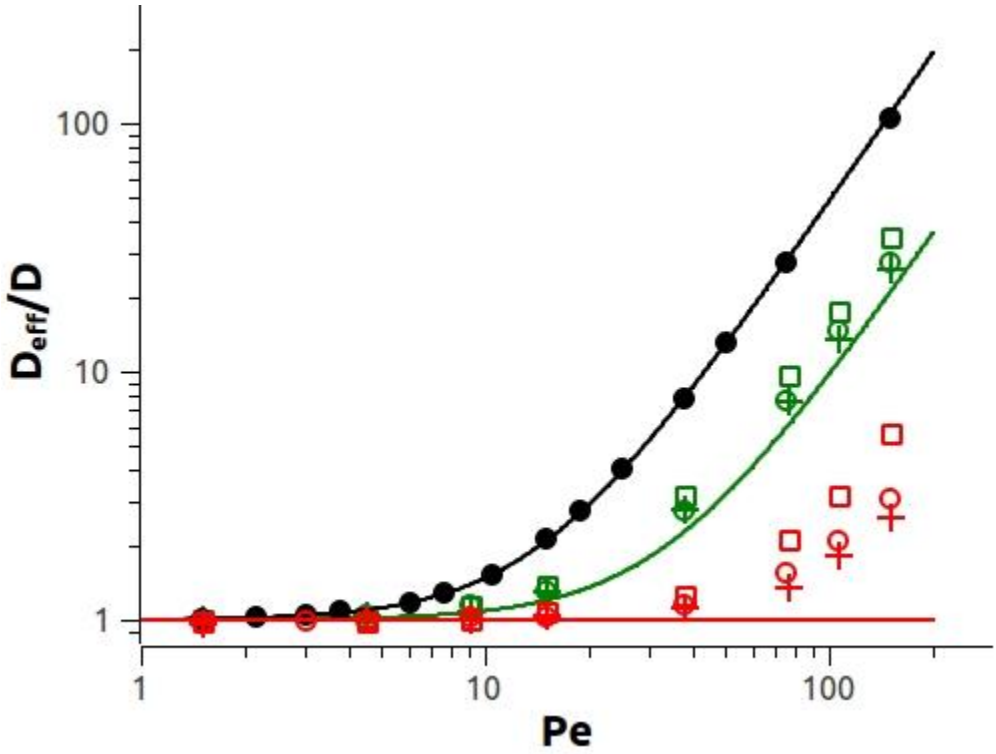

Figure 4.13: Taylor dispersivity versus Peclet number Q/D in an infinite straight channel of width w. The solid curves are from Eq. (4.4.2.1) using analytical values of ξ derived from Eq. (4.4.2.2). The symbols are from simulations; solid circles: monomer, squares: 5-spring chain, circles: 10-spring chain, pluses: 15-spring chain; the black line and black symbols: $\varepsilon = 0$, the green: $\varepsilon = 1/8$, the red: $\varepsilon = 1/2$, where $\varepsilon = R_g / w$.

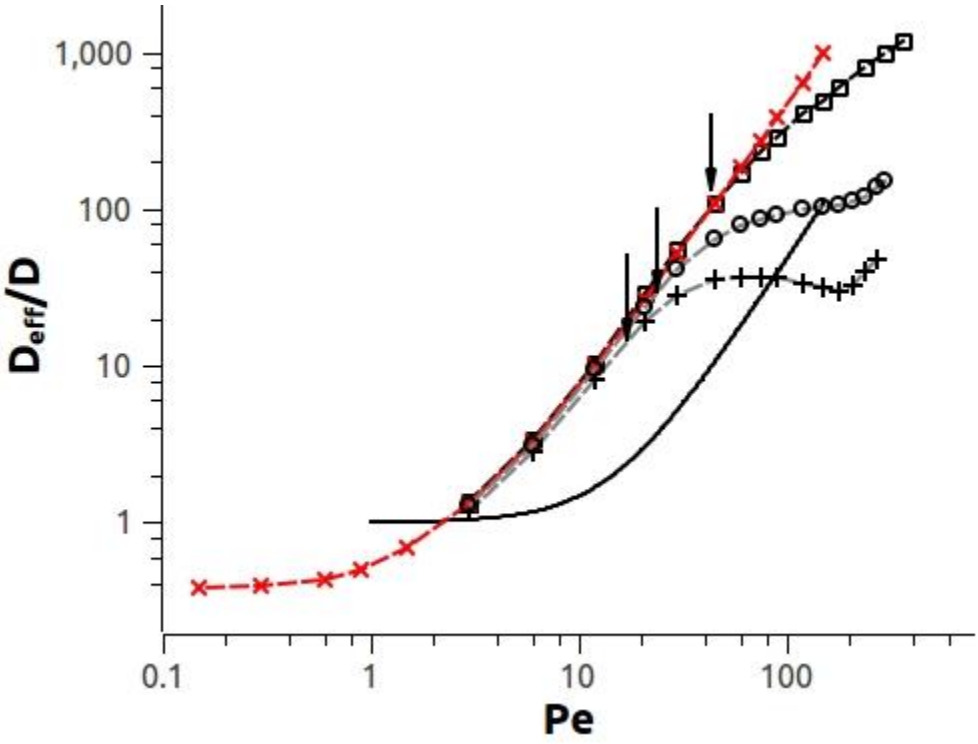

Figure 4.14: Taylor dispersivities in the planar contraction channel versus Pe. Red crosses: monomer, squares: 5-spring chain, circles: 10-spring chain, pluses: 15-spring chain, where the dashed lines are all guides to the eye. Black solid curve: monomer in the planar straight channel. The arrows point to values of Pe at which Wi = 2 for chains of different lengths, from left to right: N_s = 15, 10, 5.

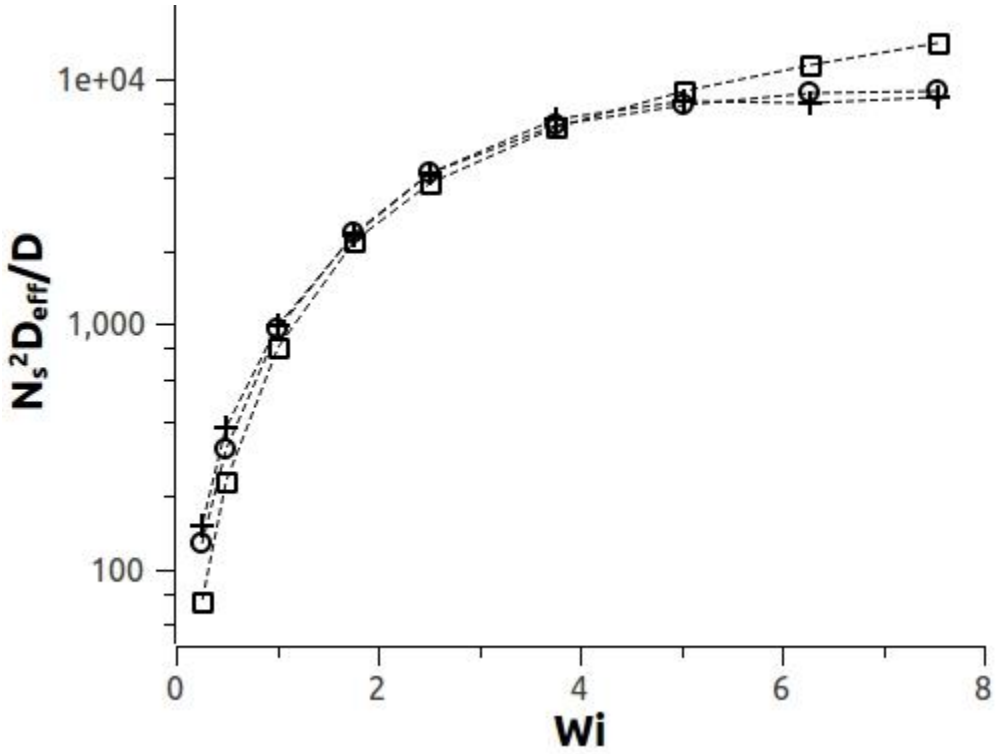

Figure 4.15: Taylor dispersivities in the planar contraction channel versus Wi. Squares: 5-spring chain, circles: 10-spring chain, pluses: 15-spring chain, where the dashed lines are all guides to the eye.

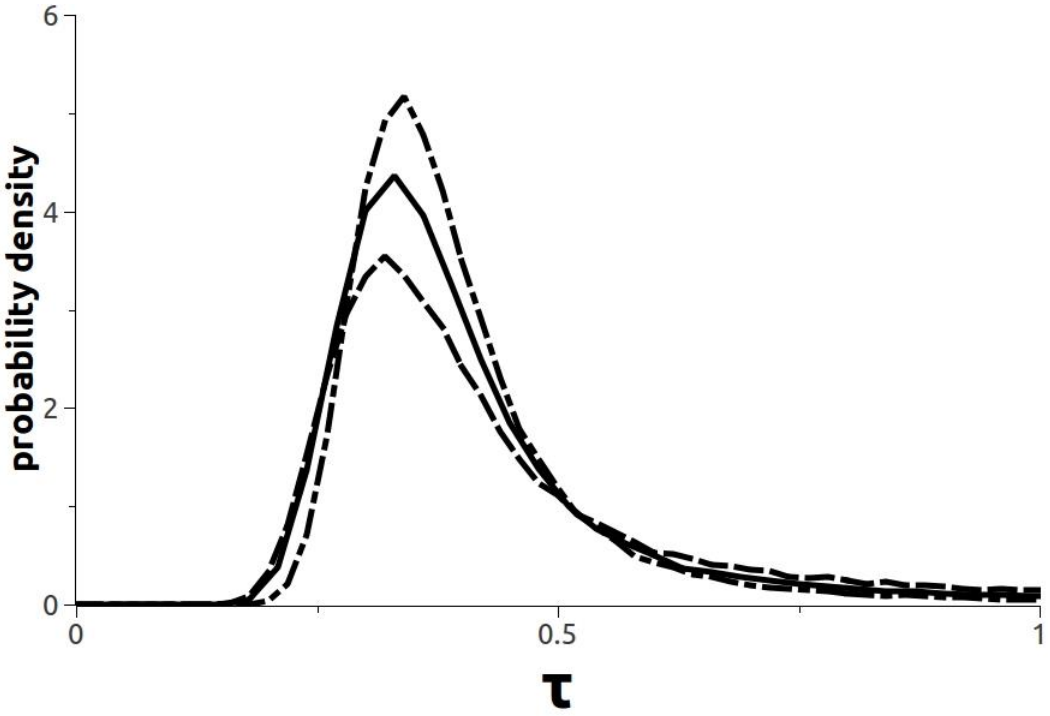

Figure 4.16: One-pass residence time distribution of different length polymers at the same shear rate by applying an acceleration g = 0.02. Dashed curve: 5-spring chain, solid curve: 10-spring chain, dot-dashed curve: 15-spring chain.

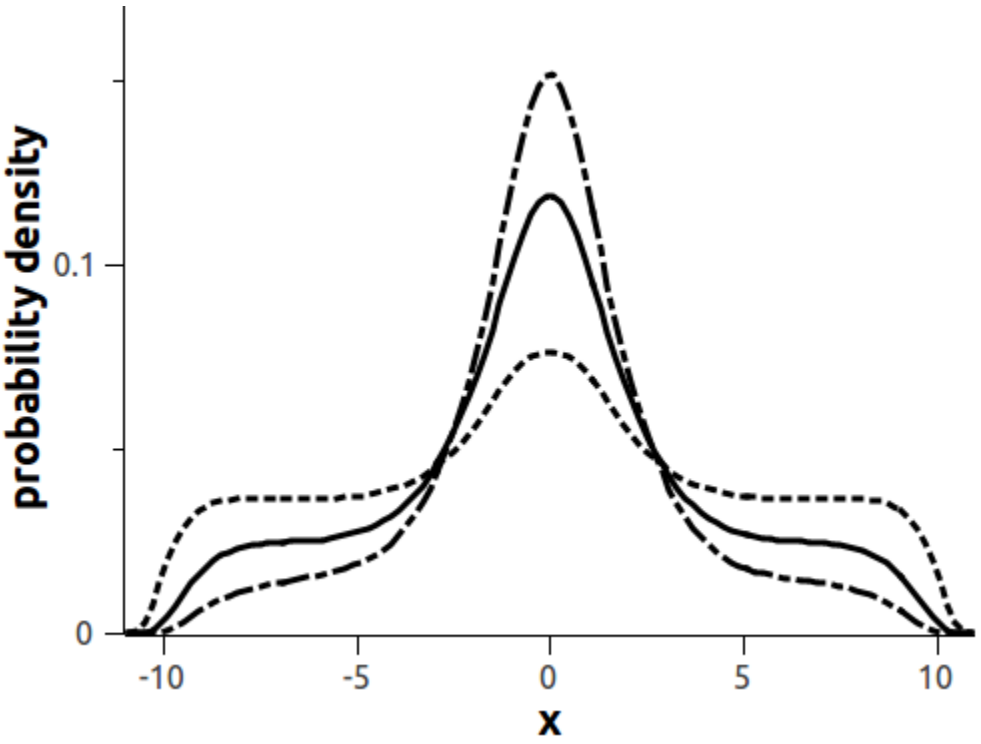

Figure 4.17: Spatial distribution of different length polymers in the wide chamber at the same shear rate by applying an acceleration g = 0.02. Dashed curve: 5-spring chain, solid curve: 10-spring chain, dot-dashed curve: 15-spring chain.

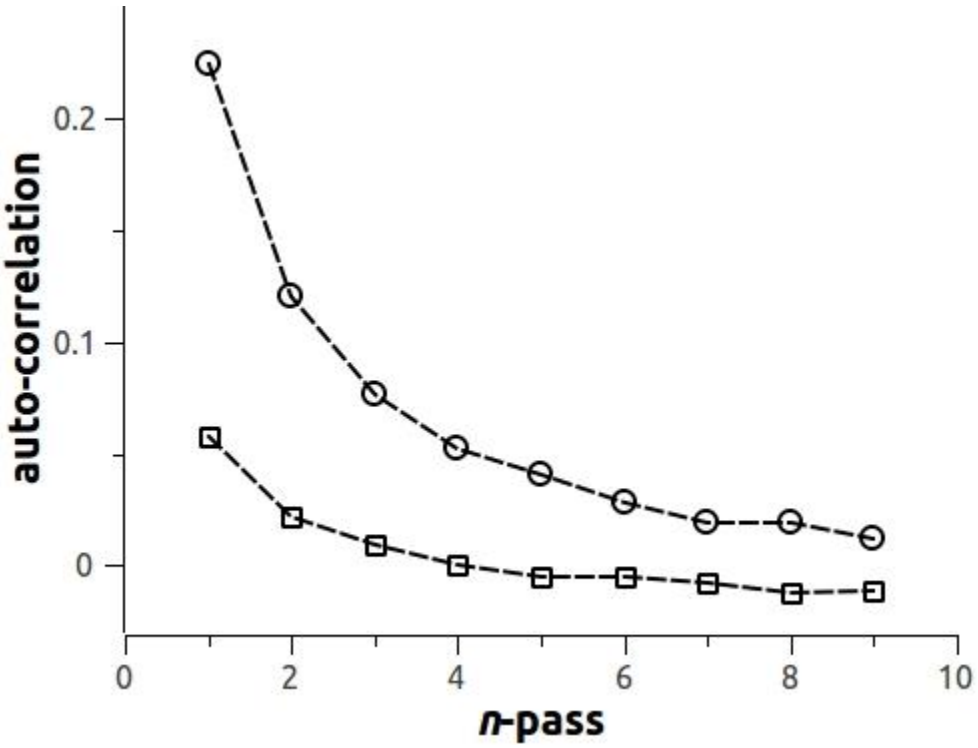

Figure 4.18: Auto-correlation of the *n*-pass residence time for a 10-spring polymer chain. Squares: Wi = 2.5; circles: Wi = 12. The statistical error is about the size of the symbols.

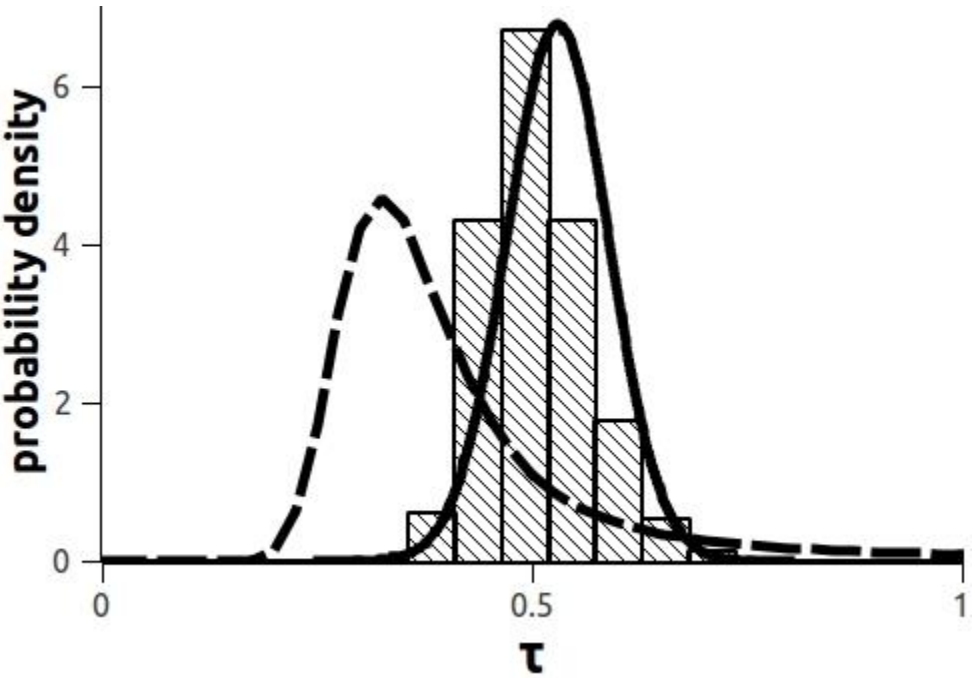

Figure 4.19: Histogram: residence time distribution of a 100-step contraction channel. Solid curve: Gaussian distribution predicted by the central limit theorem. Dashed curve: the distribution of 1-pass residence times.

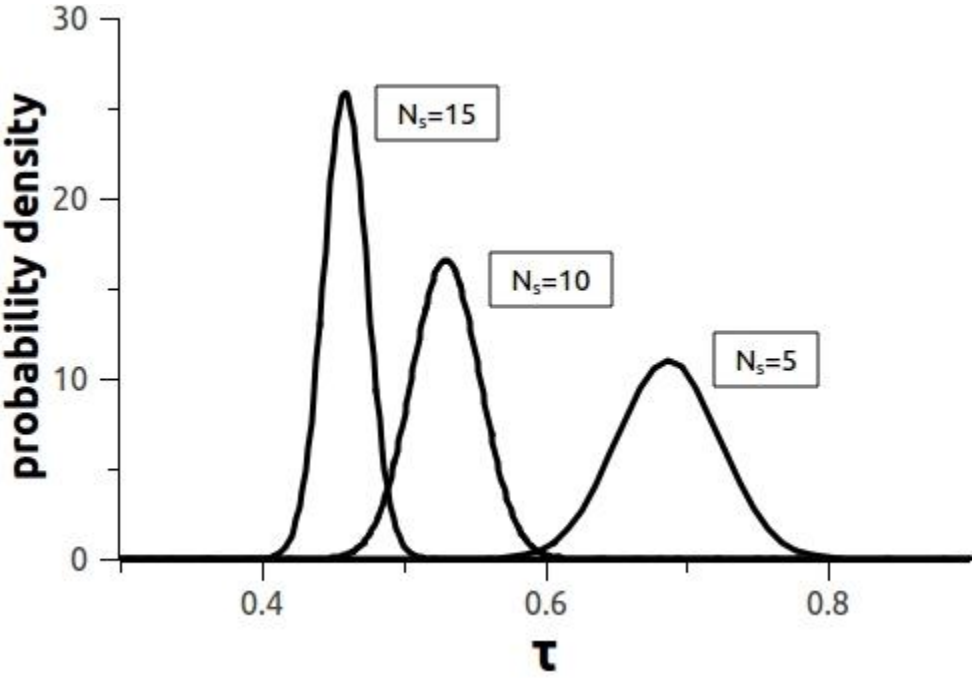

Figure 4.20: Residence time distributions of polymer chains of different lengths in a 600-step contraction channel as predicted by the central limit theorem for an acceleration $g = 0.02$.

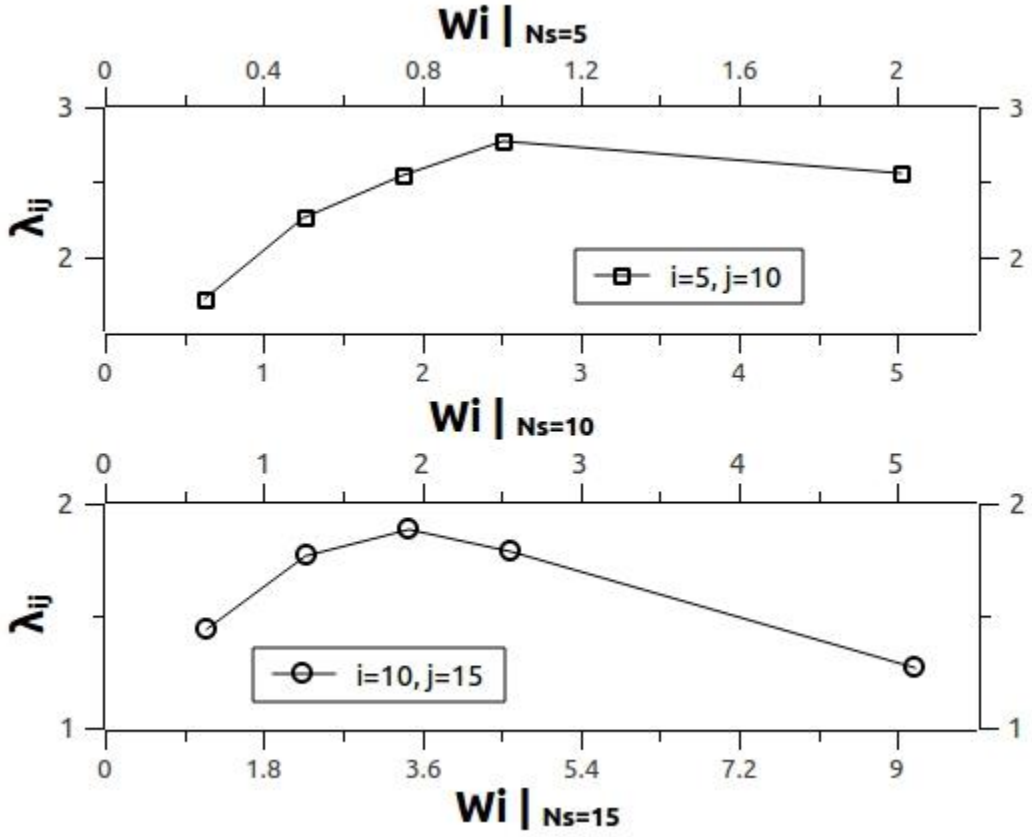

Figure 4.21: Dependence of the separation efficiency dependence on narrow-channel shear rate in a 600-step contraction channel. For the points from left to right, the shear rate is adjusted by applying accelerations g = 0.005, 0.01, 0.015, 0.02, 0.04. The shear rates are converted to Weissenberg numbers for each of the chain lengths, as shown, by multiplying by the relaxation time corresponding to that chain. Top: separation between 5-spring chains and 10-spring chains; bottom: separation between 10-spring chains and 15-spring chains.

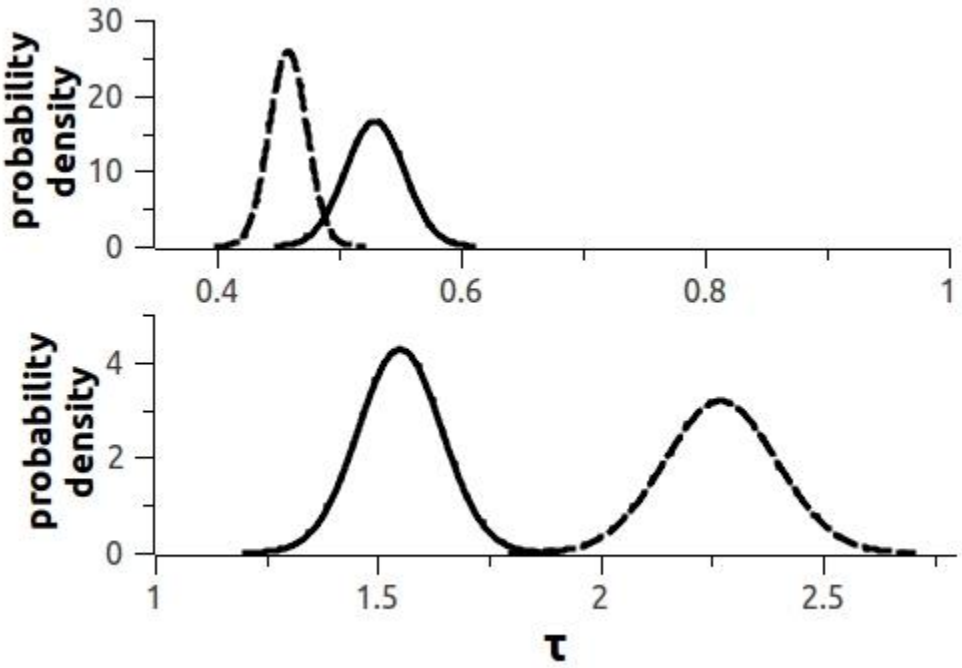

Figure 4.22: Residence time distributions of different length polymer chains in a 600-step contraction channel as predicted by the central limit theorem under different accelerations. Solid curves: 10-spring chain, dashed curves: 15-spring chain. Top: $g = 0.02$ for which $\mathrm{Wi}\big|_{N_s=10} = 2.5$, $\mathrm{Wi}\big|_{N_s=15} = 4.6$; bottom: $g = 2\times10^{-4}$ for which $\mathrm{Wi}\big|_{N_s=10} = 0.025$, $\mathrm{Wi}\big|_{N_s=15} = 0.046$.

Table 4.1. Comparison of the mean μ and standard deviation σ of the normalized residence time distribution from SRD simulations with different HI strengths to BD simulations without HI with flow field from SRD.

	10-spring chain		28-spring chain	
	SRD w/ h^*=0.16	BD	SRD w/ h^*=0.27	BD
μ	0.51	0.53	0.44	0.47
σ	0.47	0.50	0.40	0.44

- The ratio $w/R_g = 2$, where w is the width of the narrow channel.
- The statistical errors are 0 through the 2nd decimal place.

Table 4.2. Comparison of the mean μ and standard deviation σ of the normalized residence time distribution from SRD simulations at h^*=0.16 to different BD simulations without HI for 10-spring chains

	μ	σ
SRD	0.51	0.47
BD w/ flow field from SRD	0.53	0.50
BD w/ flow field from FEM w/ a=1	0.50	0.49
BD w/ flow field from FEM w/ a=0.2	0.49	0.48
BD w/ flow field from FEM w/ a=0.2 and modified boundary for polymer beads	0.53	0.58

- a is the grid size for the flow field.
- The statistical errors are 0 through the 2nd decimal.

Table 4.3. Values of ξ obtained by fitting dispersion coefficients from BD simulations to Eq. (4.4.2.1) for different length polymers at two values of $\varepsilon = R_g / w$

	$N_s = 0$	$N_s = 5$	$N_s = 10$	$N_s = 15$	Theory
$\varepsilon = 0$	216				210
$\varepsilon = 1/8$		689	875	921	1142
$\varepsilon = 1/2$		5083	11064	14645	∞

- The last column is from the analytical theory, given by Eq. (4.4.2.2).

Chapter 5

Stochastic Rotation Dynamics Simulations of Polymer Solution

In this chapter, Stochastic rotational dynamics (SRD) are used to simulate the dynamics of polymers in dilute and non-dilute, but unentangled solutions both at equilibrium and under flow in confined geometries. We first propose a way to calculate the viscosity of the polymer solution, and find the result agrees well with that from fitting the parabolic flow profile of the Poiseuille flow of the polymer solution at different polymer concentration. Then the simulation of polymer solution with different concentration in a pressure-driven slit channel is carried out to see SRD captures the hydrodynamic interaction (HI) between the polymer and the wall, as well as the screening of HI with increased polymer concentration is captured by SRD. The screening of HI thins the depletion layer at the wall in slit flow as the polymer concentration increases, consistent with previous experimental work and Brownian dynamics simulations with HI [Hernández-Ortiz *et al*., *Physics Review Letters* **98**, 140602 (2007)]. Finally, we use SRD to simulate how semi-dilute polymer concentration modifies the flow and induces polymer migration in a periodic pressure-driven planar contraction channel. The results show that the SRD method is very well suited to account for flow-induced polymer deformation, hydrodynamic interactions both within the chains and between the chain and the wall, polymer-induced changes in the flow field, and flow-induced polymer migration due both to hydrodynamic interactions and due to streamline-curvature induced migration.

5.1.Viscosity of the polymer solution

When polymers are mixed with solvent, the polymeric stresses contribute to the total stress of the solution and change the viscosity. In this section, we describe a method of calculating the viscosity of the SRD polymer solution, and determine whether SRD correctly captures the influence of the polymer on the fluid viscosity in a concentration regime where entanglement effects remain negligible.

To simulate the polymer solution, we simply add multiple polymer chains in the SRD solvent. And the polymer concentration (number density of polymer chains) is reported relative to the overlap concentration, at which the chains are concentrated enough so that a random equilibrium coil of raduis R_g begins to overlap with nearby coils. This concentration, denoted c^*, is defined as $c^* = \left(\frac{4\pi}{3} R_g^3 \right)^{-1}$ [Larson (1999)].

In this chapter, for the spring, we use the wormlike spring law as in Eq. (3.4.2) in Section 3.4.3, which is commonly used for DNA [Marko and Siggia (1995)]. We obtain specific values for these parameters by mapping the values in microns from the BD bead-spring model of Jendrejack *et al.* (2002) into SRD length units a = 1 (a is the size of the collision cell.), as discussed in Section 3.4.3. In this chapter, the SRD parameters are chosen to be $\rho = 5, \Delta t = 0.05, \alpha = 150^\circ$, and mass of the polymer bead M = 2.5 to minimize inertial the as discussed in Chapter 3. With these parameters, the spring parameters $\{b_K, L_s\}$ are yielded to be {0.380, 7.534} in SRD units, corresponding to {0.106μm, 2.1μm} in Jendrejack *et al*. (2002). For simplicity, we do not consider the excluded volume among the beads; thus the polymer and polymer beads can freely penetrate each other. And without excluded volume, the polymer radius of gyration R_g at equilibrium is 2.1.

The viscosity of the polymer solution can be attributed to the momentum transfer from both the *streaming* and *collision* steps, as well as from the spring forces. That is $\eta = \eta_{\text{kin}} + \eta_{\text{col}} + \eta_{\text{spring}}$. The first two parts, η_{kin} and η_{col}, include the contributions from both the solvent beads and the polymer beads. They can be calculated analytically as the viscosity of a mixture of two SRD fluids. One fluid consists of solvent beads with mass *m*, and the other of polymer beads with mass *M*. Thus the resulting viscosity is

$$\eta_{\text{kin/col}} = \eta^{(\text{s})}_{\text{kin/col}} + \beta\eta^{(\text{p})}_{\text{kin/col}} \tag{5.1.1}$$

where $\eta^{(\text{s})}$ and $\eta^{(\text{p})}$ are calculated from Eqs. (2.2.1.2-2.2.1.3) listed in Chapter 2 with the bead's mass *m* and *M* respectively, and the rest parameters, such as the number density ρ and rotation angle α, being the same. Here β is mixing ratio, i.e. the ratio of the number of polymer beads to the number of the solvent beads. In our simulations, the external force is only applied to the solvent beads; otherwise Eq. (5.1.1) should be the average of $\eta^{(\text{s})}$ and $\eta^{(\text{p})}$ weighted by their corresponding numbers of beads. This is confirmed by our simulations when the external force is applied on both the solvent and the polymer beads to measure the viscosity. The circles in Fig. 5.1 are the viscosities from fitting the parabolic flow profile, and the solid line is from Eq. (5.1.1), showing good agreement between the two.

To calculate the viscosity due to the spring force, η_{spring}, we apply the Green-Kubo formula [Lee and Kremer (2009)]. The stress due to the spring force at time *t* is first calculated as $\sigma_{ij}(t) = \frac{1}{V}\sum_{m=1}^{N_{\text{p}}}\sum_{n=1}^{N_{\text{s}}} F_i^{(mn)} F_j^{(mn)}$, where $F_i^{(mn)}$ is the *i*-th component of the spring force from the

n-th spring of the *m*-th polymer chain. Then the stress modulus from the auto-correlation of the stress tensor is calculated as $G_{ij}(t)=\frac{V}{k_{\mathrm{B}}T}\left\langle\sigma_{ij}(t)\sigma_{ij}(0)\right\rangle$. Finally η_{spring} is,

$$\eta_{\mathrm{spring}}=\int_0^\infty G(t)\,\mathrm{d}t \tag{2.3}$$

where $G(t)=\frac{1}{3}\left(G_{xy}(t)+G_{xz}(t)+G_{yz}(t)\right)$.

For comparison, we obtain η_{spring} via a second way. We simulate Poiseuille flow of the polymer solution between two parallel plates, keeping the Weissenberg number, Wi, as low as 0.5 to prevent the polymer from stretching; otherwise the flow profile will deviate from the parabolic [Hernández-Ortiz *et al*. (2007)]. Here $\mathrm{Wi}=\dot{\gamma}\tau$, with $\dot{\gamma}$ the shear rate, defined here for the Poiseuille flow in the slit as $\dot{\gamma}=gw/4\nu$ and τ is the polymer's stress relaxation time. Then η_{spring} is obtained by subtracting the kinetic and collision contributions to the viscosity calculated by Eq. (5.1.1) from the viscosity obtained by fitting the parabolic flow profile. Note due to the size-induced depletion from the wall, the polymer concentration is close to zero inside the depletion zone, resulting in a lower viscosity than that in the bulk. And thus the Poiseuille flow profile outside the polymer's depletion zone is actually a parabolic profile with a "slippery" boundary condition, where the "slippery" boundaries can be assumed to be located at a distance R_{g} away from the wall. Such slipping becomes stronger as the polymer concentration increases. Therefore for the fitting, we exclude the flow profile within the depletion zone of size R_{g}, and fit the remainder of the profile to $A(x-R_{\mathrm{g}})(w-R_{\mathrm{g}}-x)+B$, where L is the channel width and the two parallel plates are located at 0 and w along the x-direction; A and B are fitting parameters, A is related to the kinematic viscosity ν by $A=\frac{g}{\nu}$, and B is the slip velocity at the "slippery"

boundary. Due to the "slippery" boundary, the viscosity obtained from fitting the parabolic profile is approximate. Nevertheless, Figure 5.2 shows that the values (circles) calculated from this method agree well with those from the Green-Kubo calculation, which is shown by the error bars. In the Green-Kubo calculation, we first set the simulation box the same size as that in the Poiseille flow simulation while replace the walls with periodic boundary conditions. Next, to take into account the influence of the depletion zone on the polymer concentration, we set the width of simulation box $2R_g$ narrower. Thus we get a higher polymer concentration and higher viscosity. The Green-Kubo calculations based on these two different simulation box sizes give the error bars shown in the figure.

5.2.Screening of Hydrodynamic interaction (HI)

Polymer dynamics in a confined geometry have been widely studied, where one interesting finding is the migration of polymers away from the wall due to the HI between the polymer and the wall. Different mesoscopic simulations have been performed to study this migration in a square or slit micro-channel: Brownian dynamics (BD) simualtions by Jendrejack *et al*. (2004) in a square channel, Lattice-Boltzman simualtions by Usta *et al*. (2005) in a slit channel, SRD simulations by Watari *et al*. (2007) in a slit channel and by Cannavacciuolo *et al*. (2008) in a square channel. However, all the above studies were for the case of a single chain. Fang and Larson (2007) experimentally confirmed that a DNA polymer migrates away from a surface due to the HI between the DNA and the wall, and found that this migration is weakened with increasing polymer concentration because of the screening of the HI. Meanwhile Hernández-Ortiz *et al*. (2007) also demonstrated such an effect using BD simulations. Here we revisit this problem and demostrate that SRD also accurately captures the HI screening effect produced by an increase of the polymer concentration.

We performed our simulations in a slit channel with width w = 7.2R_g, and the channel length along the flow direction and the channel depth are chosen to be 25R_g and 10R_g, respectively, to avoid the self-interactions of periodic images. Figure 5.3 shows the normalized steady-state center-of-mass distribution of the polymer, $P_c(x)$ ($\int_0^w P_c(x)\mathrm{d}x = 1$, the confinement is along the x-direction) at different Wi values with polymer concentration c = 0.1c^*. Because of the symmetry with respect to the channel center, only half of the distribution is plotted. The central dip is due to gradients in diffusivity, which results in a migration towards the walls [Butler *et al.* (2007)]. As Wi increases, the migration due to the diffusivity gradients gets stronger, and is balanced by migration away from the wall due to the HI between the polymer and wall. Therefore the width of the wall depletion layer saturates at high Wi as shown in Figure 5.3 Such a saturation was not observed in the work of Jendrejack *et al*. (2004) and of Cannavacciuolo *et al*. (2008), presumably because in those two studies, the polymer was confined in a square channel. This stronger confinement than in the slit channel strengthens the migration away from the wall, which may overwhelm the migration from the center, or possibly the saturation in the square channel happens at a even higher Wi. Resolving this difference is left for future investigation.

Figure 5.4 shows the influence of the polymer concentration on the polymer density profile. The HI between the polymer and wall is expected to be screened as the polymer concentration increases, and in fact the thickness of the wall depletion layer decreases with increased concentration as shown in Figure 5.4 When the concentration increases up to 1.3c^*, the thickness of the depletion zone decreases to below that at equilibrium. The reduction below the equilibrium (no-flow) thickness occurs because without HI, flow decreases the depletion zone due to the polymer stretching and alignment. This is shown in the inset using BD simulations w/o HI [Chopra and Larson (2002)], where there is no thickening of the wall depletion zone due

to hydrodynamic interactions with the wall, and so only the thinning of the depletion zone from chain stretch remains. For SRD simulations, which include not only HI, but also its screening at $c = 1.3c^*$, the wall depletion thickness at Wi = 81 is not as thin as is obtained by BD simulations at Wi = 81 in the absence of HI (compare circles to solid line in inset to Fig. 8), so the HI is not completely screened at $c = 1.3c^*$, possibly because the polymer concentration near the wall is too low to produce much screening.

5.3.Contraction flow of the polymer solution

It is known that above the very dilute regime, the influence of the polymeric stresses from the stretched polymers on the fluid will change the flow field. In a contraction flow, we show in Chapter 4 that streamline curvature induces polymer to migrate toward centerline of the channel, resulting in non-uniformity of the polymer density within the channel. While the effect of polymer on the flow field might be captured by a finite element simulation using an appropriate constitutive equation, the added complexity of the flow-induced polymer migration couples the fluid flow and mass transfer together, making the problem a very challenging one for continuum-level analysis. In addition, the polymer molecules in our simulations are comparable in size to the geometry, so that concentration and stress gradients have length scales comparable to the polymer molecules, making a standard continuum analysis very difficult indeed. Fortunately, mesoscopic methods, such as SRD, are able to capture all of these effects in a relatively simple algorithm.

One issue with using SRD to simulate non-dilute polymer solutions, however, is that, as the polymer concentration increases, the number of the polymer beads increases and can become comparable to the number of the solvent beads, in which case it becomes doubtful that the solvent beads can really represent the fluid hydrodynamics properly. Our simulations show that

at $4.7c^*$ (based on the volume of the wide chamber), at which the ratio of the number of polymer to solvent beads reaches $\beta = 0.28$, the eddies shown in Fig. 5 are wiped out. However, if we double the number of the solvent beads, the eddies are recovered. In principle, the exact number of solvent beads should not drastically affect the flow, and so we infer that, to avoid artifacts, the polymer concentration below $2.4c^*$.

The geometry of the contraction channel is the same as discussed in Chapter 2 (Figure 2.4) and Chapter 4 (Figure 4.1). To show more clearly how polymers change the contraction flow field, we increase the length of the wide chamber from 12 to 15. As shown in Figure 5.5, in this longer geometry, the big eddies, shown in Figure 2.6-2.7 in Chapter 2, break into smaller eddies in each of the four corners, according to the SRD simulation for pure solvent. However, for the polymer solution with $2.0c^*$, and Weissenberg number, Wi = 2, based on the shear rate in the narrow channel, we can see in Figure 5.6, that the polymers suppress the eddies in the upper corners, while the eddies in the lower corners remain.

In Chapter 4, we study the single-chain migration in the contraction flow and found that streamline-curvature-induced migration dominates the polymer concentration field, while HI has a negligible effect on polymer migration. Here, we wish to examine the influence of the polymer concentration on the migration.

Figure 5.8 shows the residence time distribution (RTD) of the10-spring chains. We can see that the RTD at $2.4c^*$ has a fatter tail than that at $0.6c^*$. To understand this change, first we note that when the polymer concentration increases from $0.6c^*$ to $2.4c^*$, Wi reduces from 3.0 to 2.0. To assess the influence from the Wi reduction, we reduce the shear rate at $0.6c^*$ to decrease Wi to 2.0. We can see from Figure 5.8 that the decrease in Wi significantly fattens the tail of the RTD from that in the red curve to that in the green curve. The small remaining difference between the

green and black curves is presumably owed to the modification in the flow field produced by the polymers. Therefore the influence of the polymer concentration on the polymer migration can predominantly be attributed to the Wi reduction, which controls the streamline-curvature-induced migration. We can see from Figure 5.9, with the same Wi, the polymer density distribution at $0.6c^*$ and $2.4c^*$ almost overlap, while the modification of flow field due to the polymer concentration makes tiny difference. The findings imply that the streamline-curvature-induced migration is the dominant mechanism in the polymer migration in the contraction flow at Wi<10.

Next, we replace a fraction of the 10-spring chains with 5-spring and 15-spring chains, with $N_{\mathrm{p,i}}R_{\mathrm{g,i}}^3$ the same for all three of the chains, where $N_{\mathrm{p,i}}$ is the number of polymer chains of type i, and $R_{\mathrm{g,i}}$ is the radius of gyration of such chains. The result is a mixture of polymers in solution whose number of polymer chains per unit volume is the same as the original polymer solution consisting of only 10-spring chains. We apply an acceleration g = 0.02. Using the central limit theorem as described in Chapter 4, we predict the RTD of the different length polymers in a 600-step contraction channel. Figure 5.10 shows that at both $c = 0.6c^*$ and $c = 2.4c^*$, 5-spring and 10-spring chains are very well separated, while 10-spring and 15-spring chains have a better separation when the polymer contraction increases from $0.6c^*$ to $2.4c^*$. If we look at the efficiency of separation of *i*-spring chains from *j*-spring chains in an *N*-step contraction channel , $\lambda_{i,j}(N)$, as defined in Eq. (4.5.1) in Chapter 4, we find that $\lambda_{10,15}(600)$ increases from 2.2 to 2.4, as the concentration increases from $c = 0.6c^*$ and $c = 2.4c^*$. Note in Chapter 4, we show that the best separation due to streamline-curvature-induced migration is achieved at Wi around 2. Here as the polymer concentration increase from $0.6c^*$ to $2.4c^*$, Wi of the 10-spring chain is reduced

from 3.0 to 2.0, while 10-spring and 15-spring chains achieve a better separation at the higher concentration.

5.4. Summary

In this chapter, we studied the SRD simulations of polymer dynamics in dilute and non-dilute, but unentangled solutions both at equilibrium and under flow in two confined geometries: 1) a simple slit channel; and 2) a periodic pressure-driven contraction channel with the width of its narrow region comparable in size to the polymer's radius of gyration.

At equilibrium, we propose a way to calculate the viscosity of the polymer solution. The viscosity of the SRD polymer solution attributes to the momentum transfer from both the *streaming* and *collision* steps, as well as from the spring forces. That is $\eta = \eta_{\text{kin}} + \eta_{\text{col}} + \eta_{\text{spring}}$. For the first two parts, we show that they can be calculated analytically as the viscosity of a mixture of two SRD fluids. One fluid consists of solvent beads with mass *m*, and the other of polymer beads with mass *M*. For the contribution for the spring, we use Green Kubo formula to calculate the spring contribution to the viscosity. And we validate this way to calculate the viscosity by comparing with that from fitting the parabolic slit Poiseuille flow profile.

In the slit Poiseuille flow, we demonstrate the thickness of the depletion layer decreases as increase of the polymer concentration, which is consistent with what was reported in the experiment [Fang and Larson (2007)]. It is due to the screening of HI between the wall and the polymer. And as the polymer concentration further increases, the thickness of the depletion layer can be less than that at equilibrium due to the polymer stretching and alignment near the wall.

In the contraction flow, we show that the influence of polymer concentration on the polymer migration can be from the modification of the flow field and the Weissenberg number Wi

reduction, while the latter dominates, implying the streamline-curvature-induced migration is the dominant mechanism for the polymer migration in our contraction flow at Wi<10.

References

Butler, J.E., O.B. Usta, R. Kekre and A.J.C. Ladd, "Kinetic theory of a confined polymer driven by an external force and pressure-driven flow," *Physics of Fluids* **19**, 113101 (2007).

Cannavacciuolo, L., R.G. Winkler and G. Gompper, "Mesoscale simulations of polymer dynamics in microchannel flows," *Europhysics Letters* **83**, 34007 (2008).

Chopra M. and R.G. Larson, "Brownian dynamics simulations of isolated polymer molecules in shear flow near adsorbing and nonadsorbing surfaces," *Journal of Rheology* **46**, 831-862 (2002).

Fang, L. and R.G. Larson, "Concentration dependence of shear-induced polymer migration in DNA solutions near a surface," *Macromolecules* **40**, 8784-8787 (2007).

Hernández-Ortiz, J.P., J.J. de Pablo and M.D. Graham, "Fast computation of many-particle hydrodynamic and electrostatic interactions in a confined geometry," *Physics Review Letters* **98**, 140602 (2007).

Jendrejack, R. M., J. J. de Pablo and M. D. Graham, "Stochastic simulations of DNA in flow: Dynamics and the effects of hydrodynamic interactions," *Journal of Chemical Phycics* **116**, 7752(8) (2002).

Jendrejack, R. M., D.C. Schwartz, J. J. de Pablo and M. D. Graham, "Shear-induced migration in flowing polymer solution: simulation of long-chain DNA in microchannels", *Journal of Chemical Phycics* **120**, 2513 (2004).

Larson, R.G., "The structure and rheology of complex fluids," (Oxford University Press, New York, 1999).

Lee, W. B. and K. Kremer, "Entangled polymer melts: relation between plateau modulus and stress autocorrelation function," *Macromolecules* **42**, 6270-6276 (2009).

Marko, J. F. and E. D. Siggia, "Stretching DNA," *Macromolecules* **28**, 8759-8770 (1995).

Usta, O.B., A.J.C. Ladd, and J.E. Butler, "Lattice-Boltzmann simulations of the dynamics of polymer solutions in periodic and confined geometries", *Journal of Chemical Physics,* **122**, 094902 (2005).

Watari, N., M. Makino, N. Kikuchi, R. G. Larson and M. Doi, “Simulation of DNA motion in a microchannel using stochastic rotation dynamics,” *Journal of Chemical Physics* **126**, 094902(7) (2007).

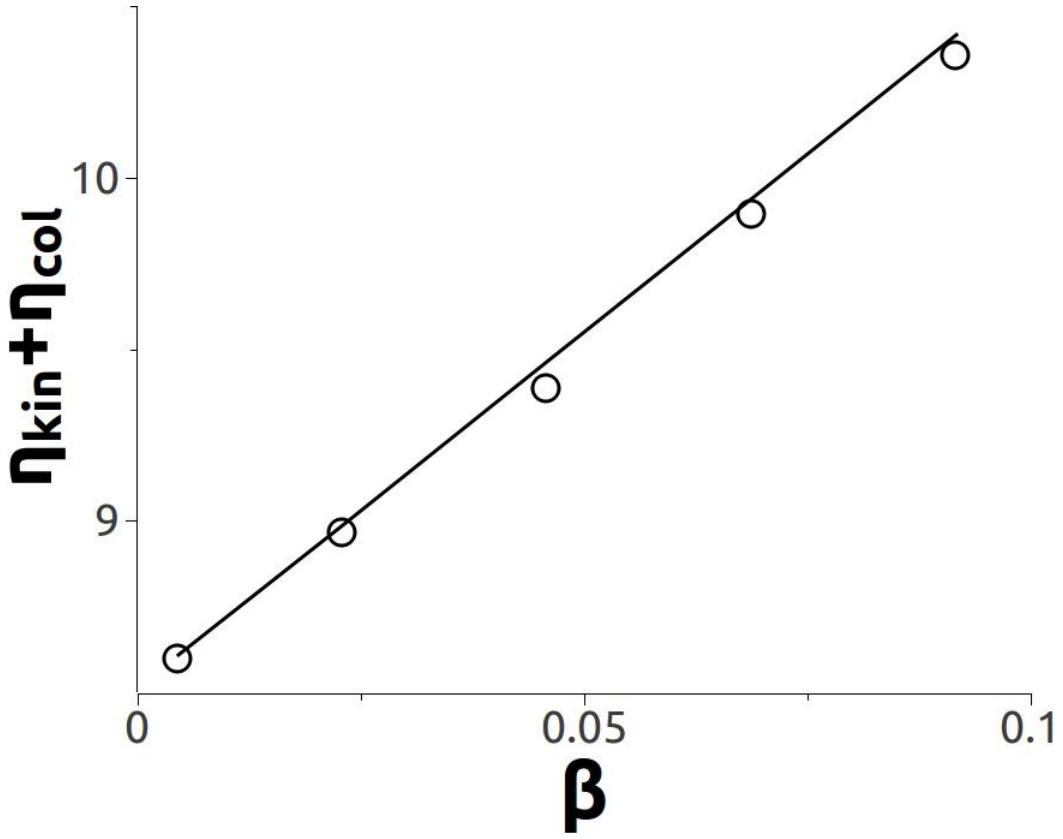

Figure 5.1: the viscosity of a mixture of solvent and polymer beads (without springs connecting them) versus the mixing ratio. The solid line is from Eq. (5.1.1), and the circles are from fitting the parabolic Poiseuille flow profile of an SRD simulation.

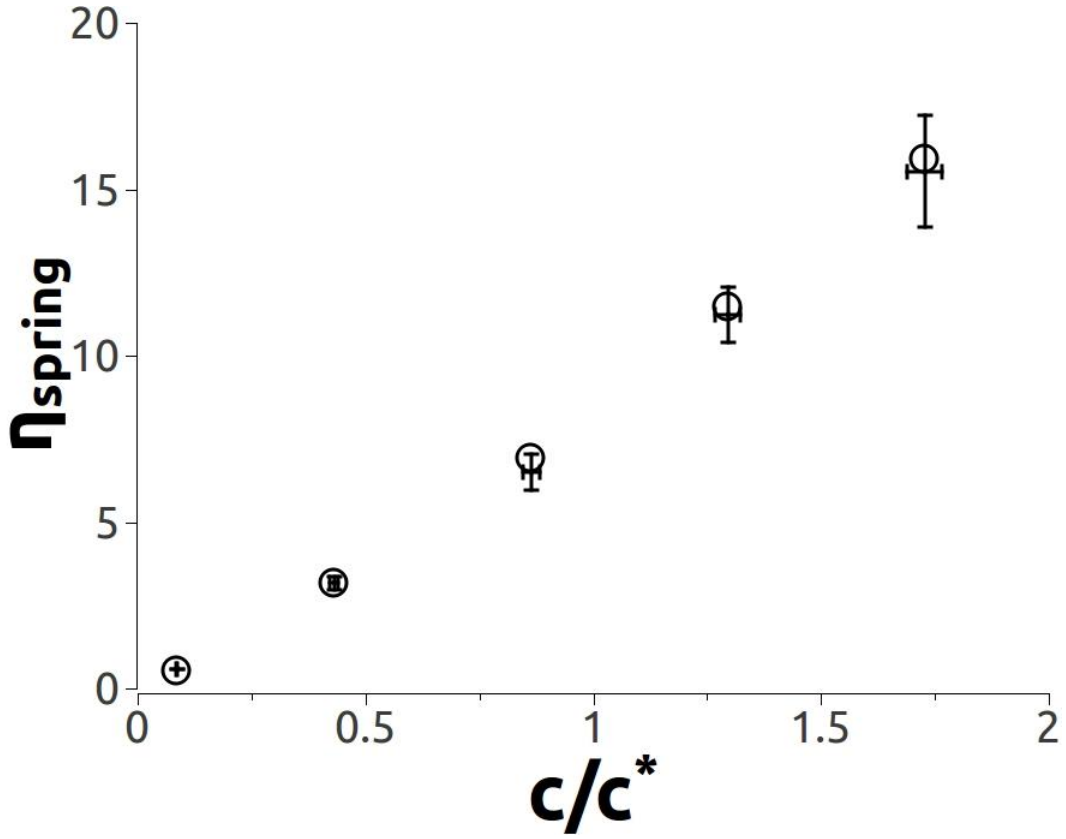

Figure 5.2: The contribution to the viscosity of the polymer solution from the spring forces as a function of the polymer concentration normalized by the overlap concentration $c^* = \left(\frac{4\pi}{3} R_g^3\right)^{-1}$. The error bars are from a Green-Kubo calculation, and the circles are from fitting the parabolic Poiseuille flow profile.

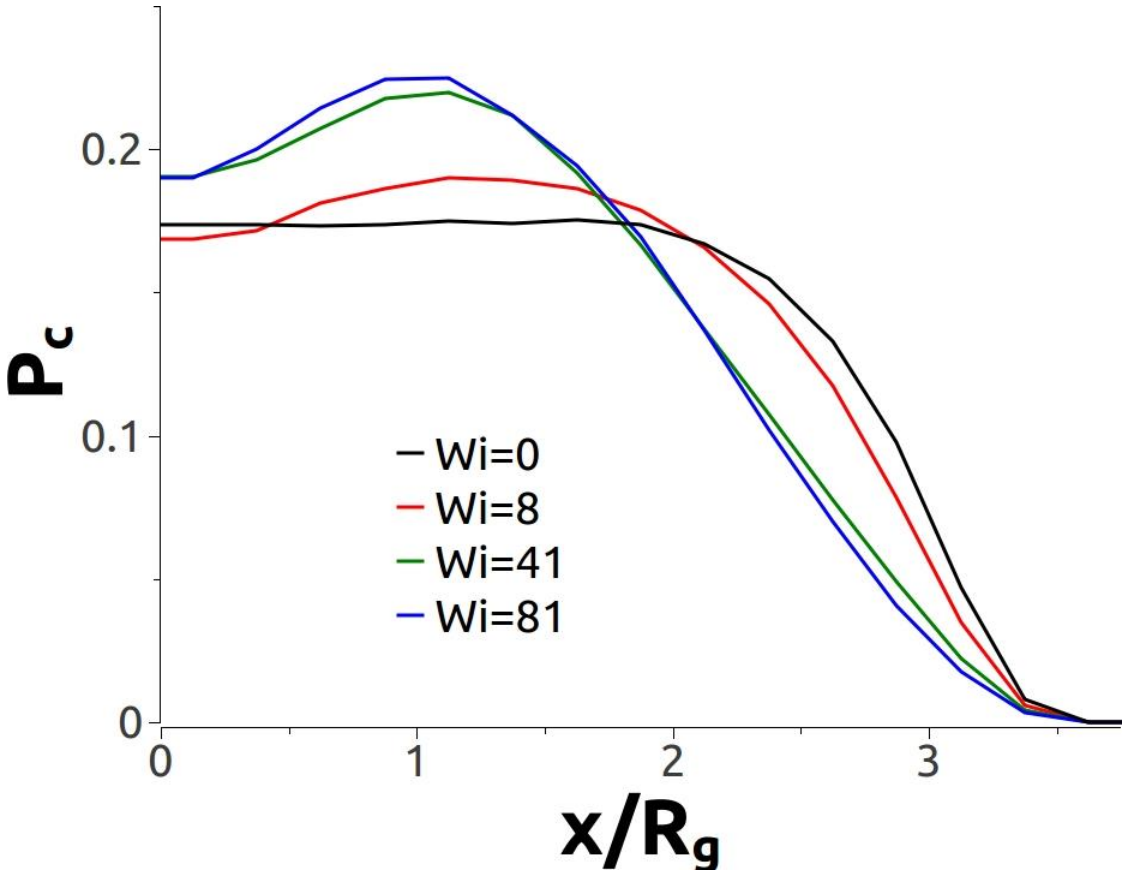

Figure 5.3: Normalized steady-state center-of-mass distribution $P_c(x)$ for different Wi at a polymer concentration of $0.1c^*$.

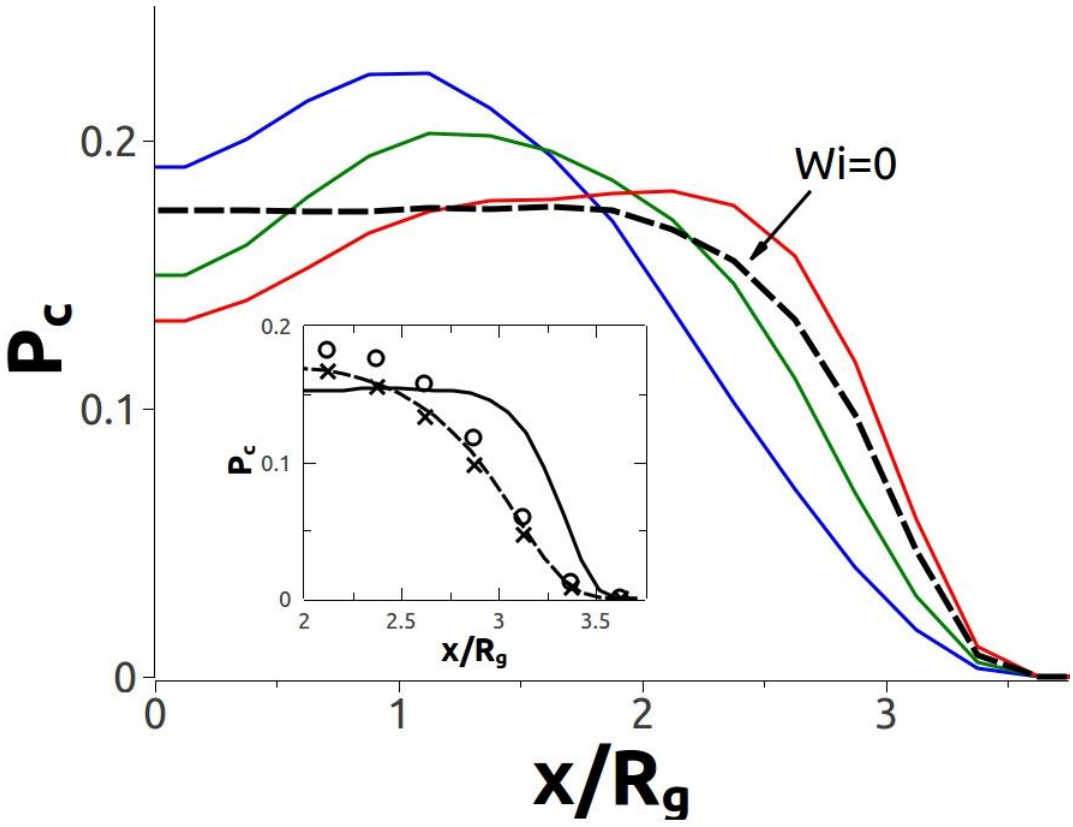

Figure 5.4: Normalized steady-state center-of-mass distribution $P_c(x)$ for polymer concentration at Wi=81 and for equilibrium (Wi=0). Blue curve: $c=0.1c^*$, green curve: $c=0.4c^*$, red curve: $c=1.3c^*$. Inset: comparison with BD simulations w/o HI. Dashed curve: BD at Wi=0, solid curve: BD at Wi=81, crosses: SRD at Wi=0, circles: SRD at Wi=81 and $c=1.3c^*$.

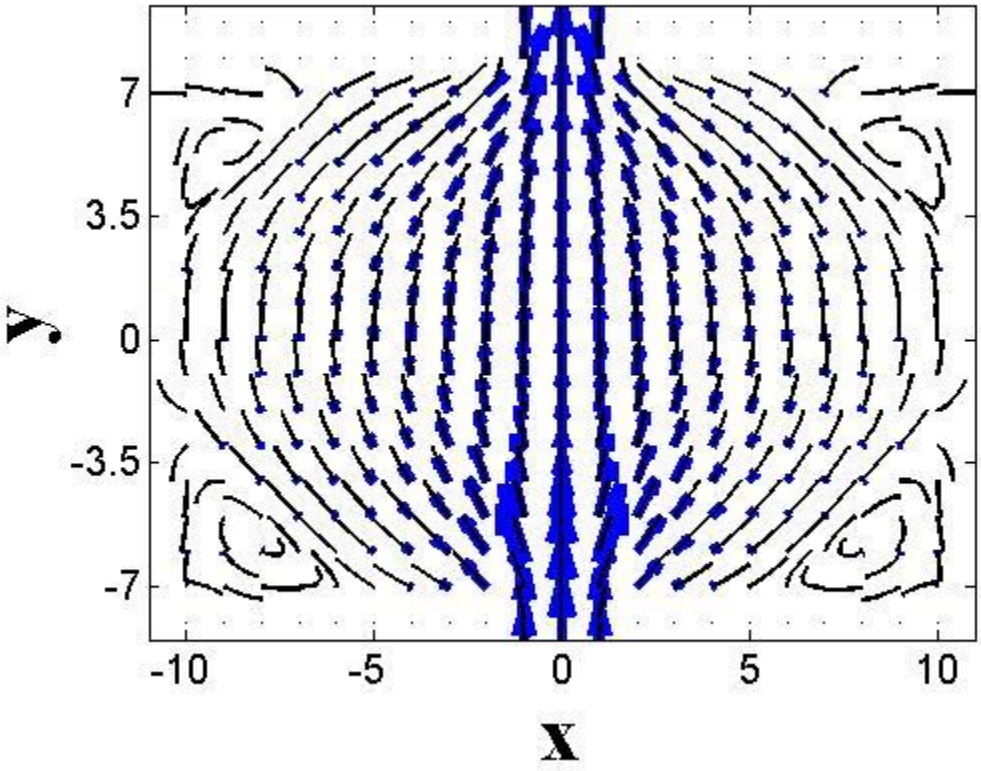

Figure 5.6: The flow field(arrows) and streamlines(black curves) in the wide chamber of the contraction channel from SRD simulation of the pure solvent at Re = 0.06 and Ma = 0.02.

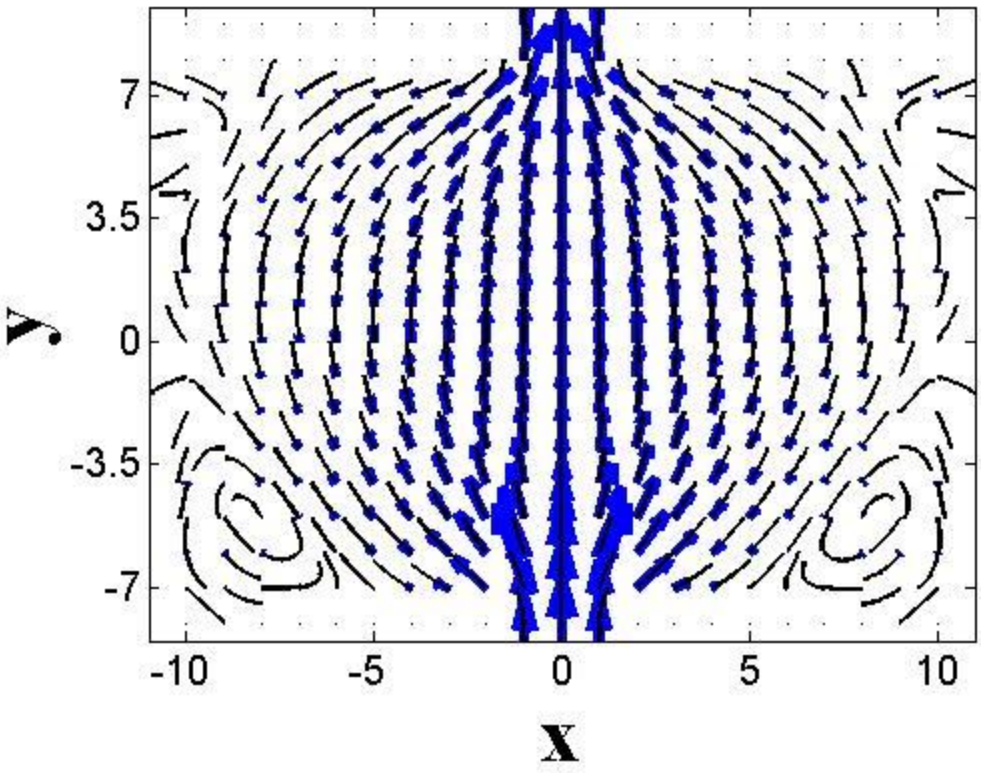

Figure 5.7: The same as Figure 5.6, expect it is from simulating the polymer solution with $2.0c^*$, and Wi = 2.

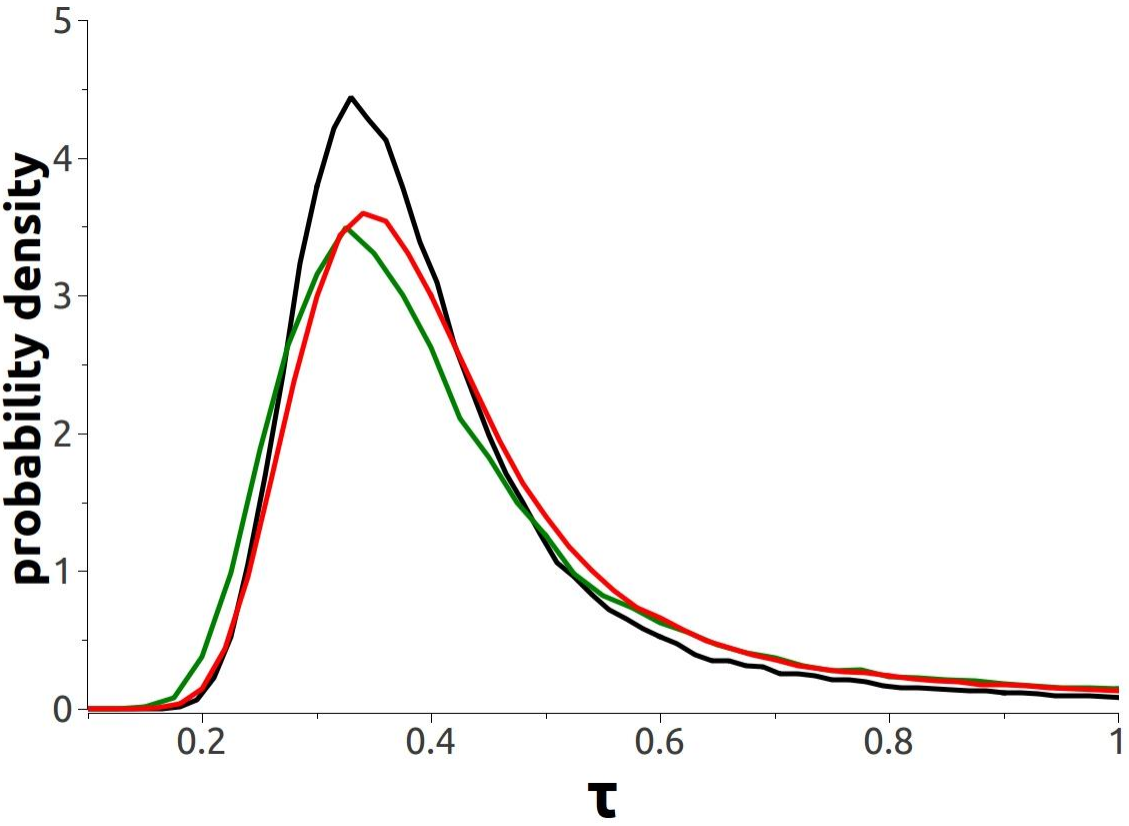

Figure 5.8: One-pass residence time distribution of 10-spring chains at different concentrations. Black curve: $c = 2.4c^*$, Wi = 2.0; Green curve: $c = 0.6c^*$, Wi = 2.0; Red curve: $c = 0.6c^*$, Wi = 3.0.

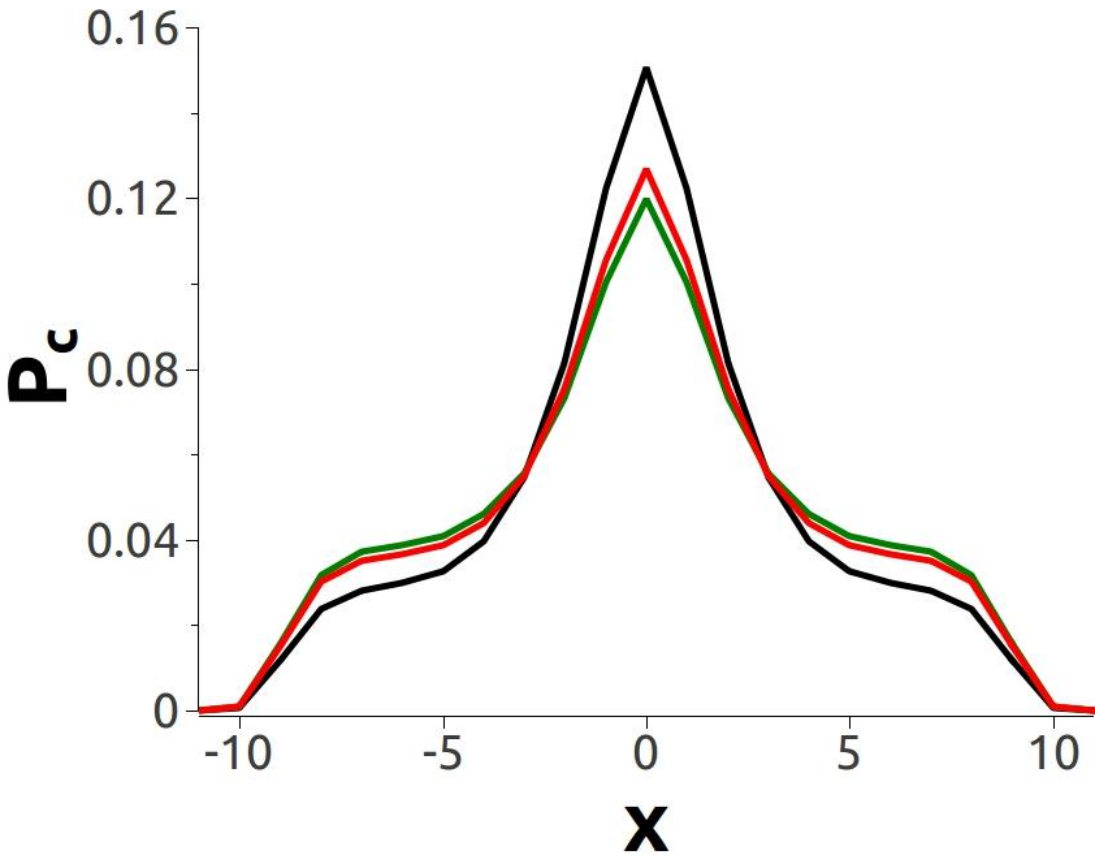

Figure 5.9: Normalized steady-state center-of-mass distribution $P_c(x)$ of 10-spring chains at different concentrations. Black curve: $c = 2.4c^*$, Wi = 2.0; Green curve: $c = 0.6c^*$, Wi = 2.0; Red curve: $c = 0.6c^*$, Wi = 3.0.

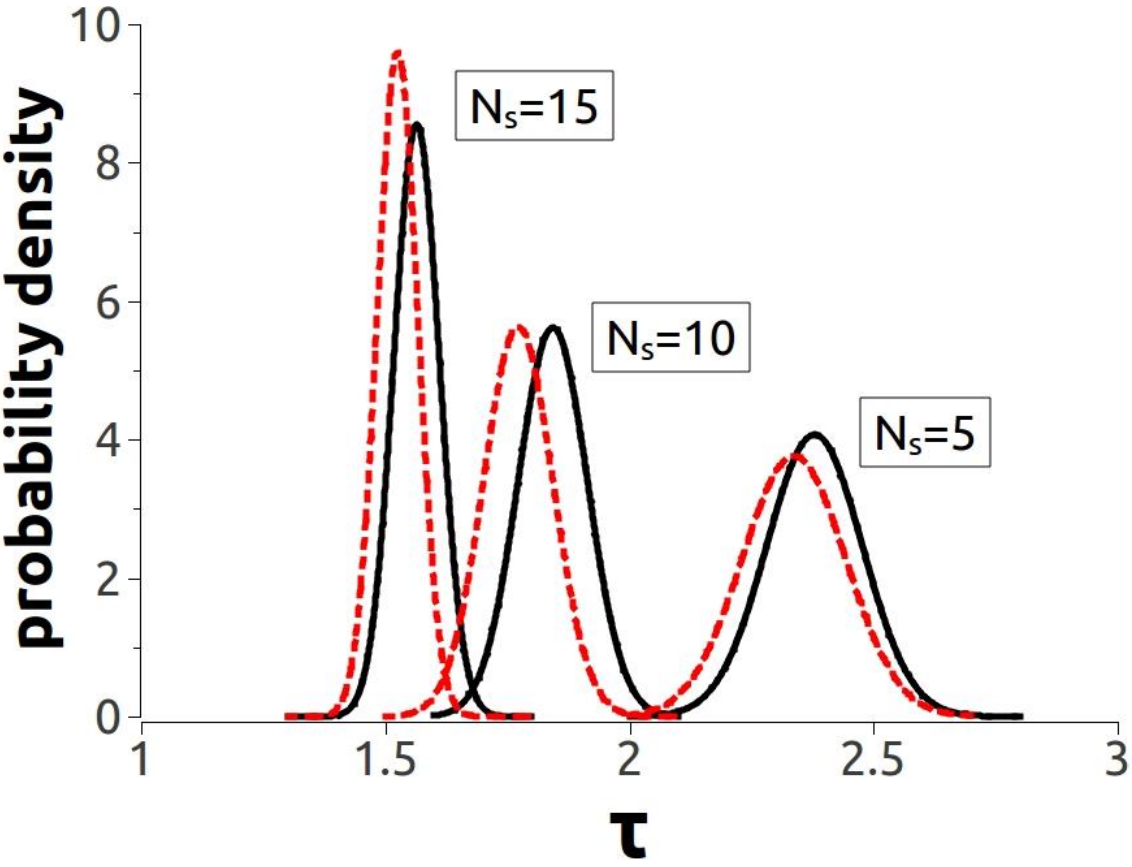

Figure 5.10: Residence time distributions of polymer chains of different lengths in a 600-step contraction channel as predicted by the central limit theorem for an acceleration g = 0.02. Black curves: $c = 2.4c^*$; Red curves: $c = 0.6c^*$.

Chapter 6

Conclusion and Outlook

In this thesis, we apply multiple mesoscopic methods to study the polymer migration in a periodic pressure-driven sudden contraction-expansion flow with contraction dimension comparable to the polymer radius of gyration. We demonstrate the potential application of this microfluidic device for the polymer separation. Not limited to polymer separation, more generally, we have demonstrated a method for predicting complex separation phenomena over large distances and time scales, using a combination of methods. First, we use Stochastic Rotation Dynamics (SRD) simulations to examine the effects of hydrodynamic interactions. We demonstrated in the contraction problem studied here that HI is not important, by comparing predictions of polymer concentration and residence time distribution from SRD with HI to what is obtained from Brownian dynamics (BD) simulations without HI. In such cases where HI is not important at the flow rates considered, we can therefore use the 15-fold faster BD simulations to obtain accurate residence time distributions (RTD's) over a few periodic contractions by averaging over hundreds or thousands of molecules simulated by BD (about 1000 chains in our simulations). Once the residence time autocorrelation distance is determined, we can convert such small-scale RTD's into RTD's for flow through arbitrary numbers of periodic contractions using the central limit theorem. In this way, we can determine the separation efficiency and separation mechanisms at work in complex geometries, by efficiently spanning from molecular-scale simulations up to macro-scale devices. As computational power

increases, the separation of more complex objects, including flexible, stiff, and branched polymers, colloids of various shapes, and biological cells, can be predicted using similar methods. Especially we think this method holds promising potential for designing microfluidic devices to separate different type cells in the developing field of cell sorting.

In this thesis it turns out that SRD can be replaced by the inexpensive BD simulations without HI in predicting the polymer migration, because in the special geometry we used here, HI plays an unimportant role. However SRD is a promising technique for studying the hydrodynamics of complex fluids. Though it is a novel method introduced by Malevanets and Kapral (1999) only decades ago, within this short period, enormous progress has been made, successful applications to problems dealing with various soft matter hydrodynamics have been carried out. In this thesis, SRD has been benchmarked for both fluid dynamics and polymer dynamics, and applied to more complex systems, in which thermal fluctuation and time-dependent hydrodynamic interaction are important. As commented by Gommper *et al*. (2006): "In such systems, the method (SRD) can play out its strengths, because the interactions of colloids, polymers, and membranes with the mesoscale solvent can all be treated on the same basis."

SRD can be used for simulating soft, deformable objects, such as capsules, vesicles, cells and *et al*., to understand and predict their behaviors in hydrodynamics flows, which is very important in science and technology. For example, capsules and vesicles can be used for drug carriers. Flow behavior of red blood cell (RBC) in the blood stream draws lots of research interest, e.g. under certain flow condition, RBCs may coagulate or be torn apart; to deliver the oxygen cargo, RBCs have to squeeze through narrow capillaries. To get a thorough understanding of these behaviors may help in the design of medical devices for various purposes.

To model soft and deformable objects of different shapes, a dynamically triangulated surface model [Ho and Baumgärtner (1990), Kroll and Gompper (1992), Gompper and Kroll (1997)] has been developed. Since SRD efficiently coarse grains the solvent with fluid particles and self-consistently captures HI, combining SRD and the solvent-free models and triangulated surfaces, the membrane hydrodynamics behavior can be efficiently and correctly described. Noguchi and Gompper(2004,2005,2006) have showed success of this approach to simulate vesicles in hydrodynamic flows. And we expect more applications of SRD for simulations in this direction.

References

Ho, J.S. and A. Baumgärtner, "Simulations of fluid self-avoiding membranes," *Europhys. Lett.* **12**, 295(1990).

Gompper, G. and D.M. Kroll, "Network models of fluid, hexatic and polymerized membranes," *J. Phys.: Condens. Matter* **9**, 8795(1997).

Gompper, G., T. Ihle, D. M. Kroll and R. G. Winkler, "Multi-Particle Collision Dynamics: A Particle-Based Mesoscale Simulation Approach to the Hydrodynamics of Complex Fluids," *Advances in Polymer Science* **221**, 1-87 (2008).

Kroll, D.M. and G. Gompper, "The conformation of fluid membranes: Monte Carlo simulations," *Science* **255**, 968(1992).

Malevanets, A. and R. Kapral, "Mesoscopic model for solvent dynamics," *Journal of Chemical Physics* **110**, 8805-8613 (1999).

Noguchi, H. and G. Gompper, "Fluid vesicle with viscous membranes in shear flow," *Phys. Rev. Lett.* **93**, 258102 (2004).

Noguchi, H. and G. Gompper, "Shape transitions of fluid vesicles and red blood cells in capillary flows," *Proc. Natl. Acad. Sci.* USA **102**, 14159 (2005).

Noguchi, H. and G. Gompper, "Dynamics of vesicle self-assembly and dissolution," *J. Chem. Phys.* **125**, 164908 (2006).